Development of a Liquefaction Assessment Method via a Contour Diagram Framework

ANASTASIOS STAMOU

September 22, 2024

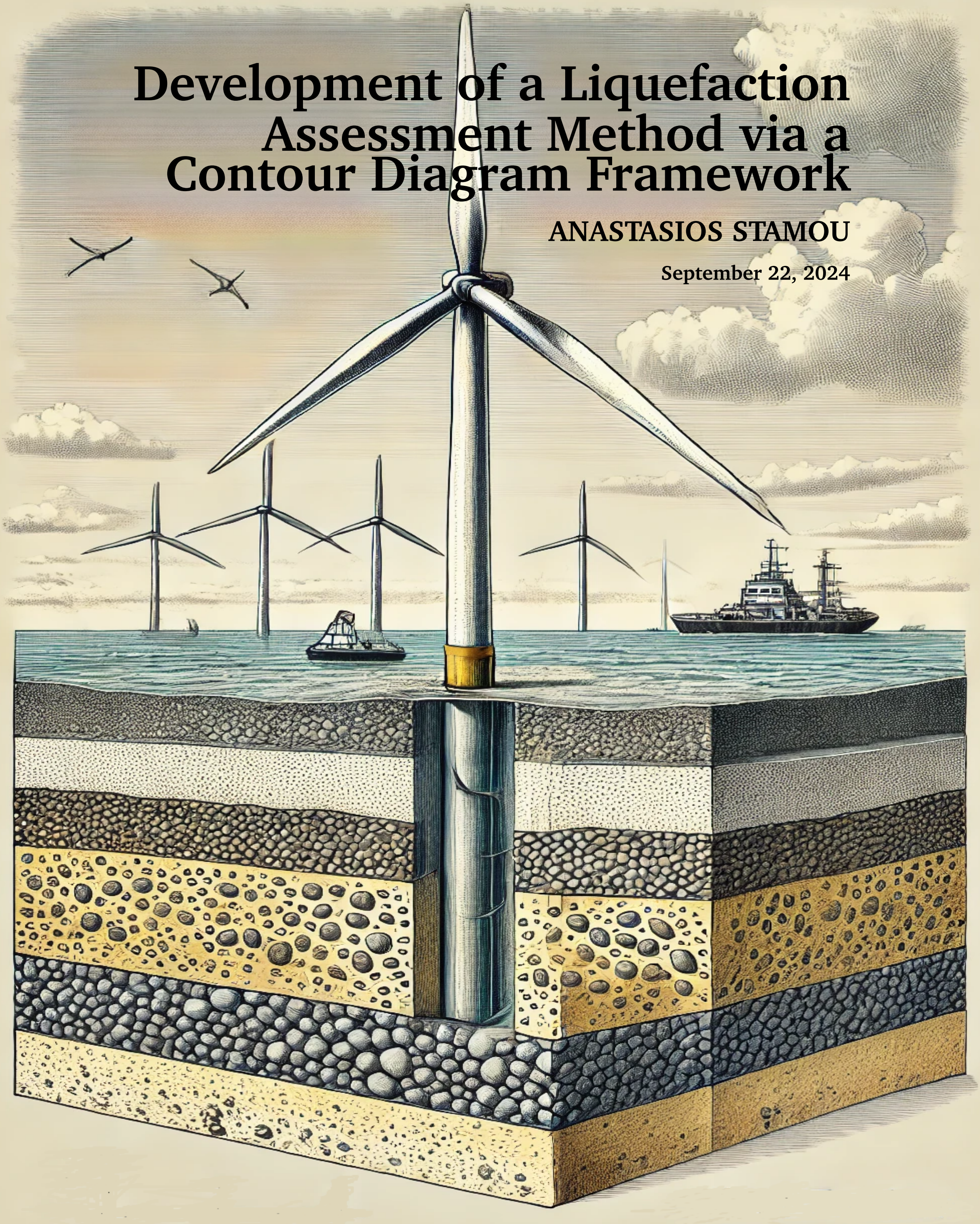

TU Delft Delft University of Technology

SIEMENS Gamesa RENEWABLE ENERGY

Development of a Liquefaction Assessment Method via a Contour Diagram Framework

Master of Science Thesis

Author:	Anastasios Stamou	(St. Number: 5708672)
Committee:	Dr. Ir. Evangelos Kementzetzidis	TU Delft - Chairman
	Dr. Ir. Karel N. van Dalen	TU Delft
	Ir. Stavros Panagoulias	SGRE - TU Delft
	Dr. Ir. Axel Nernheim	SGRE
	Ir. Pascal Voges - Espelage	SGRE

Cover: AI Generated Image

September 22, 2024

Abstract

The renewable energy sector is experiencing rapid growth, with offshore wind energy gaining significant global importance. Designing bottom-fixed Offshore Wind Turbines (OWTs) with Monopile (MP) foundations in seismic-prone regions, particularly in coarse-grained soils, presents challenges due to the risk of soil liquefaction during earthquake excitations.

The contour diagram framework (CDF) introduced by Andersen [2] is a procedure where normally non-symmetrical and irregular loading is transformed to regular load parcels. When combined with lab created contour diagrams, this approach is used to predict the accumulation of strains or pore pressure in the soil layer under examination.

This thesis examines the CDF for its capacity to predict excess pore water pressure (EPP) build-up in coarse-grained soils under seismic conditions.

The theoretical framework and current design practices for soil-structure interaction modeling emphasize the importance of addressing seismic pore pressure effects. Current practices focus on accounting for the net decrease in soil stiffness or shear strength resulting from the development of excess pore water pressure.

A key aspect of this study involved understanding the CDF and developing the necessary tools to apply it. These tools included the application of conventional liquefaction assessment methods, the extraction of cyclic stress ratio (CSR) time histories, cycle counting methods, preparation of loading parcels, and the final procedure for calculating the accumulated excess pore pressure (EPP). The robustness of these tools was validated on a Siemens Gamesa Renewable Energy (SGRE) project, confirming the proper application of the method.

The framework is validated by employing PM4Sand in PLAXIS 2D to produce the cyclic contour diagrams for a coarse-grained material. This material is then used to perform Site Response Analysis (SRA) on a soil column in PLAXIS 2D. Subsequently, a total stress SRA is conducted using both PLAXIS 2D and DEEPSOIL V7.0 to obtain the equivalent CSR and the number of cycles by employing a best-match soil material

similar to the one utilized in the undrained PLAXIS 2D analysis. By analyzing the CSR history obtained from the SRA, the equivalent number of cycles and CSRs are applied to the material's cyclic contour diagrams. Finally, the predictive capabilities of the method to forecast the EPP calculated in the PLAXIS model are assessed. The results demonstrate that the CDF reliably predicts the onset of liquefaction and low excess pore pressure ratios (EPPR), though it tends to be conservative when predicting EPPRs between 0.3 and 0.5.

Lastly, the CDF is applied on two case studies. The first involved a detailed analysis of a hydraulic project based on Akita Port, a coastal facility in Japan that experienced severe damage during the 1983 Nihonkai-Chubu earthquake. This earthquake-induced liquefaction caused significant deformation and settlement of the port structures, leading to extensive damage and highlighting the vulnerabilities of such infrastructure to seismic events. The site has since been well-documented and studied, making it an ideal case for applying and testing the CDF approach. The results demonstrate that the CDF effectively predicts the risk of soil liquefaction and accurately identifies that the intact port was not vulnerable to liquefaction.

The second case study involves a hypothetical application on an offshore wind park currently under development in the Netherlands, utilizing publicly available soil data from the North Sea region, where the park is planned. This region is characterized by complex soil conditions, including layers of dense sands. The analysis examines how incorporating soil degradation due to liquefaction into the design process impacts the foundation strategies and overall structural integrity of the wind turbines, providing insights into the necessity of considering seismic risks in the design of offshore renewable energy infrastructure.

Overall, this thesis presents that the CDF is a viable tool for evaluating liquefaction potential in coarse-grained soils under seismic loading in engineering practice. The derived EPPRs can subsequently be used to model the soil's behavior using degradation factors, providing a reliable basis for designing earthquake-resistant OWT foundations.

Acknowledgements

This master's thesis marks the culmination of two years of study at TU Delft.

At this moment, I would like to express my deepest gratitude to Professor Vangelis, Professor Karel, Stavros, Axel, and Pascal. Working with them has been an incredible experience and one of the most enriching learning opportunities of my life.

I am especially grateful to Professor Vangelis for introducing me to the opportunity and vouching for me for the internship that ultimately evolved into this master's thesis project at SGRE. His guidance and support throughout this project have been invaluable.

Words cannot express how deeply grateful I am to Axel, Pascal, and Stavros for welcoming me into SGRE and dedicating over 50 hours of their valuable time to meetings, guiding me, helping me progress, continuously encouraging my improvement over the past year, and patiently supporting me despite my shortcomings.

I am also grateful to Sachin, Dirk, Colinda, and the rest of my SGRE colleagues, as well as to fellow students, with whom I shared many productive hours in student meetings and at the company.

Lastly, I want to extend my heartfelt thanks to my parents for their unwavering belief in my abilities. Through their hard work and constant support, they have given me the invaluable opportunity to study abroad.

Anastasios Stamou
Delft, September 2024

Contents

List of Figures

List of Tables

Nomenclature

Latin symbols

C_n	Overburden Correction Factor	
DR	Relative Density	
DR, cs	Relative density on the critical state line	
De	Degradation Factor	
G	Shear Modulus	kPa
g	Acceleration of Gravity	$9.81m/s^2$
I_c	Soil Behavior Type Index	
N_{eq}	Equivalent Number of Cycles	
OCR	Over Consolidation Ratio	
p	Mean effective stress	kPa
PI	Plasticity Index	
p’	Mean Effective Stress	kN/m^2
q	Deviatoric Stress	kN/m^2
r	Deviatoric stress ratio tensor	
s	Deviatoric stress tensor	kPa
S_u	Shear Strength	kPa
V_s	Shear Wave Velocity	m/s
W	Energy stored in an elastic material	J

Greek symbols

α	Acceleration	m/s^2
Δ	Dissipated energy per unit volume	J/m^3

ϵ_v	Volumetric strain	
ξ	Damping ratio	
σ'	Effective stress	kPa
τ	Shear stress	kPa
ϕ_{cv}	Critical state friction angle	$^\circ$
ν	Poisson's ratio	

Subscripts

0	Initial
cyc	Cyclic
max	Maximum
min	Minimum
v	Vertical

Abbreviations

CDF	Contour Diagram Framework	
CDSS	Cyclic Direct Simple Shear	
CRR	Cyclic Resistance Ratio	
CSR	Cyclic Stress Ratio	
CPT	Cone Penetration Test	
De	Degradation Factor	
DSS	Direct Simple Shear	
EPP	Excess Pore Pressure	
EPPR	Excess Pore Pressure Ratio	
FE	Finite Element	
FEM	Finite Element Method	
MP	Monopile	
NCEER	National Center for Earthquake Engineering Research	
OWT	Offshore Wind Turbine	
PDE	Partial Differential Equation	
PPD	Pile Penetration Depth	m
PGA	Peak Ground Acceleration	g
PM4Sand	A plasticity model for sand	

RFC	Rainflow Counting
RPF	Range Pair Counting
SF	Safety Factor
SGRE	Siemens Gamesa Renewable Energy
SRA	Site Response Analysis
SPT	Standard Penetration Test

Chapter 1

Introduction

1.1 Motivation

Due to the rapid increase in Earth's temperature caused by the over consumption of fossil fuels, the world has seen a significant shift towards renewable energy. One rapidly growing practice is the placement of wind turbines offshore. Offshore wind farms benefit from a well-defined shear profile, where the variation in wind speed from the bottom to the top of the turbine's rotor is both predictable and consistent. As a result, there is higher potential for higher energy production. Additionally, larger turbines can be deployed offshore since they can be transported by vessels rather than by roads.

To maximize power output and efficiency, OWTs have been increasing in size, necessitating optimized foundation designs to ensure they can withstand severe events over their 25-30 year life cycle, including earthquakes. This thesis focuses on OWTs founded on MPs in coarse-grained soils. The MP foundation consists of a single, large-diameter steel pipe driven into the seabed to provide stability and support for the wind turbine.

1.2 Research Background

When considering liquefaction in engineering practice, the most widely used methods are based on the work of Youd et al. [40] and Idriss & Boulanger [8]. These methods determine the likelihood of liquefaction using a Safety Factor (SF), derived by normalizing Cone Penetration Test (CPT) or Standard Penetration Test (SPT) results with various factors to align with laboratory conditions. These approaches, calibrated for silica soils, are intended for depths up to 20 meters and do not incorporate soil-structure interaction modeling using the SF.

In onshore engineering projects, it is standard practice to mitigate the risk of liquefaction by improving soil conditions, such as adding drainage or densifying upper layers with vibrocompactors, when the SF is below 1. However, such measures are not feasible for offshore projects.

Regarding soil-structure interaction modeling, the Japanese Road Association [27] proposed using soil ultimate strength degradation factors based on the SF, the cyclic resistance of the soil, and depth. The degraded soil profile can be used to model the soil structure interaction to account for the increased strains.

Recently, the growing demand for MPs for offshore projects has increased interest in assessing and modeling liquefaction at depths greater than 20 meters, as large-diameter MPs can extend beyond 40 meters below mudline. To address this, foundation designers use the SRA result accelerations, rather than just Peak Ground Acceleration (PGA) multiplied by a depth stress reduction factor, to enhance method accuracy.

Andersen [2] proposed using contour diagrams to calculate accumulated strains or EPP, especially for offshore engineering. This method involves breaking the initial loading sequence into smaller load parcels and applying these to laboratory-generated contour diagrams until an equivalent number of cycles is reached. This is the foundation of the examined CDF of this thesis.

For modeling soil-structure interaction when EPP is known, Boulanger [9], building on experiments by Dobry et al. [18], recommends using a degradation factor dependent on the EPPR R_u. This approach aligns with current design practices for MP foundations of OWTs, which are designed using p-y curves consistent with Winkler's foundation theory [39],[16],[3].

Other researchers have developed new families of p-y curves to account for the residual strength of denser soils, making the design less conservative [29].

The development of constitutive models for Finite Element (FE) software like PLAXIS 2D or OpenSEEs enables accurate calculation of EPPRs. However, these models are computationally expensive, requiring significant run times and expertise.

This underscores the need for a robust and user-friendly method for calculating EPP accumulation.

1.3 Thesis Objective

The objective of this thesis is to examine and validate a CDF for predicting EPP in coarse-grained soils during earthquake excitation. The primary research question this thesis seeks to answer is whether the CDF can reliably be used to predict EPPRs.

To answer that question the thesis is build around the following sub objectives.

Initially, to present the CDF and detail the development of practical tools programmed in MATLAB. These tools are validated by comparing their results to a SGRE project, ensuring their accuracy and robustness.

Following tool development, the method is further validated using PLAXIS 2D and the PM4Sand constitutive model. This phase of validation ensures that the framework performs reliably under different modeling conditions.

In the final phase, the method is applied to real-world case studies to evaluate its performance in practical scenarios. Then the impact of EPP on the design of OWTs is examined, particularly in relation to Pile Penetration Depth (PPD).

Through these case studies, the thesis examines how the use of this method can enhance the design process for OWT foundations and other applications in seismic-prone regions.

1.4 Thesis Outline

To achieve the Thesis Objective set in the previous section, the thesis is structured in the following manner:

Chapter 2 introduces the basic theoretical foundations on which the rest of the thesis is built on.

Chapter 3 discusses SRA, best practices and liquefaction assessment techniques.

Chapter 4 contains the validation of the developed MATLAB tools based on an SGRE offshore wind project to ensure their robustness.

Chapter 5 contains the validation of the CDF based on data from FE analysis conducted on PLAXIS 2D for sands with different relative densities.

Chapter 6 showcases the robustness of the CDF by comparing the results to a well documented case study and then exhibits how liquefaction would alter the design of an OWT in terms of PPD.

Chapter 7 aims to provide an overview of the thesis and offer recommendations for areas of future research and guidelines which could be adopted from the industry.

Chapter 2

Theoretical Framework

This chapter establishes the theoretical foundation needed to understand the behavior of soils under seismic loading and the application of the CDF for liquefaction assessment.

The chapter begins by discussing the propagation of seismic waves and their impact on soil layers, which is essential for understanding how ground motion influences soil responses during earthquakes.

Next, the chapter explores the phenomenon of liquefaction, detailing the mechanisms that trigger it and its consequences for soil stability. This is followed by an examination of the behavior of coarse-grained soils under undrained cyclic loading, a key factor in evaluating soil performance during seismic events.

The chapter also introduces PLAXIS 2D and its PM4Sand model, which are used to simulate soil behavior under dynamic loading. Additionally, the concepts of shear modulus degradation and damping are explained to show how soil stiffness and energy dissipation evolve with increasing strain.

Finally, the chapter covers cycle counting techniques and the CDF, which provide the basis for the liquefaction assessment method under examination.

2.1 Earthquakes and Liquefaction

Earthquakes are caused by the sudden release of energy along geological faults or from the friction between tectonic plates. In some cases, they can also be triggered by volcanic activity or human-induced events, albeit at lower magnitudes. This release of energy generates ground shaking, which alters shear stresses in the soil at various depths. These changes can result in significant surface deformations and pose a threat to civil structures. Figure 2.1 provides a historical overview of earthquake events, highlighting that the most significant occurrences typically align with the tectonically active regions along the Pacific Ocean.

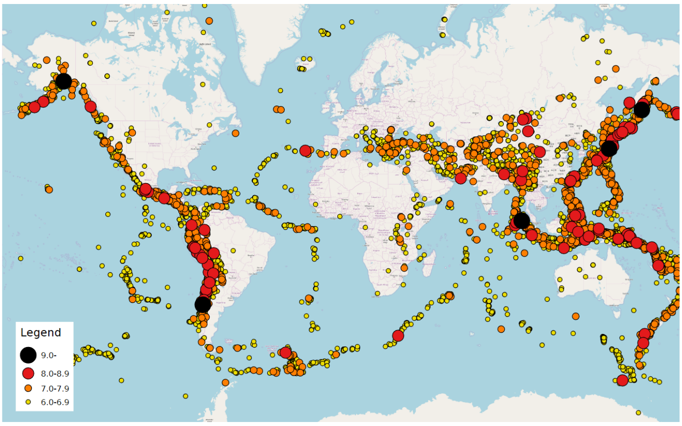

Figure 2.1: Map of Earthquakes Between 1900-2017, Source: Search Earthquake Archives, USGS

During an earthquake, cyclic horizontal ground movements generate shear waves that propagate through the soil, inducing cyclic shear stresses. In coarse-grained soils, especially in conditions of poor drainage, this cyclic loading can lead to the buildup of EPP. As a result, the effective shear strength of the soil diminishes, weakening the soil structure. This process can result in liquefaction, as illustrated in Figure 2.2. Liquefaction is discussed in more detail in Section 2.1.2.

2.1.1 Seismic Waves Propagation

In basic geotechnical seismic analyses, cyclic ground motion is quantified by the maximum horizontal acceleration at the ground surface (α_{max}), also known as peak ground acceleration (PGA). Since predicting earthquakes is not feasible, PGA values are determined based on historical earthquake data and fault studies [8]. Seismic waves include compressional (P-waves) and shear (S-waves) waves. Compressional waves move in the direction of propagation, while shear waves oscillate perpendicularly. The speed of these waves is defined by the following equations:

Figure 2.2: Soil Liquefaction - Christchurch Earthquake 2011, Source: Timothy Musson

$$V_p = \sqrt{\frac{E_{\text{oed}}}{\rho}} \tag{2.1}$$

$$V_s = \sqrt{\frac{G}{\rho}} \tag{2.2}$$

Due to soil heterogeneity, these waves undergo changes primarily because of material and radiation damping of soils. Radiation damping results in a decrease in specific energy due to geometric spreading. Consequently, the amplitude of stress waves diminishes with distance, even though the total energy remains constant. Additionally, material damping affects propagated stress waves as part of the elastic energy is lost as heat.

2.1.2 Liquefaction

According to Eurocode 8 [20], soil liquefaction is defined as ”a decrease in shear strength and/or stiffness caused by an increase in pore water pressures in saturated cohesionless material during earthquake ground motion, leading to significant permanent deformations or nearly zero effective stress.” Liquefaction can be classified into two types:

1. **Flow (static) liquefaction:** This occurs when static shear stress exceeds the shear strength of the liquefied soil, leading to dramatic flow failures. Large deformations are driven by static shear stresses once triggered. Cyclic stresses can destabilize the soil, reducing its strength enough for static stresses to cause flow failure. These failures are characterized by their sudden onset, rapid development, and the extensive distances over which liquefied materials move [28].

2. **Cyclic liquefaction:** Cyclic liquefaction occurs when repeated cyclic loading during an earthquake causes a progressive build-up of pore water pressure in saturated, cohesionless soils. Even though the static shear stress is less than the shear strength of the soil, the cyclic stress leads to a gradual reduction in effective stress, weakening the soil structure over time. This process can result in significant deformation. During the shaking, the soil behaves like a viscous fluid, leading to ground oscillation and, in some cases, lateral displacement. Unlike flow liquefaction, cyclic liquefaction generally results in more controlled and less catastrophic movement, but it can still lead to considerable damage, including settlement, foundation failure, and ground distortion [28].

Soil liquefaction can result in the following effects:

- Ground surface settlement
- Bearing capacity failure of foundations
- Lateral movement of slopes
- Permanent soil displacements
- Changes in original site conditions (post-liquefaction), including loss of strength and stiffness

2.2 Behavior of Coarse-Grained Soils Under Undrained Cyclic Loading

The response of sands to undrained cyclic loading is closely related to their behavior during earthquake shaking, with loose granular soils being particularly susceptible to liquefaction. In loose to medium sands, liquefaction triggering involves continuous contractive deformation, which is limited by a transformation phase just before reaching a critical state. At this phase, the soil's tendancy to contract shifts from contractive to dilative, resulting in a progressive development of shear strains due to loss of stiffness. Multiple loading cycles cause soil densification as the grain structure collapses during undrained shearing.

Laboratory tests have shown that pore water pressure increases significantly during the initial cycles due to large initial contraction, and again at later stages due to high pore pressure and increased shear strain amplitude, leading to a reduction in apparent shear stiffness [15].

These characteristics have been observed through cyclic laboratory tests, such as the cyclic triaxial test and Cyclic Direct Simple Shear (CDSS) test. In this thesis, the test that will be discussed is the CDSS. The behavior of coarse-grained soils under cyclic loading can be illustrated through typical laboratory results, as shown in Figure 2.3a and Figure 2.3b, where the relationships between deviatoric stress and effective stress, as well as EPP and shear strain, are demonstrated. Additionally, a typical CDSS apparatus is depicted in Figure 2.4.

2.2.1 Cyclic Direct Simple Shear Tests

Soil liquefaction resistance at the element level can be assessed using laboratory-based methods, where a representative CSR is applied to a specimen to determine

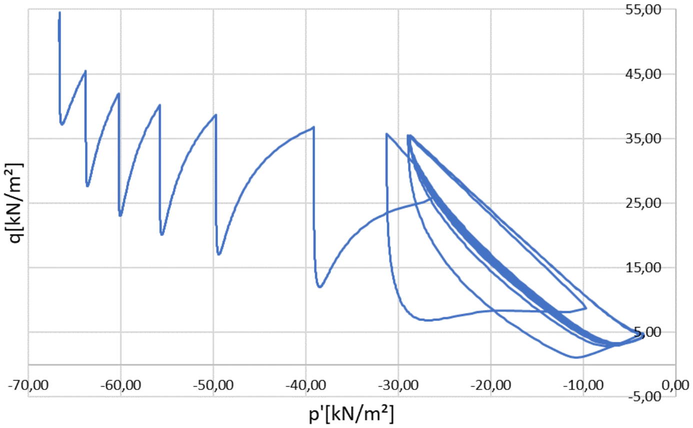

(a) Deviatoric Stress q vs Effective Stress p'

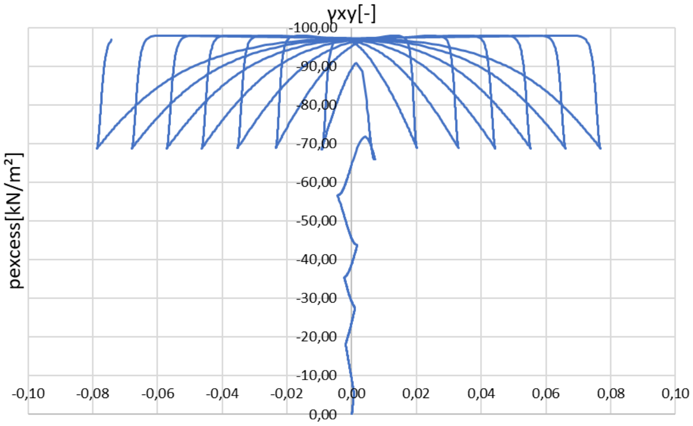

(b) Excess Pore Pressure p vs Shear Strain γ

Figure 2.3: Typical Cyclic Direct Simple Shear Laboratory Results for Coarse-Grained Soils

Figure 2.4: Cyclic Direct Simple Shear Test System - Source: Geocomp

the number of cycles required for liquefaction (denoted as N_{eq}). Cyclic loading is typically applied as a shear force or shear displacement on a horizontal plane at either the top or bottom of the specimen, assuming complementary shear stress develops on vertical planes along the sides.

Despite the ability to perform non-uniform cyclic loading tests, there is no standardized procedure for interpreting these results. Uniform cyclic loading tests are more commonly used to obtain cyclic strength curves.

Among the prevalent laboratory tests for analyzing the cyclic response of soil samples are CDSS tests. CDSS tests are well-suited for simulating both the initial in-situ lateral stresses K_0 and the strain conditions in level ground, as well as the stresses caused by vertically propagating shear waves during an earthquake. CDSS tests use cylindrical specimens with a height-to-diameter ratio typically equal to 0.5.

The cyclic resistance of soil to liquefaction is generally defined by the cyclic resistance ratio (CRR), at which a soil sample will reach liquefaction, typically after 15 uniform cycles. CRR is the ratio of the applied cyclic shear stress that leads to liquefaction to the initial effective vertical stress, as follows:

$$\text{CRR} = \frac{\tau_{\text{cyc}}}{\sigma'_{vc}} \tag{2.3}$$

2.3 Shear Modulus Degradation and Damping Curves

When subjected to cyclic loading, such as during seismic events, soils experience a reduction in stiffness and an increase in damping. These changes are particularly evident in seismic analysis, where shear modulus degradation and damping curves are commonly used to characterize soil behavior.

The shear modulus degradation curve illustrates the decrease in soil stiffness, as indicated by the shear modulus, with increasing shear strain, reflecting strain-dependent stiffness. An increase in cyclic shear strain results in a decrease in the shear modulus as exhibited in Figure 2.5a.

Cyclic loading, which involves unloading and reloading, creates a hysteretic loop in the stress-strain curve, indicating energy dissipation in each load cycle, leading to damping. The damping level is proportional to the shear strain amplitude in the load cycle; higher cyclic shear strain results in greater damping as indicated in Figure 2.5b.

The damping ratio (ξ) is defined by the following expression:

$$\xi = \frac{1}{4\pi}\frac{\Delta}{W} \tag{2.4}$$

where Δ is the dissipated energy per unit volume in one hysteresis loop, and W is the energy stored in an elastic material with the same shear modulus as the visco-elastic material.

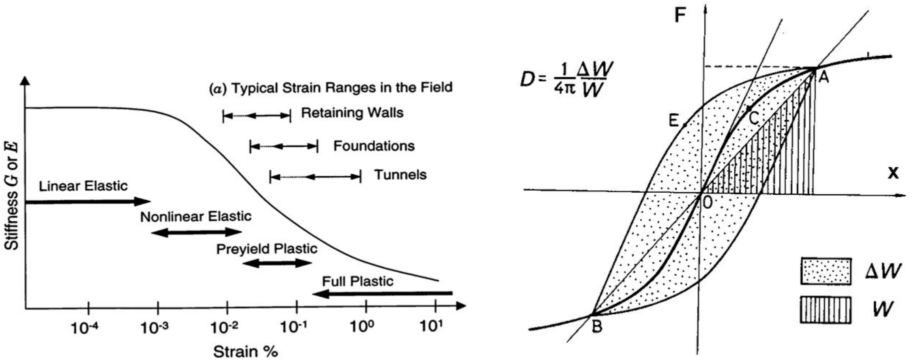

(a) Stiffness Degradation Curve in Terms of Shear Modulus G and Young's Modulus E. [30]

(b) Hysteretic Damping Definition [10]

Figure 2.5: Stiffness Degradation and Hysteretic Damping Curves.

2.4 The Contour Diagram Framework

The CDF introduced by K.H. Andersen [2] provides a systematic approach for assessing soil behavior under cyclic loading, specifically in offshore foundation design. This framework is crucial for predicting the accumulation of strains or EPP in soils subjected to dynamic loading, such as from waves, wind, or earthquakes in offshore environments.

The framework operates by converting complex, irregular cyclic loading conditions into load parcels using a cycle counting method. These load parcels are then transformed, through the use of laboratory-generated contour graphs, into an equivalent number of uniform cycles that correspond to specific levels of accumulated strain or EPP. Cyclic contour diagrams are graphical tools that map the soil's response to cyclic loading.

According to Andersen [2], these contour diagrams provide a visual representation of how soils behave under cyclic loading, making it easier to assess and predict the potential for soil degradation, including liquefaction and cyclic strain accumulation. The diagrams are constructed by normalizing shear stresses to the initial effective overburden stress of the soil, and then plotting the contour lines of the resulting cyclic response, such as strain or pore pressure, against the number of cycles and CSR. This approach allows for the direct application of site-specific soil parameters and loading conditions, ensuring that the predictions are tailored to the actual conditions encountered in offshore environments.

By using the CDF, engineers can more accurately predict the long-term effects of cyclic loading on soils, which is essential for the design of stable and resilient foundations. This method is particularly valuable in regions prone to seismic activity, where the risk of soil liquefaction and cyclic degradation can pose significant challenges to foundation stability. The ability to incorporate site-specific data into the contour diagrams enhances the accuracy of these predictions, providing a robust tool for designing safe and effective structures.

2.5 Cycle Counting Methods

Cycle counting methods are fundamental tools in geotechnical engineering, essential for analyzing cyclic loading and its effects on soil behavior. These techniques quantify the number and amplitude of the stress cycles that soil elements undergo during dynamic loading events such as earthquakes. In this study, two cycle counting methods are considered: Rainflow Counting (RFC) and Range Pair Counting (RPC).

2.5.1 Rainflow Counting

RFC is a widely accepted method for identifying and quantifying stress cycles from any arbitrary complex loading history. This method is especially beneficial when dealing with regular load sequences as it was developed for fatigue analysis, making it suitable for earthquake-induced stress analyses. The RFC algorithm simplifies the stress history into individual cycles through a conceptual ”rainflow” process, akin to how rainwater flows down a pagoda roof.

The process involves:

- Identification of peaks and valleys in the stress-time history.
- The peaks are connected to a subsequent valley, which forms potential cycles.
- The application of rules for eliminating smaller cycles that fall within larger cycles, focusing on the significant stress reversals.

RFC offers a clear and systematic way to decompose complex loading signals into a series of half-cycles, each characterized by its amplitude and mean stress. Although this method was initially developed for fatigue analysis, it has been adapted for geotechnical applications aimed at assessing the cyclic resistance of soils. RFC applied to a sample signal is illustrated in Figure 2.6.

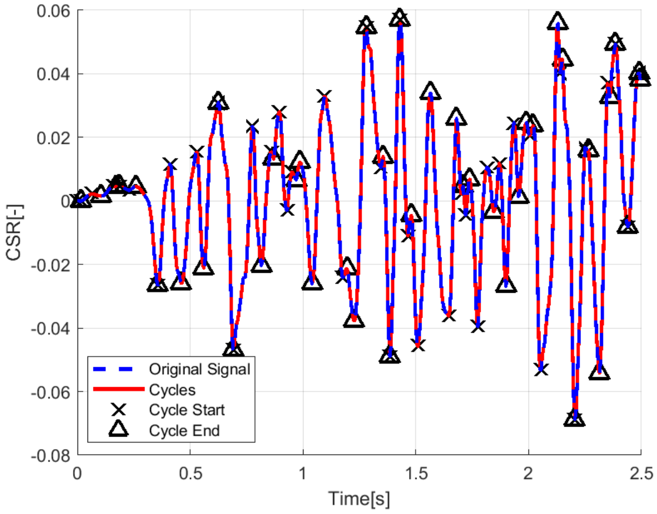

Figure 2.6: Sample Rainflow Counting Cycle Identification

2.5.2 Range Pair Counting

RPC is another cycle counting method essentially different in approach from RFC when analyzing cyclic loading. In this technique the process includes:

- Sorting of the whole stress-time history into pairs of stress ranges between two consecutive zero-crossings.
- Counting the repetitions of each stress range without considering the sequence of loadings.

RPC uses less complex logic and resources compared to RFC. This method does not consider the sequence of stress ranges but only their distribution. Therefore, it has application in cases where the sequence of the cycles applied is not that critical.

Figure 2.7 illustrates the process of RPC, where each cycle commences at the point where the previous cycle ends. This figure highlights the identification of stress ranges within the loading sequence, demonstrating how the method captures cyclic patterns without incorporating the order of load application. Such an approach is beneficial in situations where computational demand needs to be minimized, while still providing an effective preliminary assessment of cyclic behavior.

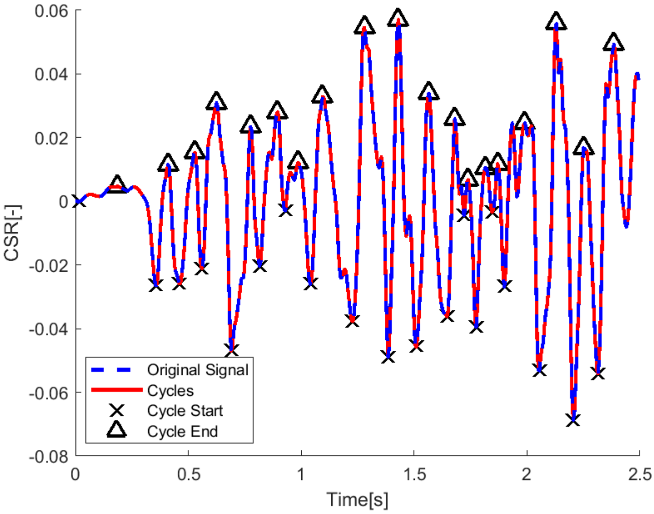

Figure 2.7: Sample Range Pair Counting Cycle Identification

2.6 Finite Element Method and Its Application in PLAXIS

The FEM is a powerful numerical technique widely used in engineering to numerically solve complex Partial Differential Equations (PDEs). It involves discretizing a continuous domain, such as a soil column or foundation, into a mesh of smaller, FEs. Each element is interconnected at nodes, where the equations of motion are solved to determine the behavior of the system under complex loads and boundary conditions.

PLAXIS is a specialized FEM software designed for geotechnical applications. It provides robust tools for modeling and analyzing soil behavior, including the effects of consolidation, seepage, and dynamic loading. The software allows for detailed modeling of soil layers, foundation elements, and groundwater flow, making it a preferred choice for engineers working on projects such as embankments, excavations, and offshore foundations.

One of the key strengths of PLAXIS lies in its advanced soil constitutive models, such as the Hardening Soil Small and the PM4Sand model. These models enable realistic simulation of soil behavior under different loading conditions, accounting for factors like plasticity, anisotropy, and strain-dependent stiffness. Additionally, PLAXIS can handle complex boundary conditions and loading scenarios, such as earthquake loading, by incorporating dynamic analysis capabilities through its PLAXIS 2D and 3D modules.

In dynamic analyses, such as those involving seismic loading, PLAXIS allows the integration of time-dependent loads and the simulation of wave propagation through soil. This is essential for accurately capturing the response of soil structures to seismic events.

2.7 PM4Sand Constitutive Model

The PM4Sand model is a constitutive model designed specifically for simulating the behavior of sands under dynamic loading conditions. It captures essential phenomena such as the generation of EPP, liquefaction, and post-liquefaction responses. The model is widely used in earthquake engineering due to its simplicity and efficiency, requiring a relatively small number of parameters that can typically be derived from in-situ test data, including the Standard Penetration Test (SPT), Cone Penetration Test (CPT), and shear wave velocity (V_s) measurements [5]. The model is based on the bounding surface plasticity framework for sand, initially proposed by Dafalias [13], with subsequent modifications made to improve its ability to simulate the stress-strain response under seismic loading [6, 7].

2.7.1 Model Formulation

The PM4Sand model is formulated in terms of effective stresses, making it suitable for 2D plane-strain analyses, where out-of-plane stresses are assumed to have minimal influence. The model captures both the elastic and plastic behavior of sand under cyclic loading conditions, focusing on key stress and strain variables. These quantities include the effective stress tensor σ, mean effective stress p, deviatoric stress tensor s, and the deviatoric stress ratio tensor r, which are expressed as follows:

$$\sigma = \begin{pmatrix} \sigma_{xx} & \sigma_{xy} \\ \sigma_{xy} & \sigma_{yy} \end{pmatrix} \tag{2.5}$$

$$p = \frac{\sigma_{xx} + \sigma_{yy}}{2} \tag{2.6}$$

$$s = \sigma - pI = \begin{pmatrix} \sigma_{xx} - p & \sigma_{xy} \\ \sigma_{xy} & \sigma_{yy} - p \end{pmatrix} \tag{2.7}$$

$$r = \frac{s}{p} = \begin{pmatrix} \frac{\sigma_{xx}-p}{p} & \frac{\sigma_{xy}}{p} \\ \frac{\sigma_{xy}}{p} & \frac{\sigma_{yy}-p}{p} \end{pmatrix} \tag{2.8}$$

Strains are similarly partitioned into volumetric and deviatoric components. The volumetric strain ϵ_v and the deviatoric strain tensor e are expressed as:

$$\epsilon_v = \epsilon_{xx} + \epsilon_{yy} \tag{2.9}$$

$$e = \epsilon - \frac{\epsilon_v}{3} I = \begin{pmatrix} \epsilon_{xx} - \frac{\epsilon_v}{3} & \epsilon_{xy} \\ \epsilon_{xy} & \epsilon_{yy} - \frac{\epsilon_v}{3} \end{pmatrix} \tag{2.10}$$

The out-of-plane normal stress σ_{zz} is calculated based on a linear elastic assumption, using the equation:

$$d\sigma_{zz} = \nu(d\sigma_{xx} + d\sigma_{yy}) \tag{2.11}$$

where ν is Poisson's ratio.

2.7.2 Critical State Soil Mechanics Framework

The PM4Sand model is grounded in the Critical State Soil Mechanics (CSSM) framework [34], which provides a theoretical basis for modeling soil behavior under large deformations and cyclic loading. A key parameter in this framework is the relative state parameter index ξ_R, which quantifies how far the current state of the soil is from its critical state. This index is a refinement of the state parameter ψ introduced by [4], and is expressed as:

$$\xi_R = D_{R,cs} - D_R \tag{2.12}$$

where D_R is the current relative density of the soil, and $D_{R,cs}$ is the relative density corresponding to the critical state at the current mean effective stress p.

The critical state relative density $D_{R,cs}$ is determined by the critical state line in the $D_R - p$ plane, given by:

$$D_{R,cs} = R\left(Q - \ln\left(\frac{100p}{p_A}\right)\right) \tag{2.13}$$

where p_A represents atmospheric pressure, and Q and R are empirical parameters related to the sand's behavior, typically calibrated using values from Bolton's (1986) empirical data, with $Q \approx 10$ and $R \approx 1.5$ for quartzitic sands.

2.7.3 Bounding, Dilatancy, Critical, and Yield Surfaces

The PM4Sand model uses bounding, dilatancy, and critical surfaces to capture soil behavior under cyclic loading. These surfaces are defined using the relative state parameter index (ξ_R), which measures the distance between the current state of the soil and its critical state.

- The bounding surface governs the hardening or softening of the soil under load.
- The dilatancy surface controls the transition between soil contraction and dilation.
- The critical state surface represents the point where the soil reaches constant volume shear under continuous deformation [21].

The bounding and dilatancy surfaces are expressed as functions of the critical stress ratio (M) and the relative state index:

$$M_b = M \cdot \exp(-n_b \xi_R) \quad \text{(Bounding stress ratio)} \tag{2.14}$$

$$M_d = M \cdot \exp(n_d \xi_R) \quad \text{(Dilatancy stress ratio)} \tag{2.15}$$

$$M = 2\sin(\phi_c^\nu) \quad \text{(Critical stress ratio)} \tag{2.16}$$

Where n_b and n_d are parameters controlling the spacing of the surfaces relative to the critical state, and ϕ_c^ν is the critical state friction angle. These surfaces allow simulation of the behavior of sands under varying cyclic loads, capturing both densification and liquefaction phenomena [21].

2.7.4 Elastic Part of the Model

The elastic behavior of the PM4Sand model is governed by the bulk modulus (K) and shear modulus (G). These moduli vary with the mean effective stress and depend on the fabric and stress conditions of the soil.

The volumetric elastic strain ($d\epsilon_v^{el}$) and the deviatoric elastic strain (de^{el}) are given by:

$$d\epsilon_v^{el} = \frac{dp}{K} \tag{2.17}$$

$$de^{el} = \frac{ds}{2G} \tag{2.18}$$

The shear modulus G evolves with the mean effective stress p, stress ratio, and fabric tensor as:

$$G = G_0 p_A \sqrt{\frac{p}{p_A}} \left(1 - C_{SR,0} \left(\frac{M}{M_b}\right)^{m_{SR}}\right) \left(\frac{1 + \frac{z_{\text{cum}}}{z_{\text{max}}}}{1 + \frac{z_{\text{cum}}}{z_{\text{max}}} C_{GD}}\right) \tag{2.19}$$

Where:

- G_0 is the initial small-strain shear modulus.
- p is the mean effective stress.
- p_A is atmospheric pressure.
- $C_{SR,0}$ controls the impact of the stress ratio.
- M/M_b is the ratio of the current stress state to the bounding surface.
- m_{SR} controls the influence of the stress ratio on G.
- z_{cum} is the cumulative fabric change, and z_{max} limits the fabric accumulation.
- C_{GD} controls the dilatancy contribution to the modulus [21].

This formulation captures the small-strain elastic behavior of soils before plastic deformation begins.

2.7.5 Plastic Components of the Model

The plastic behavior of the PM4Sand model involves both volumetric and deviatoric plastic strains, which are activated when loading exceeds the elastic threshold. The plastic volumetric strain ($d\epsilon_v^{pl}$) and deviatoric plastic strain (de^{pl}) are calculated using a loading index (L) and the dilatancy (D):

$$d\epsilon_v^{pl} = \langle L \rangle D \tag{2.20}$$

$$de^{pl} = \langle L \rangle \mathbf{n} \tag{2.21}$$

Where $\mathbf{n}$ represents the normal to the yield surface, and L governs the magnitude of plastic deformation [21].

Plastic Shear Modulus

The plastic shear modulus (K_p) is a critical parameter that controls how soil stiffness degrades under cyclic loading. The formulation for K_p depends on the relative state index and back-stress ratio tensor (α), and is expressed as:

$$K_p = G h_0 \frac{\sqrt{(\alpha^b - \alpha) : \mathbf{n}}}{\left[\exp\left((\alpha - \alpha_{\text{in}}^{\text{app}}) : \mathbf{n}\right) - 1\right] + C_{\gamma_1}} C_{\text{rev}} \tag{2.22}$$

Where:

- G is the shear modulus.
- h_0 adjusts the ratio between plastic and elastic moduli.
- α^b is the bounding stress ratio tensor.
- α is the back-stress ratio tensor.
- $\mathbf{n}$ is the unit normal to the yield surface.
- C_{rev} is the reverse loading correction factor.
- C_{γ_1} ensures numerical stability [21].

This plastic shear modulus controls how quickly the soil loses stiffness during cyclic loading, making it crucial for accurately predicting liquefaction and soil degradation.

2.7.6 Plastic Volumetric Strains - Dilatancy and Contraction

The PM4Sand model accounts for both dilatant and contractant behaviors. Dilatancy refers to the expansion of soil volume under shear, while contraction describes the reduction in volume.

Dilatancy

The model calculates dilatancy using:

$$D = Ad_0[(\alpha_d - \alpha) : \mathbf{n}] \tag{2.23}$$

Where Ad_0 is a parameter controlling the rate of soil dilation [21].

Contraction

For soils prone to contraction, the model uses the following equation:

$$D = Ad_c \frac{[(\alpha - \alpha_{\text{in}}) : \mathbf{n} + C_{\text{in}}]^2}{(\alpha_d - \alpha) : \mathbf{n} + C_D} \tag{2.24}$$

This dual formulation of dilatancy and contraction handles both loose and dense sands, simulating the full spectrum of behaviors observed during cyclic and seismic loading [21].

2.7.7 Calibration Parameters and Their Role

The PM4Sand model is calibrated using a small number of parameters, which are divided into primary and secondary categories. These parameters control various aspects of the material's stress-strain behavior, including its liquefaction resistance and post-liquefaction performance.

Primary Parameters:

- D_{R0} — The initial relative density, which influences the soil's dilatancy and cyclic resistance. It is commonly estimated from field tests such as SPT or CPT.
- G_0 — A coefficient controlling the small-strain shear modulus (G), which is typically derived from the soil's shear wave velocity (V_s).
- h_{p0} — The contraction rate parameter, which governs the soil's tendency to contract under cyclic loading and is critical for matching observed cyclic resistance ratios (CRR).

- p_A — Atmospheric pressure, used for normalizing stress values.

Secondary Parameters:

- e_{max}, e_{min} — Maximum and minimum void ratios, influencing the calculation of relative density and state parameters.
- n_b, n_d — Parameters that define the relative positions of the bounding and dilatancy surfaces with respect to the critical state surface, affecting the model's prediction of peak friction angles and phase transformation behavior.
- ϕ_{cv} — Critical state friction angle, which defines the long-term shearing resistance of the sand at constant volume.
- ν — Poisson's ratio, determining the elastic volumetric response of the material.
- Q, R — Critical state line parameters used to describe the behavior of sand in the $D_R - p$ space.
- $PostShake$ — A parameter used to simulate post-liquefaction reconsolidation, where elastic moduli are reduced to capture the sedimentation effects following liquefaction.

2.7.8 State Parameters

The model tracks several state parameters that evolve during the simulation, allowing for the dynamic behavior of sands under cyclic loading to be accurately captured. These include:

- σ_{v0} — The initial vertical stress, initialized at the beginning of each phase.
- r_u — The EPPR, which is defined as $r_u = 1 - \frac{\sigma_v}{\sigma_{v0}}$, and is used to monitor the development of pore pressure during cyclic loading.
- $r_{u,max}$ — The maximum EPPR reached during the current phase, providing insight into the soil's liquefaction potential.

Figure 2.8 illustrates the typical behavior of the PM4Sand model under both drained and undrained conditions.

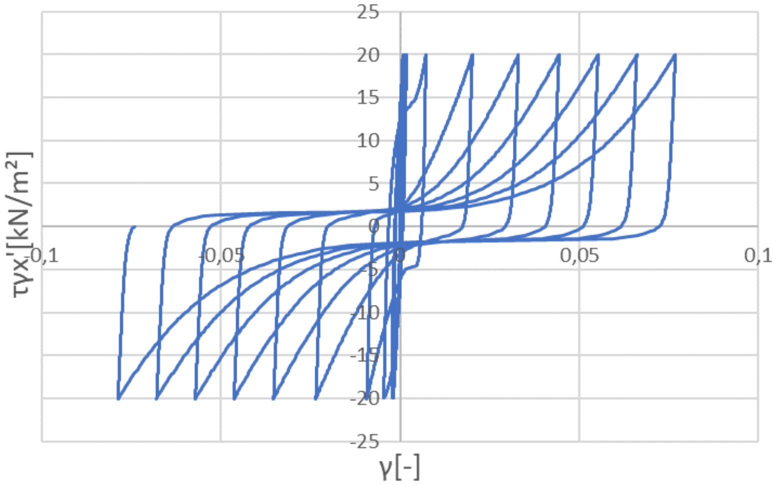

(a) Undrained Sand Behavior under Cyclic Loading - PM4Sand

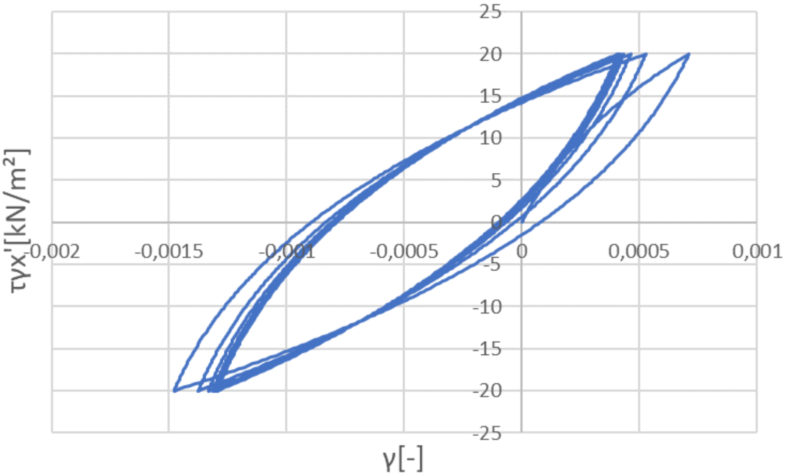

(b) Drained Sand Behavior under Cyclic Loading - PM4Sand

Figure 2.8: Comparison of Undrained and Drained PM4Sand Behavior

Chapter 3

Site Response Analysis and Liquefaction Assessment

The chapter begins by introducing SRA, which examines how shear waves from an earthquake propagate through the soil column, potentially amplifying or de-amplifying the seismic motion as it reaches the surface. This is a crucial step as SRA is the foundation of both the SF methods and the CDF.

Next, the chapter explores two methods for assessing the risk of liquefaction, as introduced in Section 2.1.2. These methods ultimately provide a SF to indicate the likelihood of liquefaction, as described by Equation 3.1. The CRR quantifies a soil's inherent ability to resist liquefaction under repeated loading conditions, while the CSR represents the stress imposed on the soil by seismic events. The SF is derived as the ratio of CRR to CSR, with a value above 1 indicating resistance to liquefaction and a value below 1 suggesting susceptibility.

$$SF = \frac{\text{Cyclic Resistance Ratio}}{\text{Cyclic Stress Ratio}} \tag{3.1}$$

The primary distinction between these methods lies in how the CSR and the CRR are calculated. Each approach applies different assumptions and corrections, reflecting variations in soil behavior and seismic input. A simplified workflow for these SF-based methods is presented in Figure 3.1.

Finally, the chapter introduces a CDF for liquefaction assessment, which predicts the maximum EPPR and uses it to calculate a ultimate shear strength degradation factor. This advanced method provides a more detailed analysis of soil behavior

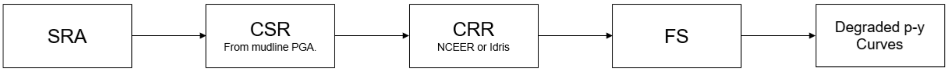

Figure 3.1: Workflow for the Safety Factor Based Methods

under seismic loading and is especially useful in scenarios where the simpler SF-based methods may not be sufficient. The workflow for this method is illustrated in Figure 3.2.

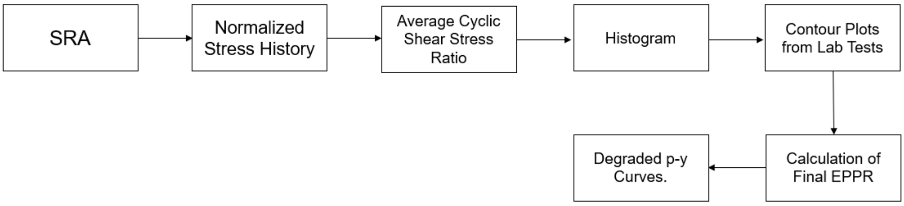

Figure 3.2: Workflow for the Contour Diagram Method

In the following sections, these methods are discussed in detail, focusing on their theoretical basis. The chapter aims to provide a comprehensive understanding of how to apply these methods effectively.

3.1 Site Response Analysis

In geotechnical engineering, the soil column—defined as a vertical section of soil extending from the surface to a specified depth—plays a crucial role in determining how seismic shear waves propagate through the subsurface. The response of this soil column is governed by its inherent properties, including shear modulus, unit weight, plasticity index and non-linear behavior at various strain levels. These properties influence whether seismic waves are amplified or attenuated as they travel toward the surface. Amplification is particularly problematic when the frequency content of the seismic motion aligns with the natural frequencies of the structure, potentially leading to resonant behavior and excessive dynamic responses.

In the context of OWTs, understanding the dynamic interaction between the foundation and the underlying soil is essential, given the long-term operational demands placed on these structures. Offshore environments often expose foundations to complex loading conditions, including seismic activity, which can induce significant ground motion. SRA is therefore a fundamental component of the design process, as it enables the prediction of acceleration, displacement, and strain profiles within the soil column. These outputs are critical for determining how the foundation will interact with the surrounding soil during seismic events and is essential part of the structural design of the OWT.

Moreover, the results of the SRA are not only pivotal for understanding seismic wave propagation but also serve as the foundation for applying both the SF and CDF methods for liquefaction assessment. A correctly conducted SRA ensures accurate predictions of PGA, which is fundamental input in the SF method. Additionally, the SRA results provide the necessary stress time histories for applying the CDF, which predicts EPPR. Without accurate SRA, the subsequent assessment of liquefaction potential and the design of wind turbine foundations would lack reliability.

A SRA usually includes the following steps.

- Soil data needs to be gathered by in-situ and lab testing. Crucial parameters are Shear Modulus, Shear Strength, Unit Weight, Plasticity Index, Over Consolidation Ratio.
- Soil Data is processed to extract the needed parameters so the analysis can be conducted.
- Those parameters along with selected seismic motions are then used to solve the PDEs that govern wave propagation and motion in an one dimensional soil column as illustrated in Equation 3.2.
- Finally, the results from the model are processed and the behavior of the soil column is assessed in terms of accelerations, displacements and eigenfrequencies.

$$\frac{\partial^2 u(z,t)}{\partial t^2} = \frac{1}{\rho(z)} \left(\frac{\partial}{\partial z} \left(G(z) \frac{\partial u(z,t)}{\partial z} \right) + \eta \frac{\partial^3 u(z,t)}{\partial t \partial z^2} \right) \tag{3.2}$$

where:

- $u(z,t)$ is the displacement in the soil at depth z and time t,
- $G(z)$ is the shear modulus of the soil as a function of depth,
- $\rho(z)$ is the density of the soil,
- $\eta(z)$ is the damping coefficient.

3.1.1 Numerical Model - DeepSoil V7.0

In this thesis, all SRA are performed by DEEPSOIL v7.0 developed by Prof. Youssef M.A. Hashash and others at the University of Illinois [25] and modelling choices and assumptions are based on the internship project that concluded before the start of this thesis [36].

DEEPSOIL is a widely used one-dimensional SRA program that can perform

- 1-D linear time and frequency domain analyses.
- 1-D equivalent linear frequency domain analyses including convolution and deconvolution
- 1-D nonlinear time domain analyses with and without pore water pressure generation.

3.1.2 The General Quadratic/Hyperbolic (GQ/H) Soil Model in DEEPSOIL

As outlined in Section 3.1.1, DEEPSOIL V7.0 is a widely used software for conducting one-dimensional seismic site response analyses (SRA). One of the advanced soil models available in DEEPSOIL is the General Quadratic Hyperbolic (GQ/H) model, which provides a more comprehensive approach to representing soil behavior under dynamic loading. This model is particularly effective in capturing both small-strain and large-strain behavior, making it suitable for a wide range of soil types. By incorporating shear strength control, the GQ/H model ensures realistic predictions of modulus reduction curves, correcting the underestimation of shear strength at large strains commonly found in simpler models like Darendeli's (2001) [14].

The GQ/H model is widely used in seismic analyses because it accurately models both the stiffness and damping behavior of soils, particularly during cyclic loading [22]. This section explains the formulation of the GQ/H model, the shear strength correction mechanism, and the key parameters required to apply the model effectively in DEEPSOIL.

Model Formulation

The GQ/H model provides a stress-strain relationship that combines hyperbolic and quadratic terms to fit modulus reduction curves accurately across a wide range of strain levels. The shear stress (τ) as a function of shear strain (γ) is described by:

$$\tau = \tau_{\text{max}} \left[\frac{1}{\theta_\tau} \left(1 + \left(\frac{\gamma}{\gamma_r} \right) - \sqrt{1 + \left(\frac{\gamma}{\gamma_r} \right)^2 - 4\theta_\tau \frac{\gamma}{\gamma_r}} \right) \right] \tag{3.3}$$

Where:

- τ_{max} is the maximum shear stress, representing the ultimate shear strength.
- $\gamma_r = \frac{\tau_{\text{max}}}{G_0}$ is the reference shear strain, which is the ratio of maximum shear stress to the initial shear modulus (G_0).
- θ_τ is a curve-fitting parameter calculated as:

$$\theta_\tau = \theta_1 + \theta_2 \frac{\theta_4 \left(\frac{\gamma}{\gamma_r} \right)^{\theta_5}}{\theta_3 + \theta_4 \left(\frac{\gamma}{\gamma_r} \right)^{\theta_5}} \tag{3.4}$$

This equation allows the model to adjust the modulus reduction curves and ensure the soil behavior is accurately represented across different strain ranges, while preventing underestimation of soil shear strength at large strains.

Shear Strength Correction

One of the core advantages of the GQ/H model is its ability to modify reference modulus reduction curves, such as those from Darendeli (2001)[14], at larger strains. These curves, which are typically derived from small strain data, tend to underestimate the soil's strength when extrapolated to higher strains. The GQ/H model incorporates a correction mechanism to ensure that the soil's shear strength at large strains is more accurately reflected. This is achieved by adjusting the modulus reduction curve through a process of shear strength correction.

The target shear strength is calculated using the Mohr-Coulomb equation:

$$\tau_{\text{target}} = c + \sigma'_v \tan(\phi) \tag{3.5}$$

Where:

- σ'_v is the effective vertical stress acting on the soil.
- ϕ is the soil's internal friction angle.
- c is the cohesion, often set to zero for cohesionless soils.

By implementing this correction, the GQ/H model ensures that predictions for soil behavior at large strains remain consistent with physical observations and do not underestimate the actual shear strength.

Model Parameters

The GQ/H model requires the following key parameters:

- G_0: The initial shear modulus, typically determined from shear wave velocity (V_s).
- $\tau_{\max}$: The maximum shear stress.
- γ_r: The reference shear strain.
- θ_1 to θ_5: Curve-fitting parameters used to adjust the modulus reduction curve for different soils which come from the shear modulus degradation and damping curves selected.

3.1.3 Key Aspects of Site Response Analysis in DEEPSOIL v 7.0

This section highlights the fundamental analytical methods and key considerations that directly influence the reliability and accuracy of SRA in DeepSoil V7.0. By carefully selecting appropriate modeling techniques, soil parameters, and wave propagation characteristics, it can be ensured that soil behavior under seismic loading is accurately predicted. Understanding these aspects is essential for optimizing the analysis process and ensuring that the results accurately reflect the soil column response during seismic events.

Table 3.1 summarizes the key aspects of the analysis, and the following list provide a more detailed explanation of each modelling choice:

- **Analysis Types and Soil Behavior:**
    - *Equivalent Linear (EQL) vs. Nonlinear (NL) Analysis:* EQL and NL analyses are the two primary methods used in SRA. Nonlinear analysis is recommended when shear strains exceed 0.1%, as it better captures the nonlinear soil behavior under large strains [28]. Additionally, for cases involving liquefaction, NL analysis is essential since it considers the full stress time history, while EQL operates solely in the frequency domain.

Table 3.1: Key Aspects of SRA in DEEPSOIL V7.0

Analysis Type	Nonlinear
Soil Model	General Quadratic Hyperbolic
Shear Modulus Degradation and Damping Curves	Darendeli
Default Hysteretic Re/Unloading Formulation	Problem Dependent
Damping Mechanisms	Problem Dependent
Discretization of Soil Layers	Input Frequency Dependent

  - *General Quadratic Hyperbolic (GQH) Soil Model:* For Nonlinear analysis, the General Quadratic Hyperbolic (GQ/H) soil model is widely employed to represent the behavior of soils under cyclic loading. As detailed in Section 3.1.2, the GQ/H model accurately captures the nonlinear stress-strain relationship in soils, providing a realistic depiction of how soils respond to dynamic loading. This model is particularly useful because it accounts for both the reduction in shear modulus and the increase in damping as strains increase. Accurately modeling this nonlinear and hysteretic behavior is crucial for reliable predictions of how seismic waves propagate through the soil column during an earthquake.

- **Choice of Damping and Shear Modulus Degradation Curves:**

  - *Darendeli's Curves and Other Models:* The choice of damping and shear modulus degradation curves plays a critical role in determining the accuracy of SRA. Darendeli's empirical models [14] are widely used due to their ability to incorporate factors like confining pressure, plasticity index, shear strength, and overconsolidation ratio as illustrated in Figure 3.3. These curves describe how the shear modulus decreases and damping ratio increases with increasing shear strain, allowing for more precise simulations of dynamic soil behavior under cyclic loading.

- **Masing and Non-Masing Hysteresis Rules:**

  - *Energy Dissipation via Hysteretic Loops:* The application of Masing rules during cyclic loading often results in larger hysteretic loops, which increase damping ratios and energy dissipation [26]. This can influence the predicted response of soils, especially in high-strain scenarios where nonlinear behavior becomes pronounced.

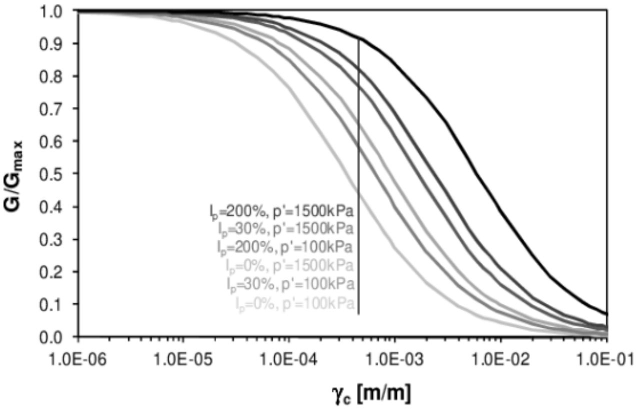

(a) Darendeli Family Shear Modulus Degradation Curve

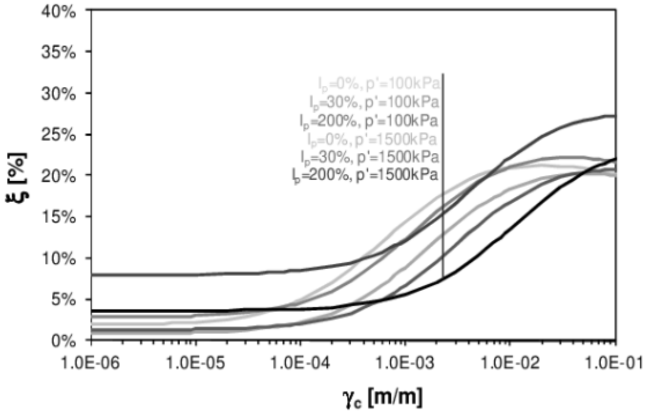

(b) Darendeli Family Damping Ratio Curve

Figure 3.3: Darendeli Family Curves. Source: [23].

- **Damping Mechanisms:**
  - *Rayleigh Damping vs. Frequency-Independent Damping:* In the absence of specific Rayleigh damping coefficients, it is advisable to apply frequency-independent damping. This approach provides consistent and uniform damping across the frequency spectrum of the seismic input, reducing the potential for frequency-dependent anomalies and ensuring that damping effects are distributed evenly across the model.
- **Discretization of Soil Layers:**
  - *Shear Wave Propagation Accuracy:* Proper discretization of soil layers is crucial for accurately capturing shear wave propagation. The maximum frequency content that a soil layer can propagate is defined by Equation 3.6. By adjusting the thickness of the layers H, the numerical model can better propagate the frequency content of the seismic input, reducing the risk of numerical inaccuracies due to waves not propagating correctly.

$$f_{max} = \frac{V_s}{4H} \tag{3.6}$$

- **Influence of Soil Properties:**
  - *Plasticity Index and Neutral Earth Pressure Coefficient:* Among soil properties, the Plasticity Index plays a significant role in influencing SRA results, whereas the neutral earth pressure coefficient K_0 is less impactful, provided that reasonable values are used.
- **Adjusting for Shear Strength in Non-Cohesive Soils:**
  - *Correction for Shear Wave Velocity in Darendeli's Curves:* While Darendeli's curves are widely used, they do not directly account for the influence of shear wave velocity. Therefore, it is necessary to adjust the shear strength of non-cohesive materials by introducing the correction factor C_{Vs} as shown in Equation 3.7. This adjustment ensures a more accurate reflection of the soil's behavior under seismic loading, as proposed by Harmon [24].

$$\tau_{Sand} = C_{Vs} + \sigma'_{v0} * tan(\phi) \tag{3.7}$$

$$C_{Vs} = \rho \times V_s^2 \times 0.80 \times 0.1\% \geq 10\,\text{kPa} \tag{3.8}$$

An overview of the typical workflow for Seismic Response Analysis (SRA) can be found in Figure 3.4.

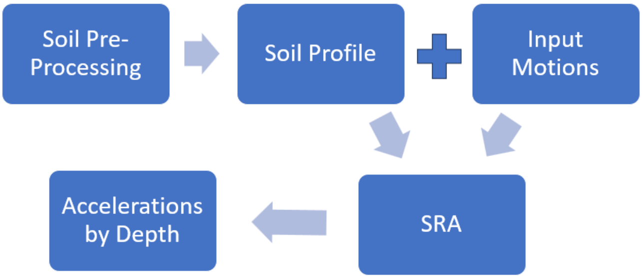

Figure 3.4: SRA Workflow

3.2 Liquefaction Assessment in the Form of a Safety Factor

In geotechnical engineering, especially in the context of OWT foundations, the assessment of liquefaction potential is paramount due to the potential for seismic-induced ground failure. Quantifying liquefaction potential is typically achieved through the use of SFs, which are derived from a comparison between CSRs and CRRs. This section aims to outline the theoretical basis and computational methodologies for calculating these SFs, providing a foundation for subsequent analyses in liquefaction risk assessment.

To ensure a comprehensive understanding of liquefaction mechanisms, several established methods are employed, each offering unique advantages depending on the specific site conditions and soil properties. Two widely used approaches in this domain are the Idriss and Boulanger [8] method and the NCEER (Youd et al., 2001) [40] method. The following subsections delineate the application of each approach, emphasizing the computational nuances and underlying assumptions that contribute to their respective efficacy in predicting liquefaction potential.

3.2.1 Liquefaction According to Idriss and Boulanger

The Idriss and Boulanger [8] method is widely used to assess liquefaction potential in engineering design. This section outlines the step-by-step process.

CRR is usually correlated to an in-situ parameter [8]. In this thesis, the parameter used is tip resistance q_c. To make the resistance comparable with the calculated stress, an overburden correction factor C_n and an equivalent clean sand adjustment for fines content need to be applied.

Overburden Correction Factor

The overburden correction factor C_n is given by

$$C_n = \frac{P_\alpha}{\sigma_{v0}}^{m} \tag{3.9}$$

where m is

$$m = 1.338 - 0.249(q_{c1Ncs})^{0.264} \tag{3.10}$$

$$q_{c1N} = \left(\frac{P_a}{\sigma'_{v0}}\right)^{m} \frac{q_c}{P_a} \tag{3.11}$$

Thus, m is directly dependent on the calculated value of the normalized tip resistance. To calculate it, simple iterations with a MATLAB script or an Excel file are needed.

Clean Sand Adjustment for Fines Content

After the normalized tip resistance q_{c1N} is calculated, the correction for fines content can be applied, which is given by the following formula as a function of fines content in % and the normalized tip resistance q_{c1N}

$$\Delta q_{c1N} = (11.9 + \frac{q_{c1N}}{14.6}) exp(1.63 - \frac{9.7}{FC+2} - (\frac{15.7}{FC+2})^2) \tag{3.12}$$

Then the normalized tip resistance for both the overburden stress and the fines content can be calculated:

$$q_{c1N_{cs}} = q_{c1N} + \Delta q_{c1N} \tag{3.13}$$

Cyclic Resistance Ratio Calculation

Once the previous calculations are done, the final value for the CRR can be calculated.

$$CRR_{M=7.5,\sigma'=1\text{atm}} = \exp\left(\frac{q_{c1N_{cs}}}{113} + \left(\frac{q_{c1N_{cs}}}{1000}\right)^2 - \left(\frac{q_{c1N_{cs}}}{140}\right)^3 + \left(\frac{q_{c1N_{cs}}}{137}\right)^4 - 2.80\right) \tag{3.14}$$

3.2.2 Liquefaction According to NCEER (Youd et al. 2001)

The NCEER method, as outlined by Youd et al. (2001)[40], is another widely recognized approach for assessing liquefaction potential. This method utilizes empirical relationships based on CPT data to evaluate liquefaction risk similarly to Section 3.2.1.

First, the soil needs to be classified as liquefiable or not through the calculation of the soil behavior type index I_c [40]. Following this classification, similar to the procedure outlined in Section 3.2.1, the cone tip resistance should be normalized and corrected for fines content.

Calculation of Soil Behavior Type Index

The soil behavior type index is calculated by the following formulas:

$$Q = [\frac{(q_c - \sigma_{vo})}{P_\alpha}][(\frac{P_\alpha}{\sigma'_{vo}})^n] \tag{3.15}$$

$$F = [\frac{f_s}{q_c - \sigma_{vo}}] \times \% \tag{3.16}$$

$$I_c = [(3.47 - log(Q))^2 + (1.22 + log(F))^2]^{0.5} \tag{3.17}$$

The first step is to identify clayey soils. To do that, an exponent $n = 1$ must be used. If the I_c calculated with $n = 1$ is greater than 2.6, the soil is classified as clayey and is considered too clay-rich to liquefy.

If the calculated I_c is smaller than 2.6, the soil is most likely granular, and Q should be calculated with an exponent of $n = 0.5$. For this calculation, C_q should be calculated with an exponent of 0.5 and q_{c1N} substituted for Q in equation 3.17. If I_c is now less than 2.6, the soil is non-plastic and granular, and this I_c can be used to calculate liquefaction resistance. If I_c is now greater than 2.6, the soil is likely to be very silty and plastic. Then, an exponent of $n = 0.7$ needs to be used to calculate q_{c1N} and I_c.

Normalized Tip Resistance Calculation

The tip resistance needs to be normalized for overburden stress to make it dimensionless. To do that, equation 3.18 is used.

$$q_{c1N} = \left(\frac{P_a}{\sigma'_{v0}}\right)^n \frac{q_c}{P_a} \tag{3.18}$$

Sections 3.2.2 and 3.2.2 are connected and must be calculated at the same time.

Calculation of Clean Sand Equivalent Normalized Cone Penetration Resistance

To correct the normalized penetration resistance q_{c1N} to an equivalent clean sand value, equation 3.19 is used.

$$(q_{c1N})_{cs} = K_c q_{c1N} \tag{3.19}$$

Here K_c is defined by the following formulas according to Robertson and Wright [40]:

$$For \quad I_c \leq 1.64 \qquad K_c = 1 \tag{3.20}$$

$$For \quad I_c > 1.64 \qquad K_c = -0.403 I_c^4 + 5.581 I_c^3 - 21.63 I_c^2 + 33.75 I_c - 17.88 \tag{3.21}$$

Cyclic Resistance Ratio Calculation

After the procedure described in the previous paragraphs is completed, the final CRR of the soil layer can be calculated using equation 3.22.

$$CRR_{M=7.5,\sigma=1\text{atm}} = \begin{cases} 0.833\left(\frac{q_{c1N_{cs}}}{1000}\right) + 0.05 & \text{if } q_{c1N_{cs}} \leq 50 \\ 93\left(\frac{q_{c1N_{cs}}}{1000}\right)^3 + 0.08 & \text{if } q_{c1N_{cs}} > 50 \end{cases} \tag{3.22}$$

3.2.3 Earthquake Induced Cyclic Stress Ratio

The earthquake-induced CSR at a specific depth z within the soil profile is typically represented by an equivalent uniform value. This value is conventionally taken as 65% of the peak CSR, as indicated by previous studies [8], and is expressed in equation 3.23.

$$CSR_{M,\sigma'_{v0}} = 0.65 \frac{\sigma_v}{\sigma'_{v0}} \frac{a_{max}}{g} r_d \tag{3.23}$$

where σ_v and σ'_v is the vertical total and effective stress at depth z respectively, a_{max}/g is the maximum horizontal acceleration (as a fraction of gravity) at the ground surface, and r_d is the shear stress reduction factor that accounts for the dynamic response of the soil profile. As this value is dependent on the duration of the shaking (energy released) and the effective overburden stress, it needs to be normalized to a magnitude of 7.5 and an effective overburden stress of 1 atm.

$$CSR_{M=7.5,\sigma=1\text{atm}} = CSR \times \frac{1}{MSF} \times \frac{1}{K_\sigma} \times r_d \tag{3.24}$$

Calculation of Magnitude Scaling Factor

The magnitude scaling factor (MSF) is used to account for duration effects (i.e., the number and relative amplitudes of loading cycles) on the triggering of liquefaction. The following relationship is proposed by Idriss and Boulanger [8].

$$MSF = 1 + (MSF_{\text{max}} - 1)\left(8.64\exp\left(\frac{-M}{4}\right) - 1.325\right) \tag{3.25}$$

Where MSF_{max} is

$$MSF_{\text{max}} = 1.09 + \left(\frac{q_{c1N_{cs}}}{180}\right)^3 \leq 2.2 \tag{3.26}$$

and $q_{c1N_{cs}}$ is the normalized tip resistance as calculated in 3.2.2 or 3.2.1 depending on the method used.

Calculation of Overburden Correction Factor

The Overburden Correction Factor K_σ is calculated from Equation 3.27.

$$K_\sigma = 1 - C_\sigma \ln\left(\frac{\sigma'_v}{P_\alpha}\right) \tag{3.27}$$

$$C_\sigma = \frac{1}{37.3 - 8.27(q_{c1N_{cs}})^{0.264}} \leq 0.3 \tag{3.28}$$

Calculation of the Depth Stress Reduction Factor

To account for the stress reduction per depth, Idriss proposed that the parameter r_d could be expressed as

$$r_d = exp[\alpha(z) + \beta(z) \times M] \tag{3.29}$$

$$\alpha(z) = -1.012 - 1.126sin(\frac{z}{11.73} + 5.133) \tag{3.30}$$

$$\beta(z) = 0.106 + 0.118sin(\frac{z}{11.28} + 5.142) \tag{3.31}$$

3.2.4 Calculation of the Final Safety Factor

Once both the CSR and the CRR have been calculated with either or both methods, the final SF for liquefaction can be calculated as

$$SF_{Nceer} = \frac{CRR_{Nceer}}{CSR} \quad SF_{Idriss} = \frac{CRR_{Idriss}}{CSR} \tag{3.32}$$

3.3 Contour Diagram Framework

The CDF builds upon the work of Andersen (2015)[2], and offers an advanced method for evaluating EPP accumulation in soils subjected to cyclic loading. Unlike traditional SF methods, this framework provides a more precise prediction of soil behavior under dynamic conditions, making it particularly valuable in seismic design for complex structures like OWTs.

This method addresses the limitations of simpler approaches, which may not fully capture the complexity of soil behavior during seismic events. By incorporating a time-history approach, the CDF predicts not only EPPR but also provides critical information such as the maximum CSR and the equivalent number of cycles per depth, offering a more comprehensive understanding of liquefaction potential.

The accuracy of this method depends on the results from the SRA, which provides the necessary CSR data. This data is essential for determining the amplitude and number of loading cycles for each soil layer, ensuring that the CDF accurately reflects dynamic soil conditions.

This section outlines the theoretical foundation of the CDF and defines the procedure needed to calculate the maximum CSR, equivalent number of cycles, and EPPR for a soil column from start to finish.

3.3.1 Site Response Analysis

SRA is conducted on the soil column using ground motions that correspond to the required design life and match the design spectrum for the specific area, as described in Section 3.1. Upon completion, time-stress histories for the middle of each layer are extracted.

3.3.2 Extraction of the Average Cyclic Shear Stress Ratio

The average CSR τ_{cyc}/σ'_{v0}, where τ_{cyc} is the shear stress induced in the soil due to cyclic loading, σ'_{v0} is the initial effective vertical stress, is calculated for each loading cycle. The calculation of these values depends on the cycle counting method selected.

This process is illustrated in Figure 3.5 where RPC method was used and the maximums were marked with magenta and minimums with light blue.

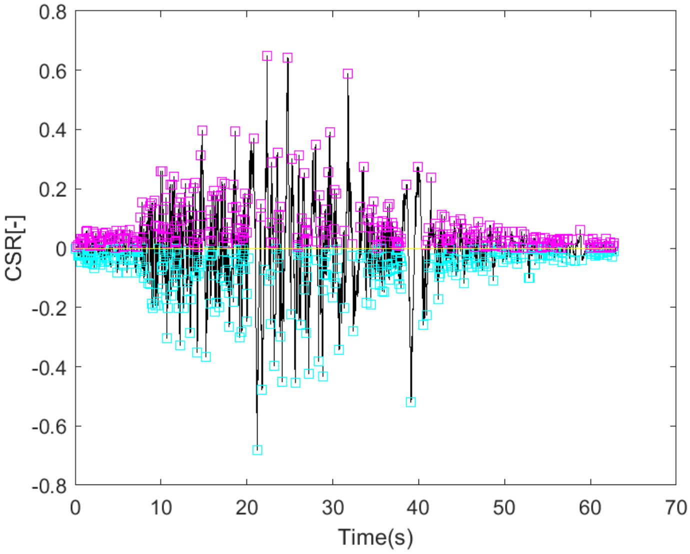

Figure 3.5: Stress Time History with Maximums Marked in Magenta and Minimums in Light Blue.

Once the extreme values per half cycle are found then equation 3.33 is used to find the average CSR for each cycle.

$$\tau_{cyc}/\sigma'_{v0} = \frac{(\tau_{max}/\sigma'_{v0} - \tau_{min}/\sigma'_{v0})}{2} \tag{3.33}$$

Equation 3.33 represents the average CSR, where τ_{cyc} is the cyclic shear stress, σ'_{v0} is the initial effective vertical stress, τ_{max} is the maximum CSR encountered between two consecutive zero crossings of the CSR time history, and τ_{min} is the minimum CSR encountered between the same two consecutive zero crossings.

In this context, the ”zero crossings” refer to the points in time where the CSR changes direction, crossing the zero stress line.

The same process is repeated with the signal inversed to make sure that no significant loading cycles are skipped by the cycle counting process.

Similarly, the number of cycles and their amplitude can be determined using a conventional RFC algorithm. However, based on the findings of this thesis, RPC has demonstrated superior performance when implemented with the CDF as illustrated in Section 5.5. Therefore, it has been chosen for use in this context .

3.3.3 Cyclic Stress Histogram

The calculated CSR cycles are converted into a histogram that illustrates the frequency of each encountered CSR. In this thesis, each bin represents an interval of 0.01, as shown in Figure 3.6. The ”Forward Signal” refers to identifying the maximum and minimum points by analyzing the signal in its original sequence, while ”Inverse Signal” refers to performing the same analysis after reversing the signal in time.

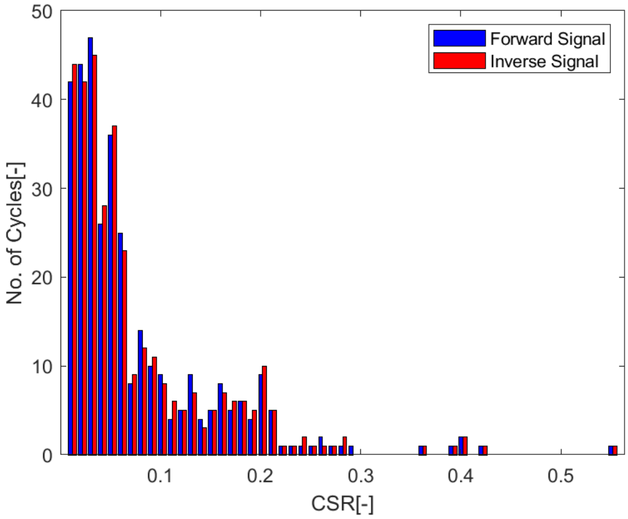

Figure 3.6: Histogram of Stress Cycles with Each Bin Representing 0.01 Stress Ratio.

Load parcels are created in this manner and then are used to determine the EPPR through the contour graph.

3.3.4 Development of Excess Pore Pressure Contour Diagrams

EPPR contour diagrams need to be developed in the lab for each soil layer. This is usually done through undrained CDSS or triaxial tests.

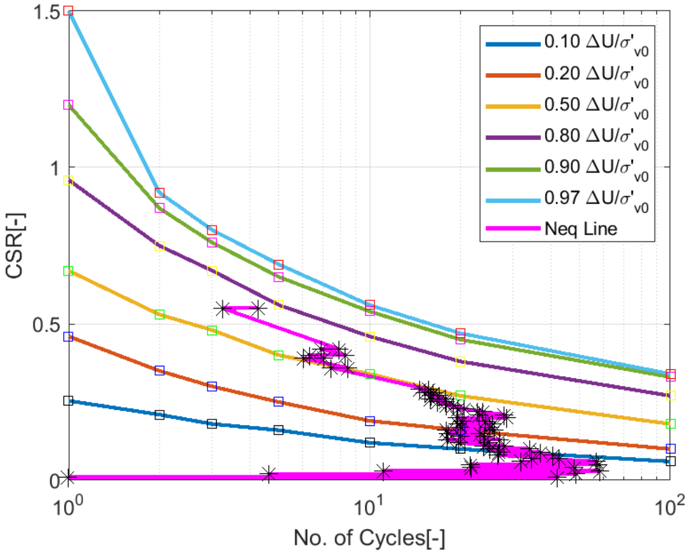

Figure 3.7: Example of an Excess Pore Pressure Ratio (EPPR) Contour Diagram.

3.3.5 EPPR Accumulation Analysis

Analyzing EPP accumulation involves using the CSR histogram and depth-specific EPPR contour diagrams constructed earlier as proposed by Andersen [2]. The maximum EPPR at the end of the earthquake is determined as $\Delta u/\sigma'_{v0}$ corresponding to the equivalent number of cycles (Neq) following the application of the final histogram bin showing the highest τ_{cyc}/σ'_{v0} induced by the earthquake. The value of Neq is associated with earthquake magnitude (higher magnitudes lead to more cycles), but Neq is also influenced by other factors such as the level of strength mobilization (weaker soils may suppress higher shear stresses, resulting in more cycles of lower stress magnitude) and the specific shape of the contour curves for each soil type [12]. The line following this procedure can be seen in Figure 3.7.

3.4 Modelling Liquefaction

After the SF for the CPT-based methods or the EPPR for the contour-based method has been calculated, it is necessary to account for liquefaction in the design, especially in cases such as OWTs, where soil improvements cannot be implemented.

To address this need, the Japanese Road Association [27] provides a factor to degrade the ultimate strength of the liquefied layer. The degradation factor depends on the SF, depth from the surface, CRR and the significance of the project under examination.

Table 3.2: JRA Degradation Factors.

Range of SF	Depth from Ground Surface (m)	Level 1 Significance		Level 2 Significance	
		$CRR \geq 0.3$	$0.3 < CRR$	$CRR \geq 0.3$	$0.3 < CRR$
$SF \leq 1/3$	$0 \leq x \leq 10$	1/6	0	1/3	1/6
	$10 < x \leq 20$	2/3	1/3	2/3	1/3
$1/3 < SF \leq 2/3$	$0 \leq x \leq 10$	1	1	1	2/3
	$10 < x \leq 20$	1	2/3	1	1
$2/3 < SF \leq 1$	$0 \leq x \leq 10$	1	1	1	1
	$10 < x \leq 20$	1	1	1	1

For the contour-based method, after the EPPR is calculated according to Section 3.3, Equation 3.34 from Boulanger [9], based on the experiments from Dobry et al. [18], is used to calculate the p-Multiplier or Degradation Factor (De), which will be the term used in this thesis, as shown in Figure 3.8. Equation 3.34 is chosen over Equation 3.35 because Figure 3.8 indicates that the latter is more conservative. When combined with the inherently conservative nature of the CDF, as discussed in Section 5.5, the alternative approach is considered excessively conservative.

$$m_p = 1 - 0.9 * r_u \tag{3.34}$$

$$m_p = 1 - 0.95 * r_u \tag{3.35}$$

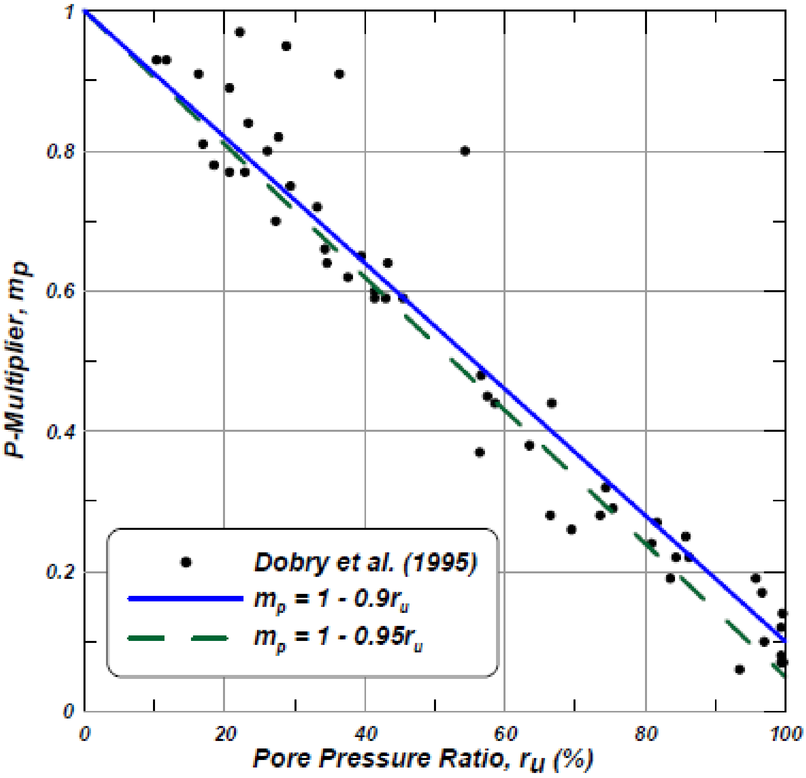

Figure 3.8: Relationship Between p-Multiplier/Degradation Factor and Pore Pressure Ratio for Post-Liquefaction Cyclic Loading of Sand [18].

Chapter 4

Validation of the Tools Developed

This chapter focuses on the validation of the liquefaction assessment tools developed in this thesis, to apply the methods outlined in Chapter 3, using real project data from SGRE. The results produced by the developed tools are compared against those from a confidential report to assess whether the tools accurately implement the NCEER, Boulanger & Idriss, and CDF methods.

The objective is to ensure that the tools correctly apply the methods and provide reliable predictions. Differences in results, particularly in terms of SF and EPPR, are closely analyzed to identify any potential errors in the application of the methods. Additionally, the results from the SF methods and the CDF will be compared in terms of SF, EPPR, and ultimate strength degradation factors, providing a comprehensive evaluation of the tools' performance and their applicability for practical engineering assessments.

This chapter will:

1. Compare the results obtained from the developed tools with those of the confidential report to ensure their robustness.

2. Compare the results between the SF and the CDF methods to identify any discrepancies or areas where one method may be more conservative or detailed than others.

4.1 NCEER and Boulanger & Idriss Methods

The NCEER and Boulanger & Idriss methods, which were extensively discussed in Sections 3.2.1 and 3.2.2, are applied in this chapter to evaluate liquefaction potential based on project data. The primary objective here is to ensure that the developed tools correctly implement these methods. This is achieved by comparing the results produced by the tools against those obtained from the confidential report.

To perform this comparison, CPT data was obtained by digitizing graphs from the confidential report. Although the digitization process provides a realistic representation of the soil profile, it is important to note that this process is not 100% accurate. Small errors can arise during the digitization of the graphs, potentially leading to minor discrepancies in the results.

Furthermore, fines content data was not available in the original report, so an estimate was calculated from I_c (Equation 3.17) using the methodology proposed by Robertson and Wride [32]. This estimation introduces an additional factor of uncertainty into the calculations when applying corrections for fines content during liquefaction assessment.

$$\text{If } I_c < 1.6, \quad \text{FC} = 0\%$$
$$\text{If } 1.6 \leq I_c \leq 3.5, \quad \text{FC} = 1.75 \cdot I_c^{3.25} - 3.7$$
$$\text{If } I_c > 3.5, \quad \text{FC} = 100\%$$

Table 4.1 provides earthquake data, which was used to ensure that the PGA and magnitude values were consistent for comparison purposes.

Table 4.1: Earthquake Magnitude and Corresponding Peak Ground Acceleration (PGA)

Earthquake Magnitude (Mw)	PGA (g)
6.8	0.120
6.8	0.129
6.8	0.120
6.8	0.123
6.8	0.114
6.8	0.132

The CRR and CSR, calculated from the CPT data and the given motions, are then used to estimate the SF. By reproducing these results with the developed tools, their accuracy and reliability can be validated.

SFs for all PGAs were calculated and their means were plotted by depth. Results from the developed code are shown in Figures 4.1a ,4.1b.

The foundation designer also provided their results for the same methods, which were used to verify if the developed code is functioning as expected. Their results are presented in Figure 4.2.

It can be observed that the SF results from both methods are comparable, with the NCEER method showing slightly less accuracy than the Idriss and Boulanger method. This discrepancy likely stems from an unclear application of the NCEER method in the report, where deviations from the procedure outlined by Youd et al. (2001) may have occurred. Additionally, minor errors were introduced in both methods due to the digitization of the CPT graphs and the absense of fines content percentage, as previously discussed.

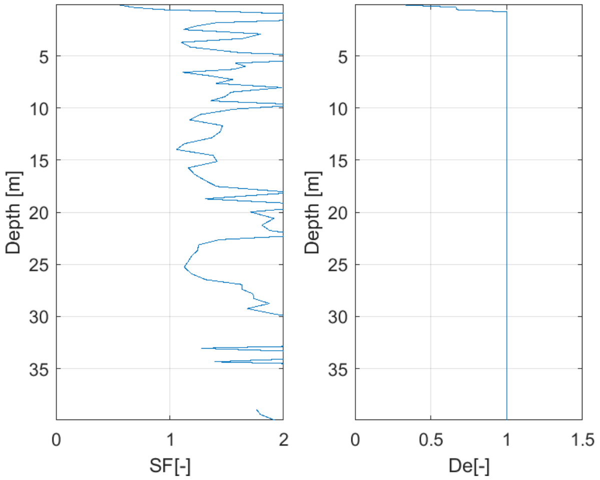

(a) Safety and Degradation Factor According to NCEER (Youd et al., 2001) [40]

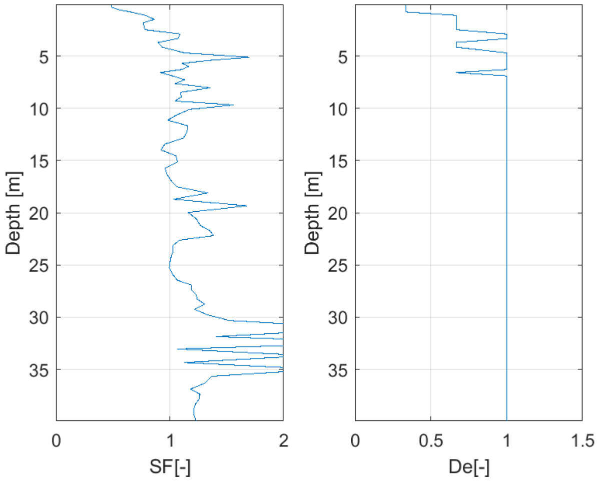

(b) Safety and Degradation Factor According to Idriss and Boulanger (2014) [8]

Figure 4.1: Safety and Degradation Factors from the Safety Factor Based Methods.

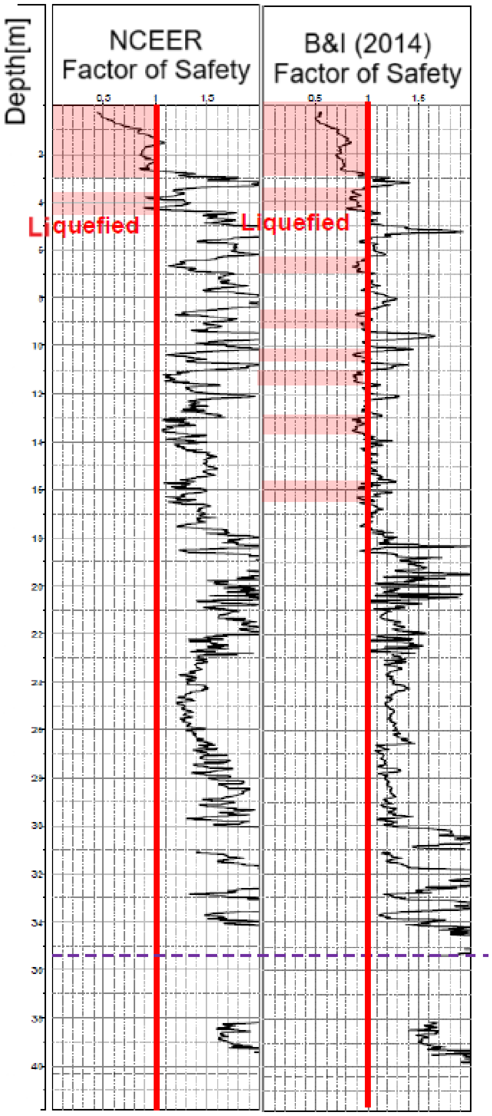

Figure 4.2: Safety Factor According to NCEER and Idriss & Boulanger(2014), Source: [12]

4.2 Contour Diagram Framework

The CDF, as outlined in 3.3, is applied in this section to evaluate the liquefaction potential using the same project data. The primary goal is to ensure that the tools developed for the CDF correctly predict the EPPR. As in Section 4.1, these results are compared with the values obtained from the confidential report to validate the accuracy of the developed tools.

Once the developed tools have been validated, the results from the CDF are compared with those obtained from the SF methods. This comparison provides a more comprehensive understanding of liquefaction potential, particularly in terms of EPPR, SF, and degradation factors, offering insights into the differences between these two approaches.

4.2.1 Site Response Analysis

SRA is the essential first step of the CDF, as it provides the necessary CSR time series which is the foundation for evaluating liquefaction potential. In this section, SRA was conducted using ground motions that correspond to the expected design life and seismic conditions of the project area.

The selected motions, shown in Table 4.2 , include shallow crustal events (Loma Prieta) and subduction zone events (Michoacan).

Table 4.2: Representative Earthquakes

Type	Year	Earthquake	Station	Mw	1st ID	2nd ID
Shallow Crustal	1989	Loma Prieta, USA	Woodside	6.93	WDS000	WDS090
Subduction	1985	Michoacan, Mexico	La Union	8.1	UNIO000	UNIO090

The motions are first matched to an outcrop spectrum for bedrock of $V_s = 315 m/s$, as shown in Figure 4.3, using the program SeismoMatch 2024 [35]. The match is not perfect as the academic version does not allow for low error tolerance thresholds so some deviation is expected, especially for lower periods.

A model is then created in DeepSoil v7 [25] according to the recommendations in Section 3.1. In Figure 4.4 , the given Vs and Shear Strength are shown. These values were directly taken from the plots in the confidential project report. No further soil data was available, so other needed soil parameters like OCR and PI were estimated

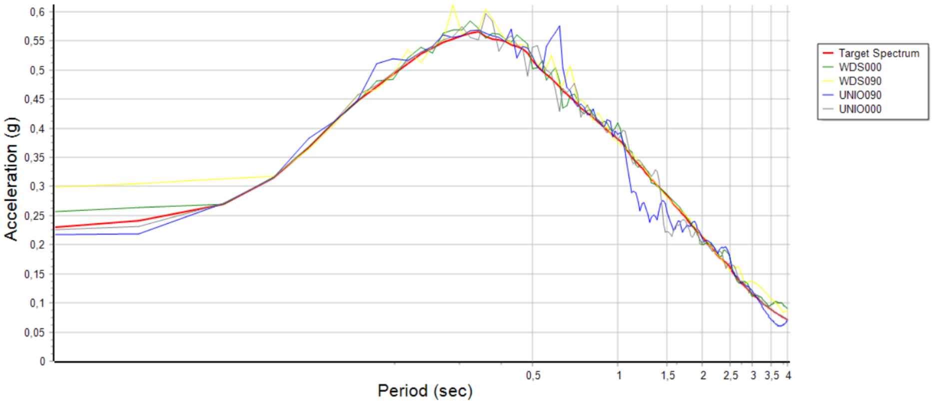

Figure 4.3: Outcrop Spectrum with Matched Motion Spectra

from CPT values using a SGRE in-house tool. Bedrock was set as elastic since an outcrop motion is used, and damping was set at 1%.

The degradation curves chosen are by Darendeli [14]. The foundation designer in the project report used custom-fit damping and shear modulus degradation curves which were not provided as data, with only few graphs available. In terms of damping, Figure 4.5 shows that Darendeli curves and the project curves differ significantly, which is expected to increase the response output of the DeepSoil model. Analysis is non-linear, without EPP generation, with Masing rules which usually leads to higher damping to decrease deviation in the response.

Once the analysis is completed, The spectral accelerations at the mudline were plotted and compared with the confidential report to assess the results of the analysis, as shown in Figure 4.6. The lines to compare are the blue Excel line and the dashed blue line in the background.

As expected, the difference in damping and the imperfect spectral matching because of higher error tolerance of the academic version leads to a larger response, especially for smaller periods. This is crucial for the next step, as a larger response translates to higher CSRs when applying the subsequent steps of the method.

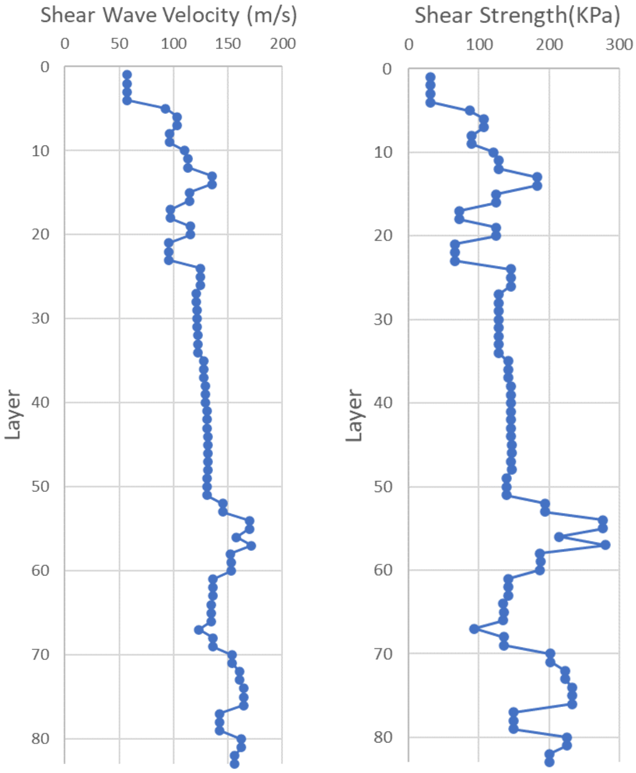

(a) Shearing Wave Velocity Profile

(b) Shear Strength Profile

Figure 4.4: DeepSoil v7.0 Input

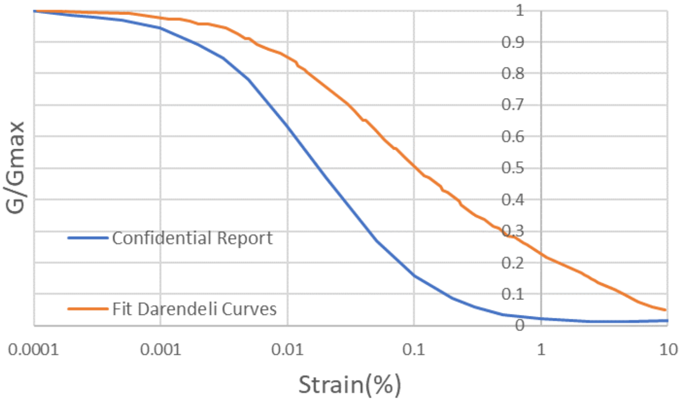

(a) Shear Modulus Degradation Curves Comparison

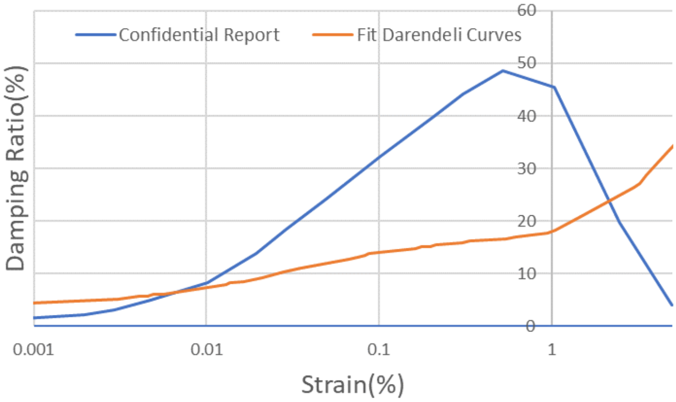

(b) Damping Curves Comparison

Figure 4.5: Comparison of Shear Modulus Degradation and Damping Curves

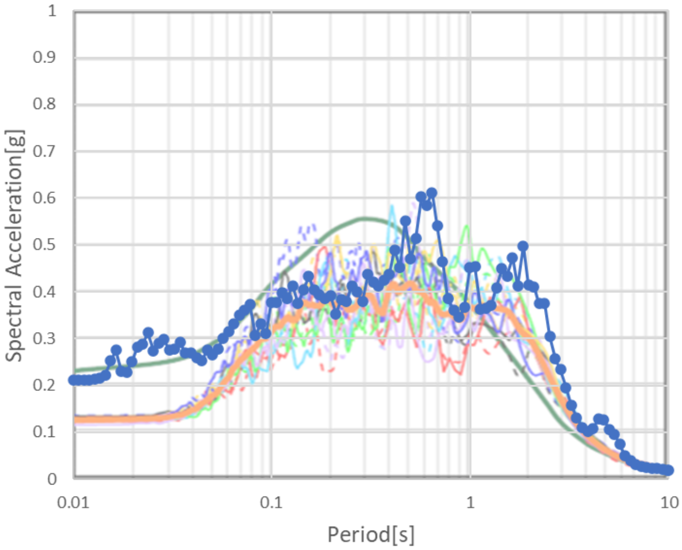

Figure 4.6: Spectral Accelerations at Mudline

4.2.2 Extraction of the Average Cyclic Stress Ratio

Following the SRA, the CSR time histories at different depths are analyzed to extract the CSR of each cycle as outlined in Section 3.3.2. The confidential report employed RPC, and thus the same method was selected for consistency in this analysis.

Following the steps explained in Section 3.3.2, the maximum and minimum values per cycle are located, as illustrated in Figure 4.7, where the CSR time history with maximum and minimum values for each cycle is exhibited. The average CSR for each cycle is then calculated with Equation 3.33.

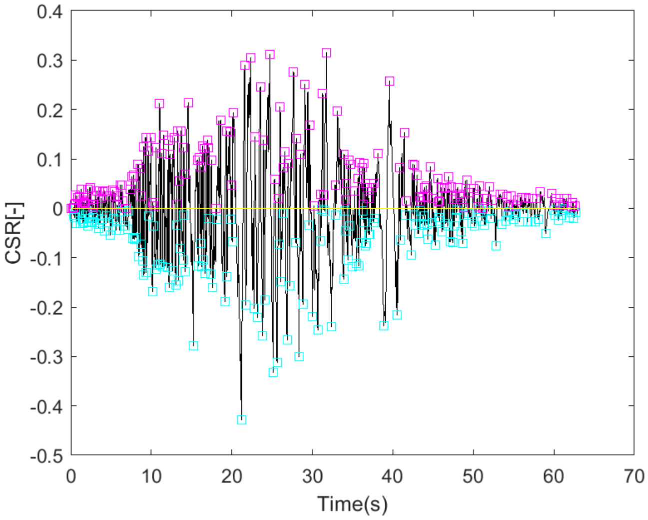

Figure 4.7: Cyclic Stress Ratio Time History with Maximum and Minimum Values per Cycle, UNIO090, Depth = 2.46 m

4.2.3 Cyclic Stress Histogram

After calculating the CSR for each cycle, the CSR cycles are categorized into bins to create a CSR histogram as described in Section 3.3.3. This histogram represents the distribution of CSR values encountered during the seismic event which essentially are the loading parcels of the CDF.

In this analysis, the CSR values are grouped into bins with an interval of 0.01. Each bin represents the frequency of encounter of a particular CSR, as shown in Figure 4.8.

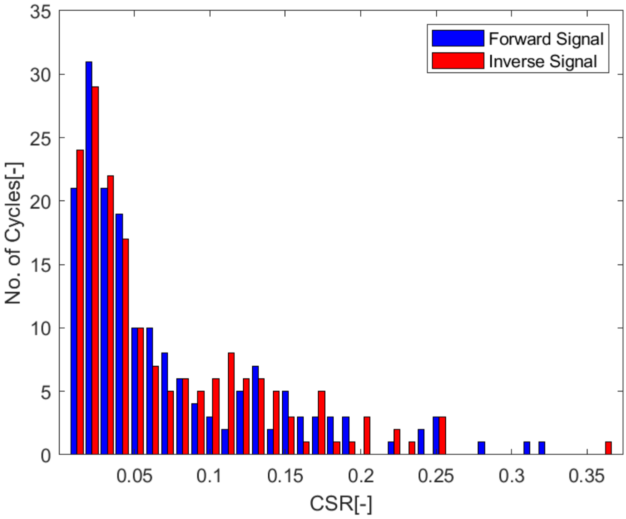

Figure 4.8: Histogram of the Loading Cycles, UNIO090, Depth = 2.46m.

4.2.4 EPPR Accumulation Analysis

The accumulation of EPPR is evaluated using the loading parcels generated in the previous step. For each bin in the histogram, the corresponding stress cycles are applied to the EPP contour diagrams. This process calculates the final EPPR at different depths, using a modified version of SGRE's in-house tools. The final output includes the equivalent number of cycles N_{eq}, the maximum CSR τ_{max}/σ'_{v0} , and the EPPR accumulated from the motion. Figure 4.9 shows the contour diagram provided by the SGRE foundation designer, while Figure 4.10 shows the output of the developed code. EPPR for the first diagram is 0.30, while EPPR for the latter is 0.40. This difference is expected due to the larger response from the SRA, as explained in Section 4.2.1.

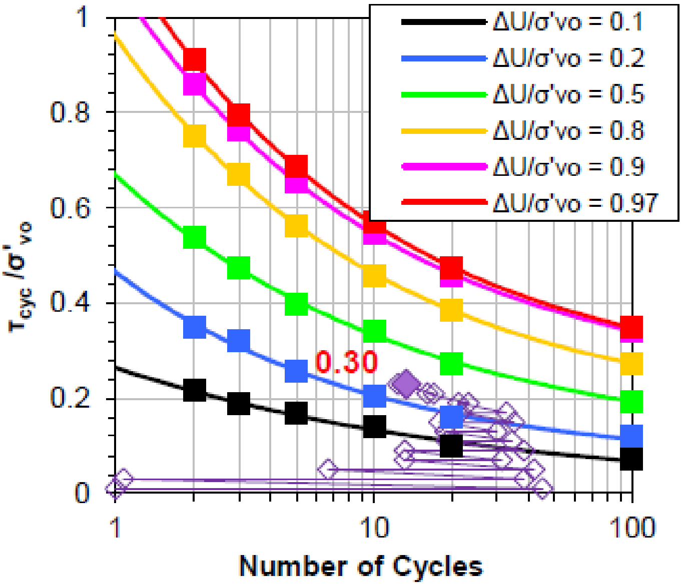

Figure 4.9: Exemplary Contour Plot for the Same Depth and Motion, Depth 2.35m, SGRE Project [12]

The same procedure was repeated for all motions and each soil layer. The results are presented in Figure 4.11. Unfortunately, the report does not clearly indicate which depth corresponds to which contour plot, and only a few examples are pro-

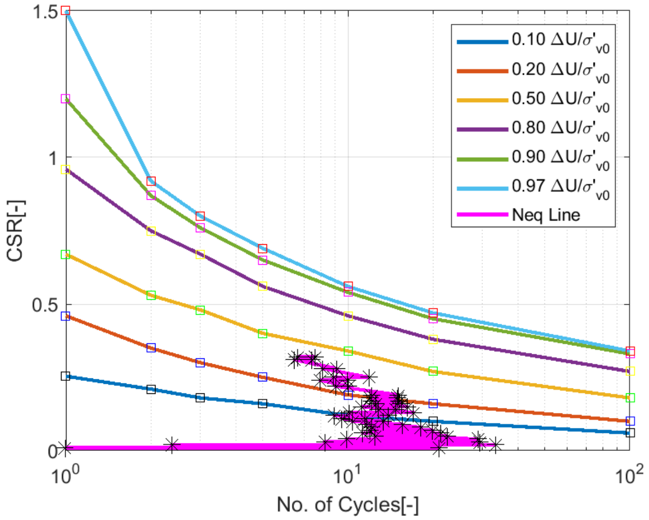

Figure 4.10: Contour diagram with EPPR Accumulation Line, Depth 2.46m

vided. The known depths and the EPPR calculated from the developed code are listed in Table 4.3.

Table 4.3: Comparison of EPPR Values

Depth (m)	EPPR from Report	EPPR Calculated	Relative Error (%)
2.35	0.3	0.4	33.33
5.9	0.95	0.98	3.16
6.5	0.62	0.82	32.26
7.3	0.99	0.98	1.01
17.7	0.73	0.82	12.33
31.05	0.37	0.65	75.68

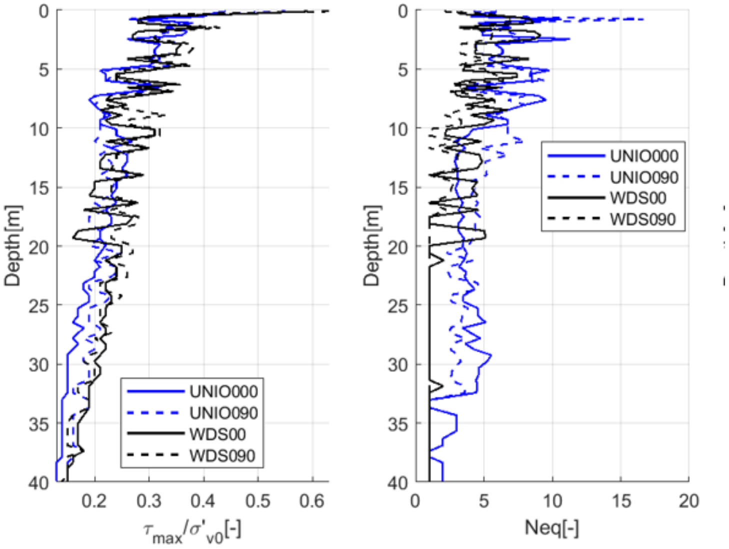

(a) τ_{max}/σ'_{v0} and N_{eq}

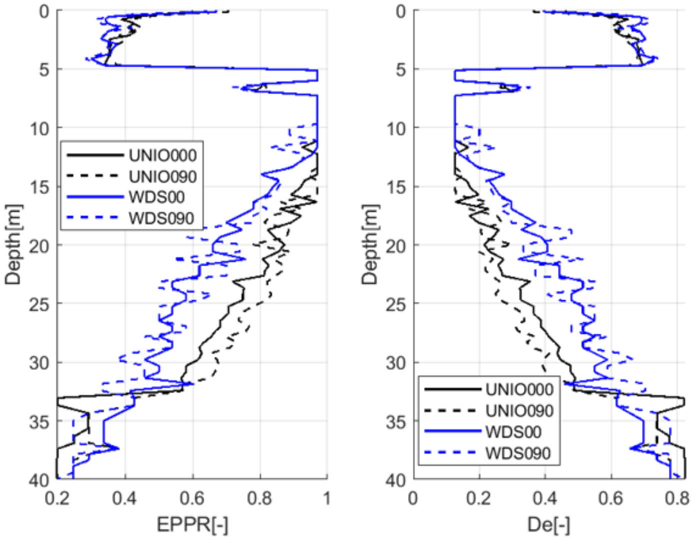

(b) $EPPR$, and Degradation Factor D_e

Figure 4.11: Plate with τ_{max}/σ'_{v0}, N_{eq}, $EPPR$, and Degradation Factor D_e

4.2.5 Comparing the CDF with Safety Factor Based Methods

To fully assess the performance of the CDF, its results are compared with those obtained from the traditional SF-based methods. This comparison focuses on key metrics such as the SF, EPPR, and the degradation factors applied to ultimate soil strength.

To facilitate a comparative analysis, CPT test data, from the same location where the CDF was applied, were used to assess liquefaction potential using the Idriss & Boulanger [8] method following the methodology outlined in Section 3.2.

Figure 4.12 illustrates the SF results alongside the corresponding EPPRs predicted by the CDF.

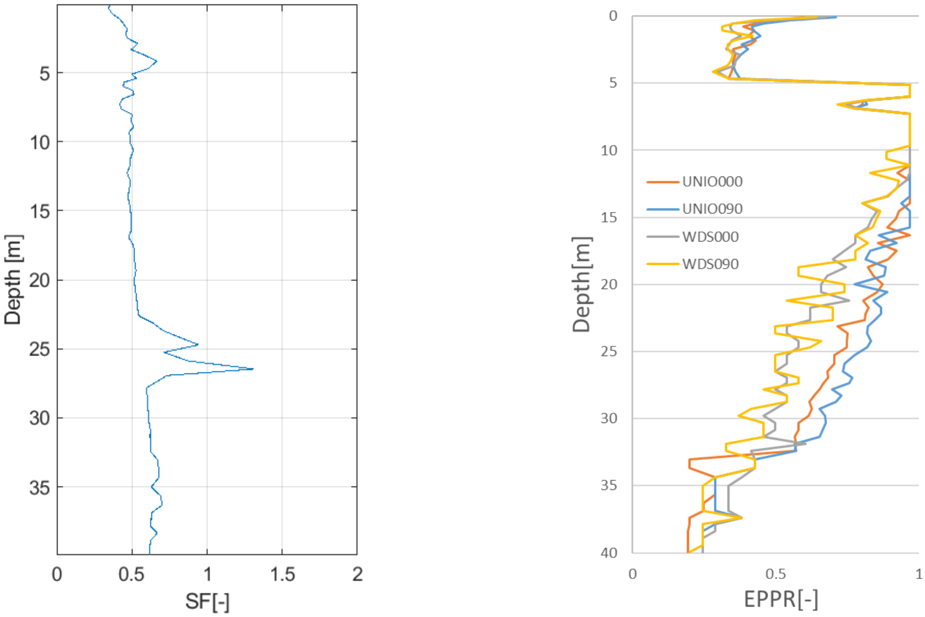

(a) Safety Factor - Idriss and Boulanger (2014) [8]

(b) Predicted EPPR

Figure 4.12: Comparison of Safety Factor and Predicted EPPR

Additionally, Figure 4.13 presents a comparison of the degradation factors by depth as determined following the guidelines by the Japanese Road Association [27] (red line), and by Boulanger [9] (blue lines).

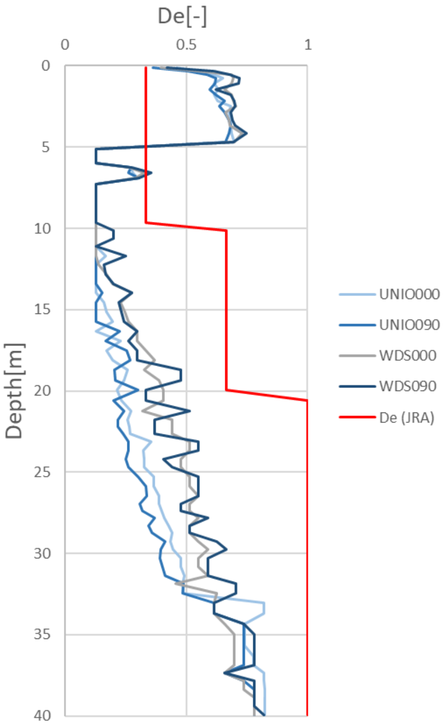

Figure 4.13: Comparison of Degradation Factors from JRA and Boulanger

The comparison between the SF and the predicted EPPR reveals that the SF method suggests that the entire soil column is susceptible to liquefaction. In contrast, the CDF indicates that complete liquefaction is confined to depths between 5 and 15 meters, with the rest of the soil column exhibiting low to moderate EPPR.

Regarding the degradation factors, the discrepancies in liquefaction prediction lead to differences in the resulting factors. The Japanese Road Association's approach is more conservative for shallow depths, while at greater depths, the degradation factor approaches or equals 1. Conversely, Boulanger's method, which is aligned with the predicted EPPR, is less conservative in the top 5 meters of the soil column. However, at greater depths, the degradation factor is lower than that proposed by the Japanese Road Association.

Chapter 5

Validation of the CDF's Ability to Predict EPPR

In this chapter, the results of the CDF for sands with relative densities (DR) of 55% and 75% will be compared to the results of a FEM model to validate the CDFs ability to predict EPPR accumulation. To minimize modeling discrepancies between the software used for all analyses, a simplified soil column will be assessed for this validation experiment. The validation strategy is outlined in the following steps:

- EPPR contour plots are generated using the PLAXIS 2D soil testing facility with Stress-Controlled CDSS Tests.
- Undrained SRA is conducted in PLAXIS 2D to calculate the EPPR using the same motion, scaled by Earthquake Scaling Factors of 0.25, 0.5, 1, and 2.
- Drained SRA is conducted in PLAXIS 2D with $\nu = 0.495$ and in DEEPSOIL v7.0, followed by the extraction of CSR time history at selected stress points.
- The CDF is applied to the extracted CSR time history.
- The EPPR is compared based on the maximum recorded values.

5.1 PLAXIS 2D Model

The soil column under investigation is 41 meters long and consists of two clay layers modeled as linearly elastic, as detailed in Tables 5.1 and 5.2 and an elastic bedrock, as shown in Tables 5.3 and 5.4. The first clay layer is 7 meters thick, the last clay layer is 31 meters thick, and the bedrock is 2 meters thick. The sand layer is 2 meters long, and its properties are presented in Sections 5.3 and 5.4. The Rayleigh damping coefficients are calculated based on the fundamental eigenfrequency and five times the fundamental eigenfrequency of the soil column, as determined using DEEPSOIL V7.0.

The input motion, in all cases, is a baseline-corrected, spectral-matched motion from the Loma Prieta earthquake, as described in Section 4.2.1 and found in Appendix B. This motion is scaled by acceleration multipliers/earthquake scaling factors (E.S.F.) of 0.25, 0.5, 1, and 2 to simulate motions of different amplitudes.

Dynamic Plane Strain analysis is conducted in PLAXIS 2D without consolidation for 1000 solution steps, using automatic sub-step determination to ensure proper wave propagation through the 15-noded elements as shown in Table 5.5. Static boundary conditions are set to fixed at the bottom and free everywhere else. Dynamic boundary conditions are set to tied degrees of freedom on the sides, free on the top, and the bottom is modeled as a compliant base. All sides of the soil column are impermeable, restricting the flow of water. Boundary conditions are summarized in Table 5.6.

Table 5.1: Material Properties for the Clay Layers

Material set		
Identification		Clay
Soil model		Linear Elastic
Drainage type		Undrained C
Unit weights		
γ_{sat}	kN/m^3	21.00
Rayleigh damping		
Input method		SDOF equivalent
Rayleigh α		0.1100
Rayleigh β		0.5045E-3
ξ_1	%	1.000
ξ_2	%	1.000
f_1	Hz	1.050(55%) or 1.060(75%)
f_2	Hz	5.260(55%) or 5.30(75%)

Table 5.2: Mechanical Properties for the Clay Layers

Stiffness		
$E_{u,\text{ref}}$	kN/m^2	180.7E3
ν_u (nu)		0.4950
Alternatives		
G_{ref}	kN/m^2	60.42E3
E_{oed}	kN/m^2	6.102E6
Wave velocities		
V_s	m/s	168.0
V_p	m/s	1688

Table 5.3: Material Properties for Bedrock

Material set		
Identification		Bedrock
Soil model		Linear Elastic
Drainage type		Drained
Unit weights		
γ_{sat}	kN/m^3	22.00
Rayleigh damping		
Input method		Direct
Rayleigh α		0.000
Rayleigh β		0.000

Table 5.4: Mechanical Properties for Bedrock

Stiffness		
E_{ref}	kN/m^2	151.9E3
ν (nu)		0.2000
Alternatives		
G_{ref}	kN/m^2	63.30E3
E_{oed}	kN/m^2	168.8E3
Wave velocities		
V_s	m/s	168.0
V_p	m/s	274.3
Excess pore pressure calculation		
Determination		ν-undrained definition
ν_u definition method		Direct
ν_u, equivalent (nu)		0.4950

Table 5.5: PLAXIS 2D Mesh Details

Mesh Parameter	**Value**
Nr. of soil elements	220
Nr. of nodes	1994
Average element size	0.9371 m
Maximum element size	1.767 m
Minimum element size	0.2857 m

Table 5.6: Boundary Conditions

Boundary Condition Type	**Boundary**	**Condition**
Static	Xmin, Xmax, Ymax	Free
Static	Ymin	Fixed
Dynamic	Xmin, Xmax	Tied Degrees of Freedom
Dynamic	Ymin	Compliant Base
Groundwater	Xmin, Xmax, Ymin, Ymax	Impermeable

5.2 DEEPSOIL V7.0 Model

For the first total stress analysis, a model was set up in DEEPSOIL v7.0 [25]. The goal was to simulate the behavior of the PLAXIS model as closely as possible. The analysis settings are detailed in Table 5.7. The top and bottom clay layers are modeled as linear elastic. The bedrock is modeled as elastic, with a shear wave velocity (V_s) of 168 m/s and a unit weight of 22 kN/m^3. The sand layer is modeled using the General Quadratic Hyperbolic (GQH) [19] soil model, with settings provided in Tables 5.8, 5.9. The shear strength was determined using the critical state friction angle specified in the PLAXIS 2D models, as detailed in Tables 5.13 and 5.15 , and calculated using the formula outlined in Section 3.1. The Vs was derived by computing the small strain shear modulus of the sands through the PLAXIS 2D soil testing facility.

The initial soil column, before further discretization to ensure accurate shear wave propagation, is depicted in Figure 4.4. The input motion's maximum frequency content is set to 50 Hz which will be used for the discretization, ensuring the soil model's response is appropriately captured for the specified seismic conditions.

The input motion is the same baseline-corrected, spectral-matched Loma Prieta earthquake, scaled by factors of 0.25, 0.5, 1, and 2 to simulate motions of different amplitudes.

Damping is set to Rayleigh damping, as specified in Table 5.10. The Rayleigh damping matrix is defined using the eigenfrequency of the soil column and five times the eigenfrequency, ensuring that the damping accurately reflects the dynamic characteristics of the soil structure across a broad frequency range. The analysis control parameters are defined in Table 5.7.

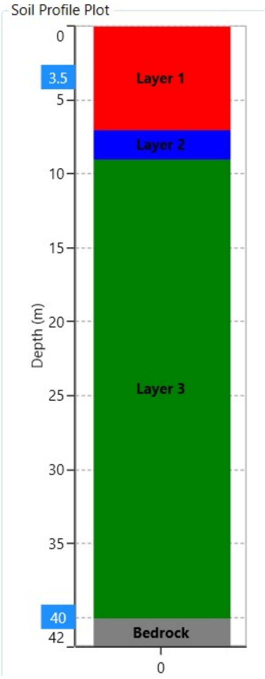

Figure 5.1: DEEPSOIL v7.0 Soil Column

Table 5.7: Analysis Type Settings - DEEPSOIL v7.0

Analysis Type Definition	
Analysis Method	Nonlinear
Generate Excess Porewater Pressure	No
Enable Dissipation	No
Make Top of Profile Permeable	No
Make Bottom of Profile Permeable	No
Solution Type	Time Domain
Default Soil Model	General Quadratic/Hyperbolic Model (GQ/H)
Default Hysteretic Re/Unloading Formulation	Non-Masing Re/Unloading
Maximum Frequency	50Hz

Table 5.8: Mean Layer Properties

Sand Layer Properties	
Thickness (m)	2
Unit Weight (kN/m^3)	18
Shear Wave Velocity (m/s)	
Constant Value	173(55%) or 203.00(75%)
Shear Strength (kPa) Varying with Depth	
Depth[m]	Shear Strength
7	95(55%) or 112(75%)
9	106(55%) or 125(75%)

Table 5.9: Layer Reference Curves

Layer Reference Curve	
Reference Curve	Darendeli, 2001
Parameter	**Value**
OCR	1
Ko	0.5
N	10
Frequency	1
PI	0

Table 5.10: Rayleigh Damping Settings - DEEPSOIL V7.0

Rayleigh Damping	
Define matrix with	Frequencies
1 Mode/Freq.	1.05(Dr=55%) or 1.06(Dr=75%)
2 Modes/Freq.	5.26(Dr=55%) or 5.30(Dr=75%)

Table 5.11: Frequency Domain and Time Domain Settings

Number of iterations	15
Effective Shear Strain Definition SSR	$\frac{M-1}{10}$
Effective Shear Strain Ratio (SSR)	0.65
Complex Shear Modulus Formulation	Frequency Independent $G^{*} = G(1 + 2i\xi)$
Step Control	Flexible
Maximum Strain Increment (%)	0.001
Integration Scheme	Implicit: Newmark Beta Method $(\beta = 0.25, \gamma = 0.5)$
Time-history Interpolation Method	Linear in time domain

5.3 Validation of Sand with 55% Relative Density

In this section, the CDF is applied to a case where sand with a relative density of 55% is used. A sand material with properties detailed in Tables 5.12, 5.13 is defined using the PM4Sand soil constitutive model. The soil properties used in this validation experiment are based on those provided by Vilhar [38], ensuring they correspond to realistic material characteristics.

As a first step, the contour plots must be generated using the PLAXIS 2D soil testing facility. For the defined sand material, stress-controlled CDSS tests are conducted to construct the different EPPR contour lines. For this purpose, consolidation is set to $K_0 = 0.5$, and effective vertical stress is set conservatively at 100 kPa as the effective vertical stress of the sand layer ranges between 77 and 93kPa and higher effective vertical stress corresponds to lower CRR. The constructed graph is shown in Figure 5.2 where EPPR denotes $\frac{dU}{\sigma'_{v0}}$.

Table 5.12: Material Properties - Sands of 55% and 75% Relative Density.

Material set		
Drainage type		Undrained A
Unit weights		
γ_{sat}	kN/m^3	18.00
Rayleigh damping		
Input method		SDOF equivalent
Rayleigh α		0.1100
Rayleigh β		0.5045E-3
ξ_1	%	1.000
ξ_2	%	1.000
f_1	Hz	1.050(55%) or 1.060(75%)
f_2	Hz	5.260(55%) or 5.30(75%)

Once the contour graph is ready, an undrained SRA is conducted in PLAXIS 2D, and the maximum EPPR is recorded. Total-stress SRA is then conducted in both DEEPSOIL and PLAXIS 2D.

To achieve this in PLAXIS 2D, the analysis type for the sand layer is set to drained, and the Poisson's ratio (ν) is set to 0.495 to simulate the incompressibility of water. The stress time history for stress points 589 and 459, which correspond to the top

Table 5.13: Mechanical Properties - Sand of 55% Relative Density.

User-defined parameters		
DR0		0.5500
G0		677.0
hp0		0.4000
pA	kN/m^2	101.3
emax		0.8000
emin		0.5000
nb		0.5000
nd		0.1000
ϕ_{cv}	°	33.00
nu		0.3000
Q		10.00
R		1.500
PostShake		0.000
Excess pore pressure calculation		
Determination		ν-undrained definition
ν_u, equivalent (nu)		0.4950

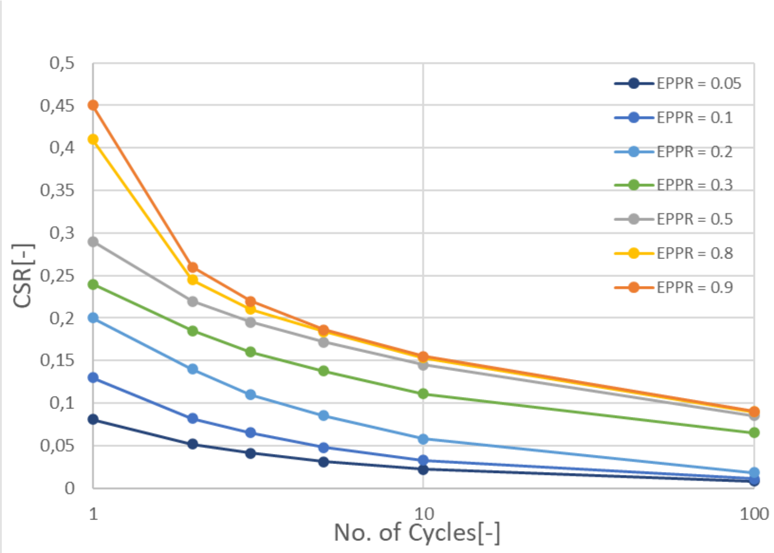

Figure 5.2: Contour Diagram for Sand of 55% Relative Density

and bottom of the sand layer, as can be seen in Figure 5.3, are recorded and normalized with the respective effective vertical stress, to obtain the CSR time history as defined in Section 3.3.2.

The CSR time histories, along with the constructed contour diagram, are given as input to the CDF to predict the EPPR. These results are then recorded and compared to the results from the FE model in terms of maximum recorded values. The comparison of these results can be found in Table 5.14.

Table 5.14: Validation Error for Sand of 55% Relative Density

Method Used	**Cycle Counting Method**	**E.S.F. = 1**	**Rel. Error**	**E.S.F. = 0.5**	**Rel. Error**	**E.S.F. = 0.25**	**Rel. Error**	**E.S.F. = 2**	**Rel. Error**
Plaxis (Reference)	-	0.97	0%	0.2956	0%	0.221	0%	0.97	0%
Contour Method	Rainflow C.	0.97	0%	0.495	67%	0.224	1%	0.97	0%
Contour Method	Range Pair C.	0.97	0%	0.423	43%	0.218	-1%	0.97	0%
Plaxis Contour	Rainflow C.	0.97	0%	0.4	35%	0.209	-5%	0.97	0%
Plaxis Contour	Range Pair C.	0.97	0%	0.38	29%	0.212	-4%	0.97	0%

PLAXIS 2D serves as the reference case, while the Contour Method involves conducting a total stress analysis using DEEPSOIL v7.0 followed by the application of the

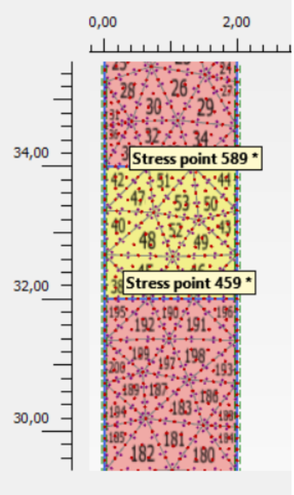

Figure 5.3: Mesh and Stress Points Selected

CDF. Plaxis/Contour represents in similar manner a total stress analysis conducted in PLAXIS 2D, followed by the application of the CDF.

As observed, the CDF accurately predicts the EPPR for most motion amplitudes. However, for the case where the motion is multiplied by 0.5x, a larger error is noted.

When total stress SRA is conducted through PLAXIS 2D, the difference is primarily attributed to the different assumptions made during the procedure, which will be explained in Chapter 5.5.

5.4 Validation of Sand with 75% Relative Density

This section continues the validation process by applying the CDF to a denser sand material with a relative density of 75% to examine how the CDF performs for a sand layer with higher cyclic resistance. The material is again defined using the PM4Sand constitutive model, with properties detailed in Tables 5.12, 5.15. The soil properties used are again based on those provided by Vilhar [38].

Following the procedure described in Section 5.3, the contour plot for the denser sand material is generated (Figure 5.4 where EPPR denotes $\frac{dU}{\sigma'_{v0}}$).

Subsequently, total-stress SRA is conducted in both DEEPSOIL v7.0 and PLAXIS 2D. The results and the respective relative error are presented in Table 5.16.

Table 5.15: Mechanical Properties - Sand of 75% Relative Density.

User-defined parameters		
DR0		0.7500
G0		890.0
hp0		0.6300
pA	kN/m^2	101.3
emax		0.8000
emin		0.5000
nb		0.5000
nd		0.1000
ϕ_{cv}	°	33.00
nu		0.3000
Q		10.00
R		1.500
PostShake		0.000
Excess pore pressure calculation		
Determination		ν-undrained definition
ν_u, equivalent (nu)		0.4950

Table 5.16: Validation Error for Sand of 75% Relative Density

Method Used	**Cycle Counting Method**	**E.S.F. = 1**	**Rel. Error**	**E.S.F. = 0.5**	**Rel. Error**	**E.S.F. = 0.25**	**Rel. Error**	**E.S.F. = 2**	**Rel. Error**
Plaxis(Reference)	-	0.28	0%	0.25	0%	0.2	0%	0.97	0%
Contour Method	Rainflow C.	0.44	57%	0.254	2%	0.196	1%	0.97	0%
Contour Method	Range Pair C.	0.388	37%	0.25	1%	0.187	-4%	0.97	0%
Plaxis / Contour	Rainflow C.	0.39	37%	0.2504	1%	0.174	-11%	0.97	0%
Plaxis / Contour	Range Pair C.	0.318	12%	0.2439	-2%	0.1871	-4%	0.97	0%

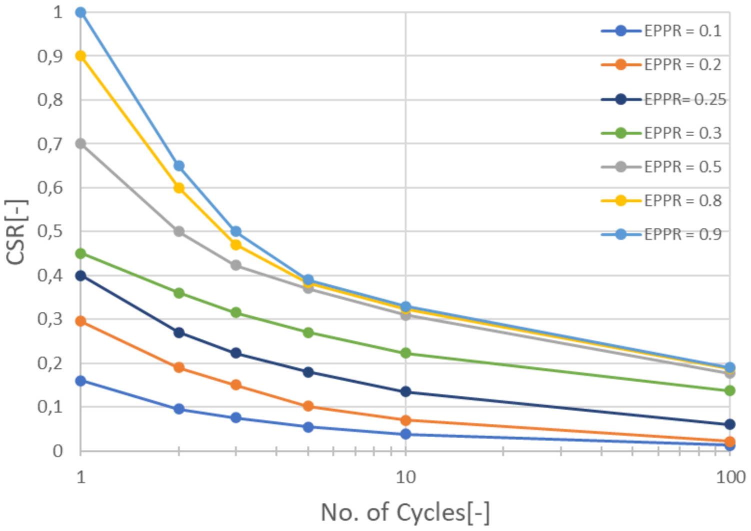

Figure 5.4: Contour Diagram for Sand of 75% Relative Density

Similar to the sand of 55% relative density, it can be observed that for lower EPPR ranges and for the onset of liquefaction, the CDF performs well. However, larger errors are noted in the 0.3-0.5 EPPR range.

5.5 Error Analysis

Understanding the sources of error in the CDF is essential for assessing its EPPR predictive accuracy. This section focuses on identifying the key factors that contribute to discrepancies between the results produced by the CDF and those from the FEM model.

Several sources of error were identified, including conservative assumptions during the creation of the contour graphs, such as overburden stress, the choice of damping curves, and the use of different baseline correction algorithms. Additionally, cycle counting methods, construction of the contour diagrams, and assumptions related to the soil's internal friction angle all influence the predicted EPPR. By analyzing these factors, this section aims to provide a comprehensive understanding of why the errors occur and how they affect the accuracy and conservatism of the CDF.

5.5.1 Conservatism when Creating the EPPR Contour Graph

Firstly, the contour diagram is constructed based on an initial overburden effective stress of 100 kPa while the maximum exhibited in the sand layer is 93kPa . This introduces error, as the CRR of the soil increases with a decrease in overburden effective stress. To mitigate this effect in this validation study, the sand layer was kept relatively short. Additionally, the construction method of the EPPR contour diagrams also affects the results. It is assumed that the different points, usually between six and eight for each EPPR contour line, are connected linearly to create the full graph, with the points in between resulting from linear interpolation.

5.5.2 Comparison in Terms of Maximum Values

Comparisons were made in terms of maximum pore pressure ratio. In instances with higher error values, part of the layer reached this maximum value, while the rest exhibited EPPRs are closer to those observed in the FEM model. This suggests that when examining different stress points or different parts of the refined soil layer, there is variation in the results, likely due to resonating or mitigating effects occurring during wave propagation. This phenomena can be clearly observed in the first case study results as exhibited in Figure 6.4.

5.5.3 Damping and Shear Modulus Degradation Curves

Furthermore, the monotonic damping curves used for total stress analysis do not account for the cycle-by-cycle softening of the soil material due to pore pressure accumulation. This is evident in Figures 5.5 and 5.6 where differences in damping and shear modulus degradation curves are observed. These plots are generated by performing undrained and drained CDSS tests, where the current shear modulus is calculated as the secant modulus at the point of maximum stress, and the damping ratio is determined from the area of the final hysteretic loop.

To assess the differences in stress behavior between the two cases, the time series of stresses were plotted for both relative densities, as shown in Figures 5.7 and 5.8. From these plots, only minor differences in the stress time histories can be observed between the two cases.

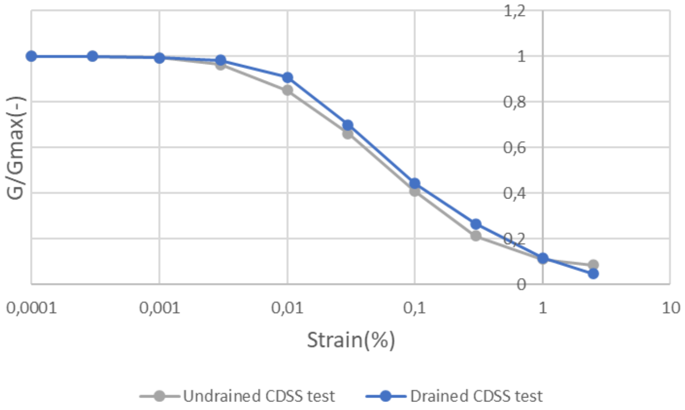

Figure 5.5: Comparison Between Shear Modulus Degradation Curves - Sand of Dr = 55%

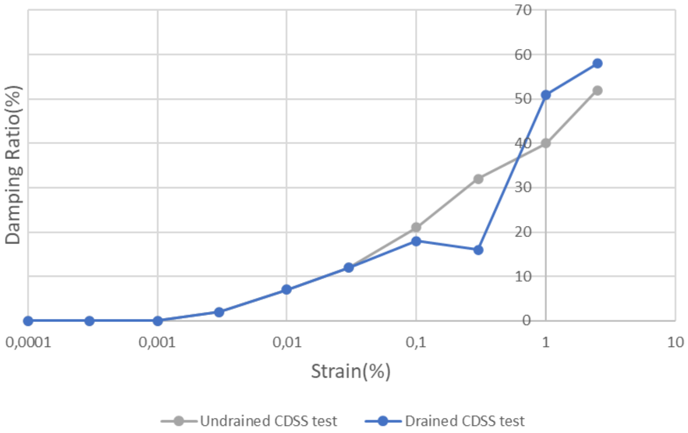

Figure 5.6: Comparison Between Damping Curves - Sand of Dr =55%

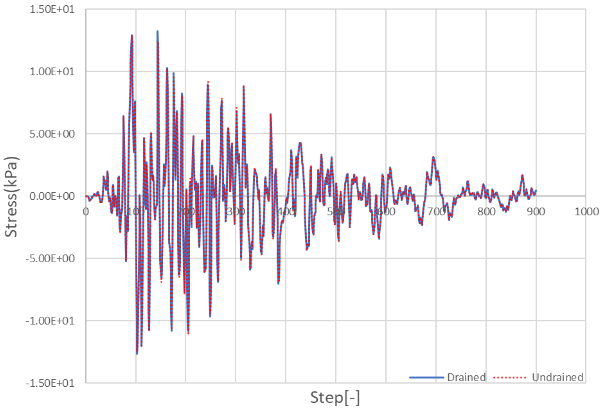

Figure 5.7: Stress Time Series for Relative Density - Dr55%

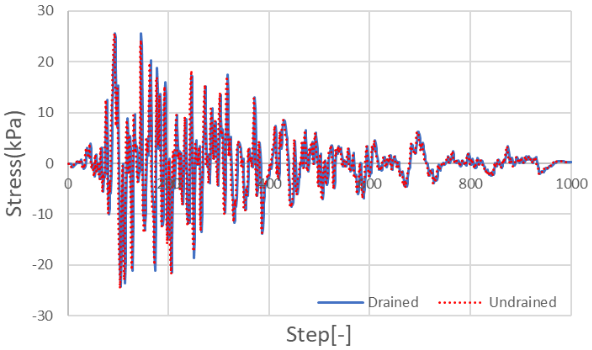

Figure 5.8: Stress Time Series for Relative Density - Dr75%

In order to gain a deeper understanding of these differences, the stress data were further analyzed by segmenting them into discrete bins. This approach allows for a more detailed comparison of the stress distribution over the entire signal. To achieve this, RPC was employed, as it demonstrated the highest accuracy during the validation process. The resulting stress bin comparisons for the two relative densities are shown in Figures 5.9 and 5.10. From the graphs it can be observed that the total stress ”drained” analysis exhibits slightly higher or slightly more high stress cycles in comparison to the ”undrained” analysis which takes into account EPP accumulation.

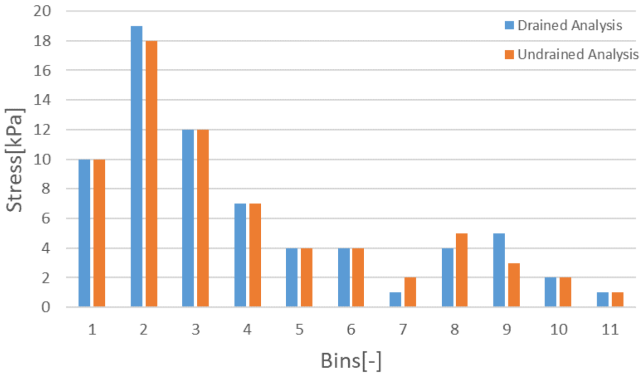

Figure 5.9: Stress Bins Comparison for Relative Density - Dr55%

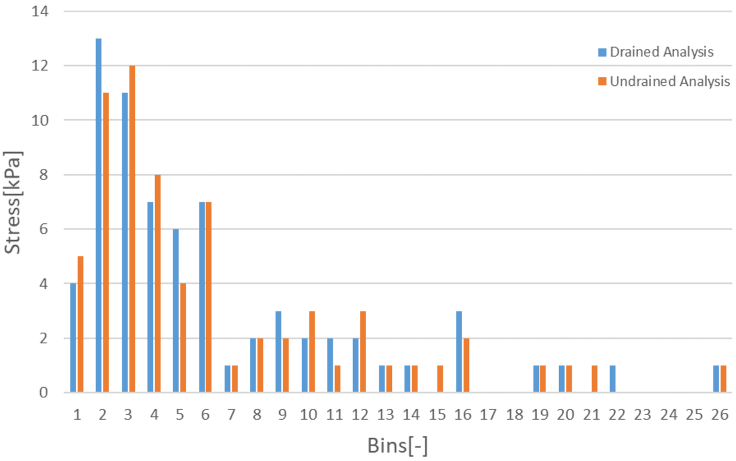

Figure 5.10: Stress Bins Comparison for Relative Density - Dr75%

5.5.4 Cycle Counting Methods

The results also indicate that the cycle counting method impacts the outcomes, introducing error. Among the two cycle counting methods examined, RPC performs better than RFC. This stems from the inherent differences between the methods. In seismic loading, stress cycles are often irregular, with varying amplitudes and frequencies. RFC was originally developed for fatigue analysis, where load cycles tend to be more regular, such as in material fatigue studies. RFC works well for decomposing stress histories into half-cycles but tends to prioritize larger cycles and often identifies cycles around different average shear stress values (τ_{average}). These cycles are less critical for liquefaction but are included conservatively because the contour diagrams are generated with the assumption that $\tau_{\text{average}} = 0$, leading to an overestimation of the effects. Additionally, RFC tends to detect more cycles than RPC, as it captures smaller, less significant cycles that RPC typically filters out.

In contrast, RPC captures only the cycles between two consecutive zero crossings on the y-axis, ignoring smaller cycles that occur above or below zero, while transforming all cycles to be centered around $\tau_{\text{average}} = 0$, aligning more closely with the assumptions used in the contour diagrams. This more accurately reflects the stress conditions relevant to liquefaction. As a result, RFC tends to produce higher CSRs and more cycles than RPC, which leads to higher predicted EPPRs, as shown in Figure 5.11.

5.5.5 Constitutive Model

Moreover, the PM4Sand model is highly accurate in predicting the onset of liquefaction. Nonetheless, minor discrepancies are observed compared to experimental results, particularly in the range where the largest errors occur, which depends on other model parameters. As illustrated in Figure 5.12 , these discrepancies are evident when comparing the different lines to the experimental data. To fully evaluate the performance of the CDF in these ranges, it would be ideal to compare the values with shake table tests, although this is beyond the scope of this thesis.

5.5.6 Assumptions for Soil Properties

Another factor to consider is the angle of internal friction when comparing DEEPSOIL and PLAXIS 2D results. In the PM4Sand model, the critical state friction angle is explicitly defined. For the DEEPSOIL model, the same angle was used to define the shear strength of the coarse-grained material. This approach is inherently conservative because the critical state friction angle is only relevant when the soil material

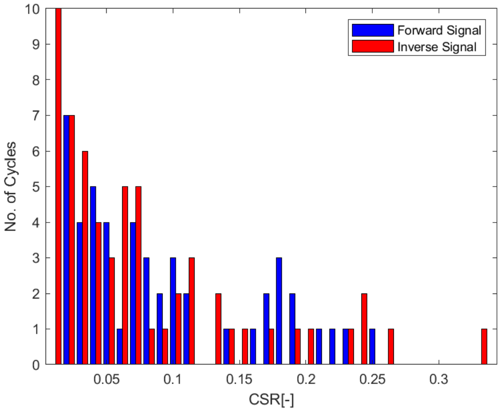

(a) Cyclic Stress Ratio Histogram - Range Pair Counting

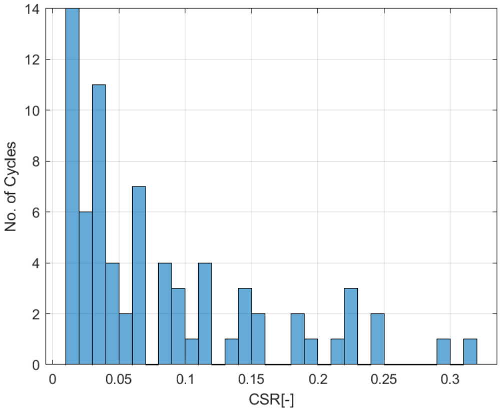

(b) Cyclic Stress Ratio Histogram - Rainflow Counting

Figure 5.11: Cyclic Stress Ratio Histograms for Stress Point of Maximum Error - Relative Density of 75%

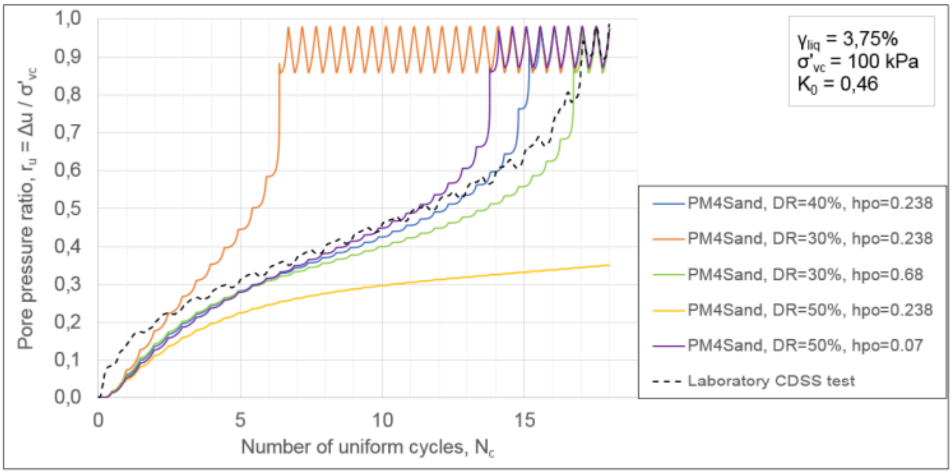

Figure 5.12: Generation of EPP, PM4Sand Model Response Versus Cyclic Laboratory Data. Source: [37]

reaches the critical state. Prior to reaching this state, the friction angle is typically 3-4 degrees higher. This conservative assumption leads to a lower calculated shear strength and consequently higher shear stress ratios.

5.5.7 Baseline Correction Algorithms

Moreover, both PLAXIS 2D and DEEPSOIL V7.0 utilize distinct baseline correction algorithms. Consequently, during the input motion correction process, there may be discrepancies in the content of the input data when comparing results of PLAXIS 2D and DEEPSOIL v7.0. This could be prevented by using a baseline correction software like SeismoSignal but the academic version does not allow for baseline correction.

5.5.8 Overall Validation Conclusion

Overall, the final validation results demonstrate that the CDF reliably predicts the EPPR for the onset of liquefaction, irrespective of the software used for the total stress analysis. The errors are minimal for lower EPPRs. However, in the mid-range of EPPR, higher error values are observed. These fluctuations in EPPR are caused by differences in analysis type, constitutive model, cycle counting methods, and assumptions made when applying the CDF. This makes the method slightly more conservative.

Chapter 6

Case Studies

In this chapter, the CDF is applied to two distinct case studies to demonstrate its effectiveness in real-world and hypothetical scenarios. The first case study focuses on Akita Port, Japan, which experienced severe damage during the 1983 Nihonkai-Chubu Earthquake. This site provides a well-documented example of earthquake-induced liquefaction, making it an ideal candidate for validating the CDF's predictive capabilities. The study allows for a direct comparison between the predicted EPPR and the actual damage observed, offering critical insights into the framework's accuracy. The second case study focuses on an offshore wind farm under development in the Netherlands, using available soil data from the North Sea, combined with the seismic profile of a highly active seismic region. Although the Netherlands is not a seismically active area, this theoretical scenario allows for a detailed exploration of how liquefaction could affect the design of MP foundations for OWTs. By applying the seismic conditions of a more earthquake-prone region, this case study examines how soil degradation due to liquefaction might influence foundation strategies and the structural integrity of the wind turbines, offering critical insights into the potential risks and design adjustments necessary in similar offshore environments.

6.1 Akita Port

This case study is based on research conducted by P.V. Toloza (2018)[37] on Akita Port, Japan, which suffered extensive damage during the 1983 Nihonkai-Chubu Earthquake. The earthquake-induced liquefaction led to significant deformations and settlement of the port structures, making it an ideal site for applying and validating the CDF. Toloza's study involved analyzing soil data from two wharfs at the port—Omaha Wharf No.1, which remained intact, and Omaha Wharf No.2, which was severely damaged.

In this section, SRA is conducted using derived soil data from the port, and the CDF is applied to predict the EPPR. Since the original seismic motion data from the earthquake was unavailable, a spectral-matched and baseline-corrected motion from the 1989 Loma Prieta Earthquake is used, as it closely matches the magnitude and PGA of the original event. The motion can be found in Appendix B.

By comparing the predicted EPPR from the CDF with field data and FEM results, this case study aims to validate the accuracy of the CDF in predicting liquefaction risk in a real-world scenario. The outcomes will highlight the method's reliability and any potential limitations when applied to complex, historical earthquake events.

6.1.1 Quay Wall Structure Omaha Wharf No.1

Omaha Wharf No.1 is notable for remaining undamaged during the 1983 Nihonkai-Chubu Earthquake, despite being similar and subjected to similar seismic conditions as Omaha Wharf No.2, which sustained significant damage. This section focuses on understanding why Omaha Wharf No.1 withstood the earthquake and assessing the accuracy of the CDF in predicting its liquefaction risk.

The soil stratigraphy for Omaha Wharf No.1 is presented in Table 6.1. The column consists of a mixture of clean sand (S), very silty sand (VSS), slightly silty sand (SSS), and very sandy clay (VSC). The relative densities of these layers range from medium dense (MD) to very dense (VD), with a high CRR generally associated with the dense sand layers. These properties suggest a lower susceptibility to liquefaction, which correlates with the lack of observed damage.

Table 6.1: Soil Stratigraphy - Omaha Wharf No.1

Layer	Depth Range [m]	Description	Density	$(N_1)_{60}$	D_R [%]	ϕ' [°]	γ_{unsat} [kN/m^3]	γ_{sat} [kN/m^3]	c [kPa]
1	0 to -7	S	MD	30	70	37	18	20	0
2	-7 to -8.5	VSS	MD	25	65	36	19	21	0
3	-8.5 to -13	SSS	MD	25	70	37	19	21	0
4	-13 to -20.5	SSS	VD	35	80	38	18	20	0
5	-20.5 to -21.6	VSC	VS	17	-	27	18	20	5
6	-21.6 to -30	SSS	MD	25	70	37	19	21	0

Initially, the simplified liquefaction assessment method was applied, adjusting the inputs to account for minor differences in the intensity and magnitude between the spectral-matched Loma Prieta earthquake motion and the original Nihonkai-Chubu motion. As illustrated in Figure 6.1, the SF indicates that the soil column does not appear to be prone to liquefaction based on Section 3.2.

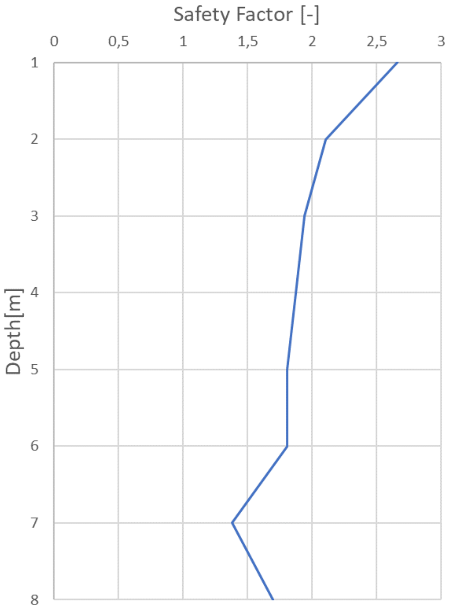

Figure 6.1: Simplified Method - Omaha Wharf No.1

To model the soil column in PLAXIS 2D, all layers were simulated using the Hardening Soil Small constitutive model [31] to establish the initial conditions. The parameters, selected based on Brinkgreve et al. [11], are listed in Table 6.2.

Table 6.2: Parameter Selection - Hardening Soil Small Model - Omaha Wharf No.1

Layer	Depth [m]	$E_{50,\mathrm{ref}}$ [MPa]	$E_{\mathrm{oed,ref}}$ [MPa]	$E_{\mathrm{ur,ref}}$ [MPa]	m [-]	$K_{0,\mathrm{nc}}$ [-]	R_f [-]	$G_{0,\mathrm{ref}}$ [MPa]	$\gamma_{0.7}$ [-]
1	4.25	42	42	84	0.481	0.402	0.91	107.6	1.3×10^{-4}
2	7.8	39	39	78	0.497	0.410	0.92	104.2	1.35×10^{-4}
3	10.5	42	42	84	0.481	0.402	0.91	107.6	1.3×10^{-4}
4	17	48	48	96	0.450	0.384	0.90	114.4	1.2×10^{-4}
5	21	20	20	40	0.550	0.546	0.92	75	1.65×10^{-4}
6	24.5	42	42	84	0.481	0.402	0.91	107.6	1.3×10^{-4}

Bedrock characteristics were chosen as indicated in Tables 6.3 and 6.4, as the actual bedrock data was not specified.

For the dynamic analysis, the first two layers were replaced with sand layers

Table 6.3: General Properties - Bedrock

Property	Unit	Value
Soil model		Linear Elastic
Drainage type		Non-porous
Unit weights		
γ_{sat}	kN/m^3	24.00

Table 6.4: Mechanical Properties - Bedrock

Stiffness		
E_{ref}	kN/m^2	257.4E3
ν (nu)		0.2000
Alternatives		
G_{ref}	kN/m^2	107.3E3
E_{oed}	kN/m^2	286.0E3
Wave velocities		
V_s	m/s	209.4
V_p	m/s	341.9

modeled using the PM4Sand constitutive model, with parameters shown in Table 6.5. This approach is commonly used when employing the PM4Sand model, as it is specifically optimized for dynamic analysis. For that reason, it is recommended to use a different soil model to establish the initial conditions before switching to PM4Sand for the dynamic phase, ensuring more accurate and reliable results.

Table 6.5: Set of Parameters - PM4Sand Model - Upper Soil Layers

Wharf	D_R [%]	G_0 [-]	n^b [-]	h_{po} [-]
Ohama No.1	70	599	0.2	0.85
	65	980	0.2	2.7

Rayleigh damping parameters used for the analysis are detailed in Table 6.6.

The SRA boundary conditions were consistent with those used for the validation in Chapter 5. Figure 6.2 displays the PLAXIS 2D results, indicating a maximum EPPR of 0.39 in the upper layers.

Following the procedure outlined in the validation chapter, contour graphs were created using the PLAXIS 2D soil testing facility. Next, a best-match DeepSoil model was developed to conduct total stress SRA and apply the CDF. Analysis settings are

Table 6.6: Rayleigh Damping Coefficients - Omaha Wharf No.1 - All Layers

Description	Ohama No. 1 Wharf
Target damping ξ [%]	1.25
Frequency target 1 f_1 [Hz]	1.48
Frequency target 2 f_2 [Hz]	3
Rayleigh damping coefficients α_R	0.1556
Rayleigh damping coefficients β_R	8.88E-04

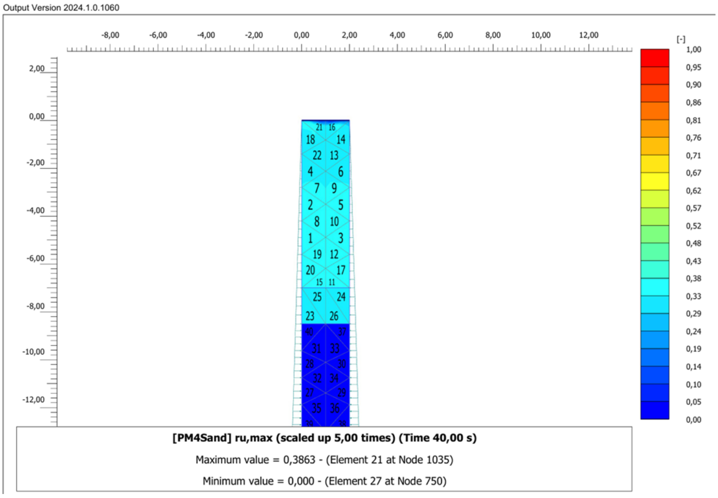

```
[PM4Sand] ru,max (scaled up 5,00 times) (Time 40,00 s)
Maximum value = 0,3863 - (Element 21 at Node 1035)
Minimum value = 0,000 - (Element 27 at Node 750)
```

Figure 6.2: PLAXIS 2D Maximum Excess Pore Pressure Ratio Results - Omaha Wharf No.1

provided in Table 6.7. The difference from the validation lies in the fact that the soil column is primarily modeled using the Hardening Soil Small (HS Small) model, which follows Masing rules. Consequently, Masing rules were also selected in DEEPSOIL v7.0. This modeling choice was made because Masing rules typically result in higher damping compared to non-Masing behavior. This is due to the fact that, when the material is loaded to a certain strain level, the unloading and reloading paths are scaled versions of the initial loading curve. This scaling effect creates more pronounced hysteresis loops, leading to greater energy dissipation with each loading cycle, and consequently, higher damping.

Table 6.7: Analysis Type Settings Omaha Wharf No.1 and 2 - DEEPSOIL v7.0

Analysis Type Definition	
Analysis Method	Nonlinear
Generate Excess Porewater Pressure	No
Enable Dissipation	No
Make Top of Profile Permeable	No
Make Bottom of Profile Permeable	No
Solution Type	Time Domain
Default Soil Model	General Quadratic/Hyperbolic Model
Default Hysteretic Re/Unloading Formulation	Masing Re/Unloading
Maximum Frequency	50Hz

Darendeli shear modulus degradation and damping curves were utilized, with soil properties listed in Table 6.8.

Table 6.8: DEEPSOIL V7.0 Layer Properties - Omaha Wharf No.1

Depth Range (m)	γ (kN/m^3)	G_0 (kPa)	V_s (m/s)	ϕ (-)	S_u Top (kPa)	S_u Bot (kPa)	K_0 (-)
0 to 7	20	107600	229.73	37	86.08	138.83	0.398
7 to 8.5	21	104200	220.63	36	134.22	146.21	0.412
8.5 to 13	21	107600	224.20	37	151.26	188.56	0.398
13 to 20.5	21	114400	231.17	38	197.77	262.23	0.384
20.5 to 21.6	20	75000	191.80	27	176.33	181.94	0.546
21.6 to 30	21	107600	224.20	37	259.02	328.65	0.398

Using the results from DEEPSOIL, the CDF was employed to predict the EPPR for the first two soil layers down to a depth of 8 meters. As illustrated in Figure 6.3 and Figure 6.4 the CDF accurately predicted an EPPR of approximately 0.4-0.5 for the first 8 meters, with maximum error of 22% as detailed in Table 6.9.

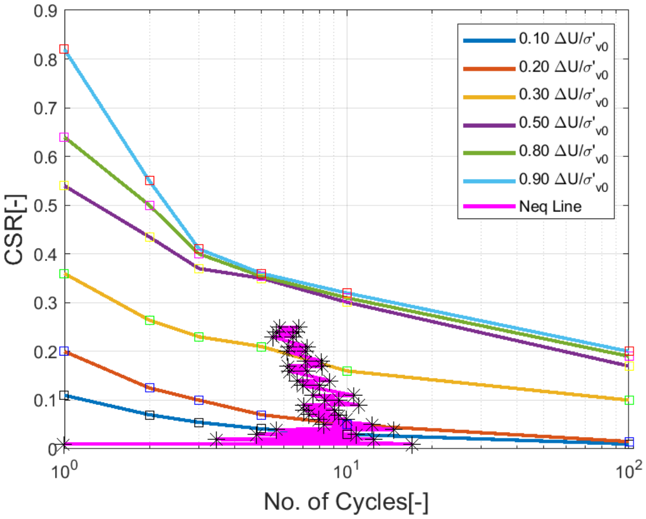

Figure 6.3: Contour Graph - Middle of Second Layer

Table 6.9: Comparison Between RU Max - Omaha Wharf No.1

	Ru_max	Rel. Error
FEM	0.3863	-
Contour Method	0.4978	22%

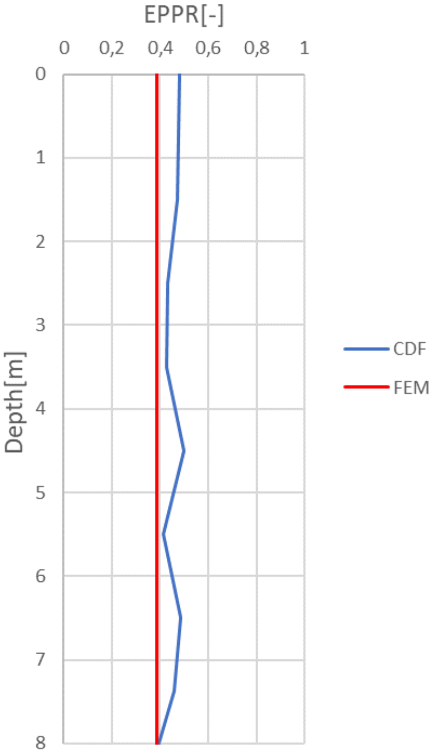

Figure 6.4: Excess Pore Pressure Ratio as Predicted by the CDF - Omaha Wharf No.1

6.1.2 Quay Wall Structure Omaha Wharf No.2

Omaha Wharf No.2 sustained severe damage during the 1983 Nihonkai-Chubu Earthquake, largely due to liquefaction-induced settlement and lateral spreading. This section evaluates the accuracy of the CDF in predicting the EPPR and liquefaction risk for this site.

The soil stratigraphy for Omaha Wharf No.2 is presented in Table 6.10. The soil profile consists of layers of clean backfill sand (CBS), slightly silty sand (SSS), and very sandy clay (VSC), with relative densities ranging from loose (L) to medium dense (MD). These layers, particularly the loose sand, are highly susceptible to liquefaction, which corresponds to the observed damage.

Table 6.10: Soil Stratigraphy - Omaha Wharf No.2

Layer	Depth Range [m]	Description	Density	$(N_1)_{60}$	D_R [%]	ϕ' [°]	γ_{unsat} [kN/m^3]	γ_{sat} [kN/m^3]	c [kPa]
1	0 to -12	CBS	L	8	40	33	17	19	0
2	-12 to -14.5	SSS	L	12	50	34	19	21	0
3	-14.5 to -20	SSS	D	30	75	37	19	21	0
4	-20 to -22.5	VSC	VS	29	-	27	18	20	5
5	-22.5 to -25.5	SSS	MD	22	70	37	19	21	0
6	-25.5 to -30	SSS	D	30	75	37	19	21	0

As with Omaha Wharf No.1, the SF liquefaction assessment method is first applied, adjusting for the differences between the spectral-matched Loma Prieta earthquake motion and the original Nihonkai-Chubu event. The SF method, illustrated in Figure 6.5, shows that the entire soil column is severely prone to liquefaction.

Similarly for this case, all layers were again simulated using the Hardening Soil Small constitutive model to establish the initial conditions. The parameters are listed in Table 6.11.

Table 6.11: Parameter Selection - Hardening Soil Small model - Ohama No.2 Wharf

Layer	Depth [m]	D_R [%]	$E_{50,\text{ref}}$ [MPa]	$E_{\text{oed,ref}}$ [MPa]	$E_{\text{ur,ref}}$ [MPa]	m [-]	$K_{0,\text{nc}}$ [-]	R_f [-]	$G_{0,\text{ref}}$ [MPa]	$\gamma_{0.7}$ [-]
1	5.5	40	24	24	48	0.575	0.455	0.950	87.2	1.6×10^{-4}
2	12.2	50	30	30	60	0.544	0.437	0.938	94	1.5×10^{-4}
3	16	75	45	45	90	0.466	0.393	0.906	111	1.3×10^{-4}
4	20	-	20	20	40	0.550	0.546	0.920	75	1.7×10^{-4}
5	23	70	42	42	84	0.481	0.402	0.913	107.6	1.3×10^{-4}
6	26	75	45	45	90	0.466	0.393	0.906	111	1.3×10^{-4}

The bedrock characteristics were the same as those for Omaha Wharf No.1, as indicated in Tables 6.3 6.4.

For the dynamic analysis, similarly as in Omaha Wharf No.1 the first two layers are replaced with sand layers modeled using the PM4Sand constitutive model, with parameters shown in Table 6.12.

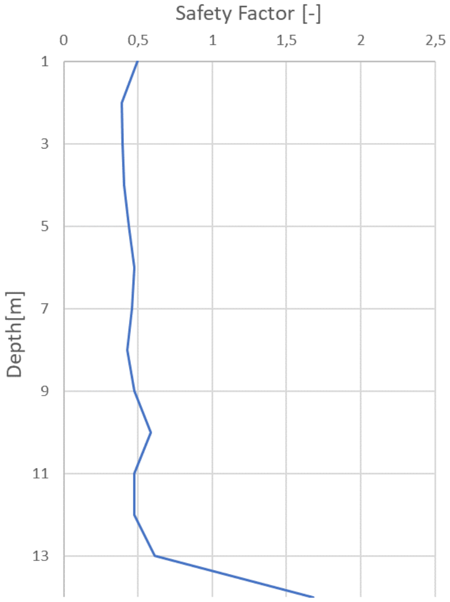

Figure 6.5: Simplified Method - Omaha Wharf No.2

Table 6.12: Set of Parameters Omaha Wharf No.2 - PM4Sand Model - Upper Soil Layers

Wharf	D_R [%]	G_0 [-]	n^b [-]	h_{po} [-]
Ohama No.1	40	530	0.5	0.58
	50	802	0.5	1

Rayleigh damping parameters used for this analysis are detailed in Table 6.13.

Table 6.13: Rayleigh Damping Coefficients - Omaha Wharf No.2 - All Layers

Description	Omaha No. 2 Wharf
Target damping ξ [%]	1.25
Frequency target 1 f_1 [Hz]	1.36
Frequency target 2 f_2 [Hz]	5
Rayleigh damping coefficients α_R	0.1682
Rayleigh damping coefficients β_R	6.25E-04

The SRA boundary conditions and analysis settings are again consistent with those used in the validation Chapter 5. This time, the analysis is run with consolidation as that is the most severe case for layer 2, with permeability coefficients k as shown in Table 6.14.

Table 6.14: Grain Size Distribution and Permeability Coefficient

Layer	Soil Material	$<2\mu$m	2 - 50μm	50μm - 2mm	Permeability Coefficient, k [m/s]
1	Loose sand	0	0	100	1.16E-06
2	Loose sand	0	0	100	1.16E-06
3	Dense sand	10	15	75	3.04E-06
4	Very stiff clay	10	26	64	3.41E-10
5	Medium dense sand	20	52	28	1.94E-07
6	Dense sand	20	52	28	1.94E-07

Figure 6.6 presents the PLAXIS 2D results, showing a maximum EPPR of 1 (indicating full liquefaction) in the upper layer, with the exception of the first few meters at the top of the first and the bottom of the second layer. The first layer does not fully liquefy because the analysis was run with consolidation, allowing for some drainage in the upper portion of the sand layer. Since the CDF does not currently account for dissipation or drainage, it can be reasonably assumed that without drainage, the first layer would indeed fully liquefy.

Repeating the procedure outlined in the validation chapter, contour graphs were created using the PLAXIS 2D soil testing facility. This time, due to significant differences in effective vertical stress in layer 1 and layer 2, multiple contour graphs were created for the same layer to account for the influence of effective vertical stress on the cyclic behavior of the soil. For Omaha Wharf No.2, the same best-match DEEPSOIL model was developed to conduct total stress S.R.A. and apply the CDF. Analysis settings are provided in Table 6.7. The procedure and settings remain consistent with those used for Omaha Wharf No.1.

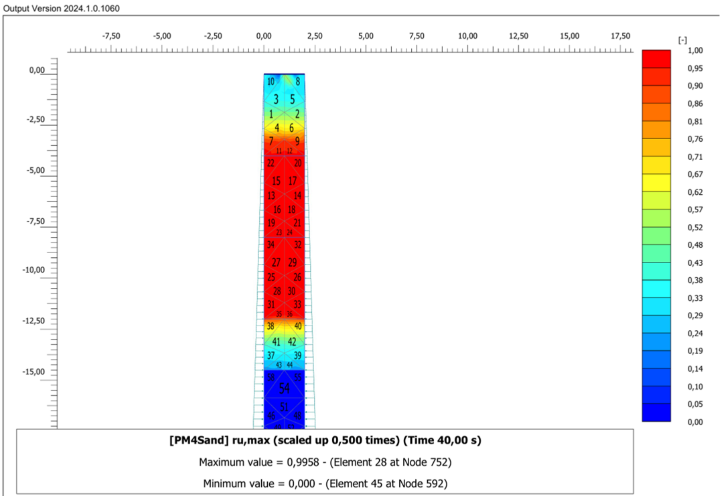

[PM4Sand] ru,max (scaled up 0,500 times) (Time 40,00 s)

Maximum value = 0,9958 - (Element 28 at Node 752)

Minimum value = 0,000 - (Element 45 at Node 592)

Figure 6.6: PLAXIS 2D Maximum EPPR Results - Omaha Wharf No.2

Darendeli shear modulus degradation and damping curves were again utilized, with soil properties listed in Table 6.15.

Table 6.15: DEEPSOIL V7.0 Layer Properties - Ohama Wharf No.2

Depth Range (m)	γ (kN/m^3)	G_0 (kPa)	V_s (m/s)	ϕ (-)	S_u Top (kPa)	S_u Bot (kPa)	K_0 (-)
0 to 12	19	87200	212.19	33	69.76	139.90	0.455
12 to 14.5	21	94000	209.55	34	148.05	166.60	0.441
14.5 to 20	21	111000	227.71	37	190.91	236.50	0.398
20 to 22.5	20	75000	191.80	27	164.87	177.61	0.546
22.5 to 25.5	21	107600	224.20	37	252.62	277.48	0.398
25.5 to 30	21	111000	227.71	37	280.20	317.50	0.398

Using the results from DEEPSOIL, the CDF is employed to predict the EPPR for the first two soil layers down to a depth of 14.5 meters. As illustrated in Figures 6.7a, 6.7b, 6.7c and Figure 6.8 the CDF accurately predicts a maximum EPPR of approximately 1 for the first 12 meters, while for the second layer it predicts it would fully liquefy, whereas in PLAXIS 2D only the first half liquefies as shown in Table 6.16. The 0.9 and 1.0 contour lines correspond to identical values so only one is shown.

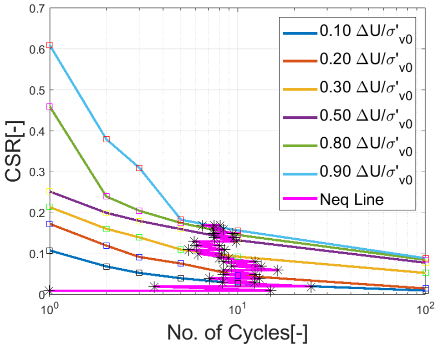

(a) First Half of the First Layer

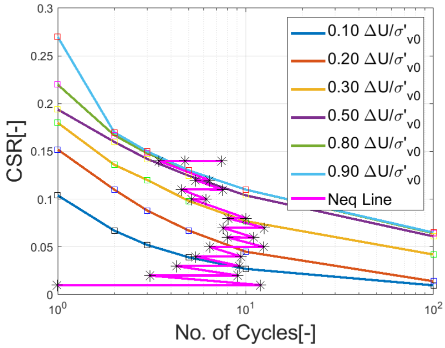

(b) Second Half of the First Layer

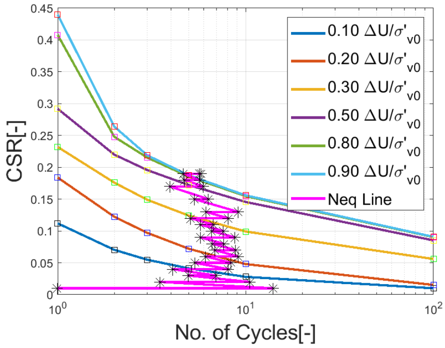

(c) Middle of the Second Layer

Figure 6.7: EPPR Contour Graphs for Different Layers

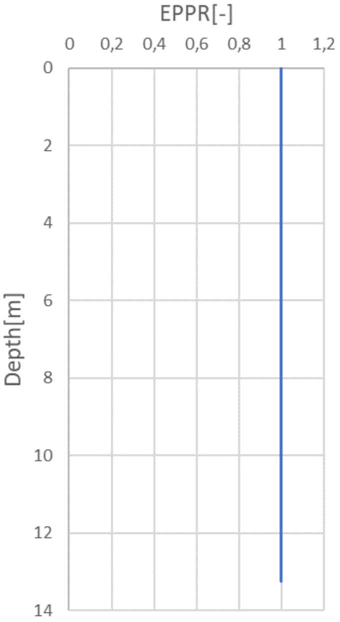

Figure 6.8: Maximum Excess Pore Pressure Ratio by Depth - Omaha Wharf No.2

Table 6.16: Comparison Between RU Max - Omaha Wharf No.2

	Ru_max	Rel. Error
FEM	1	-
Contour Method	1	0%

6.1.3 Summary of Findings - Akita Port

The application of the CDF to the Akita Port case study demonstrates its accuracy in predicting liquefaction potential for both Omaha Wharf No.1 and No.2. The analysis for Omaha Wharf No.1 showed that the CDF predicted no significant liquefaction, which aligns with the observed lack of damage after the 1983 Nihonkai-Chubu Earthquake. However, the framework slightly overestimated the EPPR, reflecting its conservative bias.

For Omaha Wharf No.2, where severe damage occurred due to liquefaction, the CDF successfully predicted the extent and depth of liquefaction, particularly in the loose sand layers, with an EPPR reaching 1.0. As with Wharf No.1, the CDF's predictions were slightly conservative, with marginally higher EPPR values compared to the results from the PLAXIS 2D model for the second layer. Despite this conservatism, the overall pattern of liquefaction severity was accurately captured.

6.2 Ten Noorden von de Waddeneilanden (TNW) Offshore Wind Farm

In this case study, the design of an offshore wind farm in the Netherlands is examined (Source:[33]). The wind farm is primarily founded on dense coarse-grained soils, making it a suitable example to explore how potential soil liquefaction could affect the design of OWTs, particularly regarding PPD. It is important to highlight that this is a theoretical study, as the seismic motions used do not reflect the seismicity of the Netherlands. Instead, seismic loading equivalent to Asia's seismic profile is applied, to understand the effects liquefaction might have under hypothetical earthquake conditions. The findings from this theoretical exercise will offer valuable insights for future offshore wind farm projects, particularly in areas where seismic events may pose a potential risk.

A condensed workflow for all the steps required is illustrated in Figure 6.9.

For the case study, one characteristic location is selected based on available CPT data, indicative soil and spring assumptions, and preliminary structural design. Soil interpretation was conducted using the CPT test results with SGRE's in-house tools.

Lateral spreading, which could be a limiting factor in determining pile diameter, pile wall thickness and the design of other structural elements, is not examined fully in this chapter. Difference in displacements and rotations is shown but a full structural analysis of the pile in regards to potential local buckling is beyond the scope of this thesis.

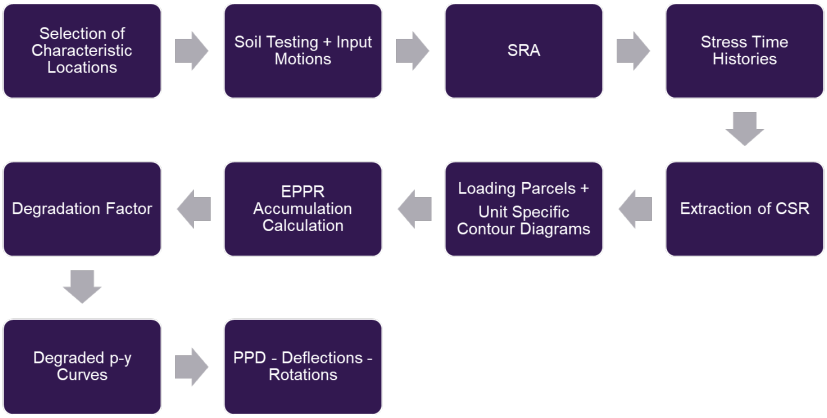

Figure 6.9: Liquefaction Assessment Workflow

6.2.1 TNW Position A

In this section, the location selected for the case study is referred to as Position A. The soil column at this location extends to a depth of 60 meters, consisting of 40 meters of dense sand followed by 20 meters of clay. Figures 6.10a and 6.10b show the Shear Wave Velocity and the Shear Strength after soil interpretation for the soil profile under examination. Derivation and rest soil properties can be found in Appendix A .

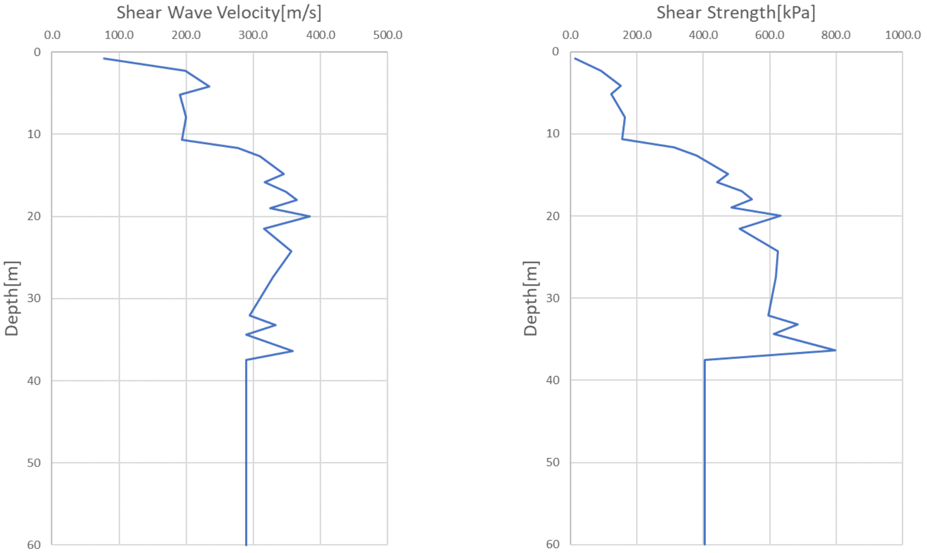

(a) Shear Wave Velocity by Depth - Position A

(b) Soil Shear Strength by Depth - Position A

Figure 6.10: Shear Wave Velocity and Soil Shear Strength at Position A.

The part under examination for EPP accumulation is the first 40 meters. Figure 6.11 indicates the soil stratification of the sandy layers. As no bedrock was detected during the CPT test, it is assumed that the clay layer continues beyond 60 meters. Therefore, in the SRA, bedrock was defined using the shear wave velocity of the clay layer.

For input motion, the two directions of the spectral matched and baseline-corrected Loma Prietta (Woodside station - 1989)(WDS) earthquake are selected as a shallow

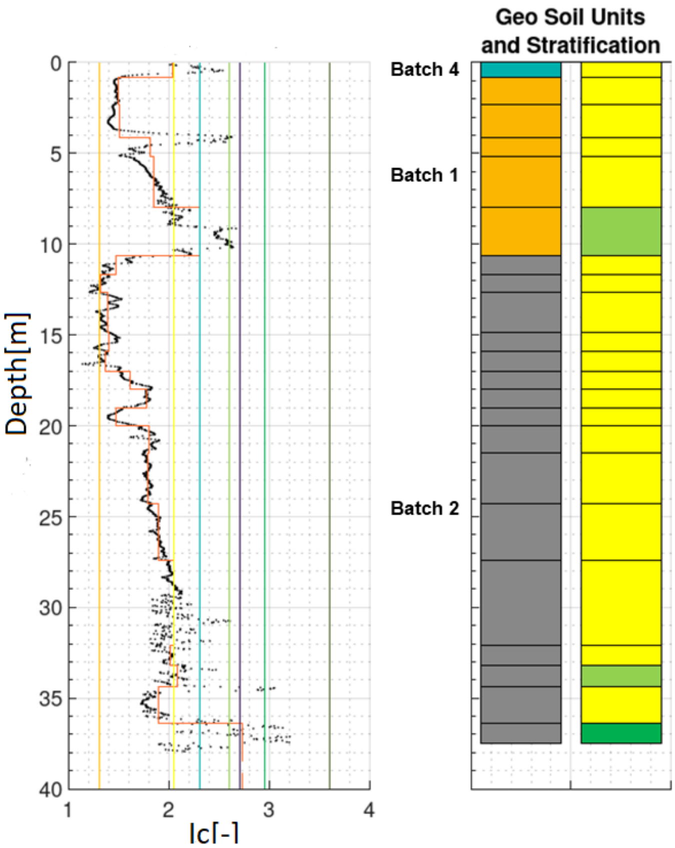

Figure 6.11: Soil Stratification - TNW Position A

crustal earthquake type. A subduction earthquake is also examined using the Michoacan (La Union station - 1985)(UNIO) baseline corrected and spectral matched motion. Their magnitude and ID can be found in Table 4.2. The selected motions and their spectral plots can be found in Appendix B. To be completely accurate, the input motion would have to be matched to a design spectra of the respective V_s. In this case, the motion is matched to $V_s = 315m/s$ while clay layer's V_s is $290m/s$ so it is deemed sufficient and slightly conservative.

Soil data and input motions are then given to DEEPSOIL V7.0 as input. Analysis type settings are consistent with the ones used for validation as exhibited in Table 5.7. Darendeli's Damping and Shear Modulus degradation curves are selected. Damping is set to frequency independent and rest of the time domain solution settings are consistent with Table 5.11.

After completing the SRA under these assumptions, acceleration and stress time histories are extracted. Although accelerations play a crucial role in the structural design of OWTs, they were not considered in this preliminary design phase. Spectral accelerations at the mudline are illustrated in Figure 6.12 , while the CSR time history at the mudline for UNIO000 can be found in Figure 6.13a.

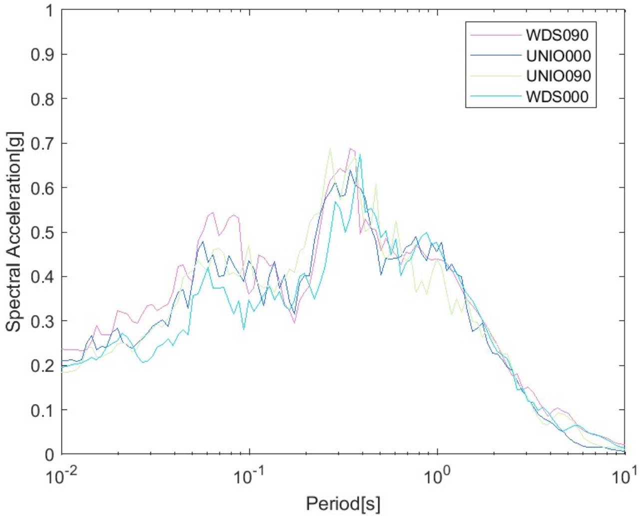

Figure 6.12: Spectral Accelerations - Mudline

Following the extraction of the CSR time history, it is divided into bins using a cycle counting method. RPC, as described in Section 2.5, is employed for this purpose.

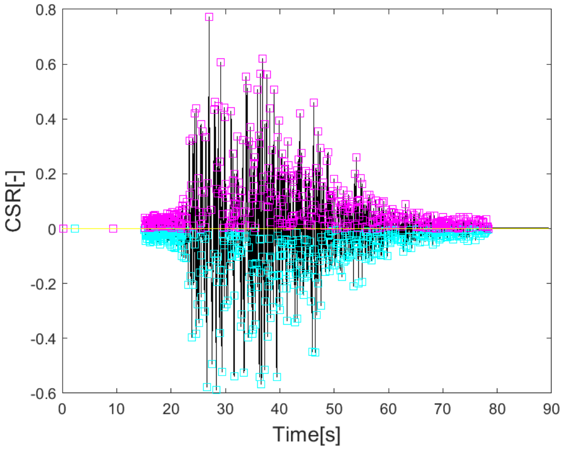

(a) CSR Time History - TNW Position A - Mudline

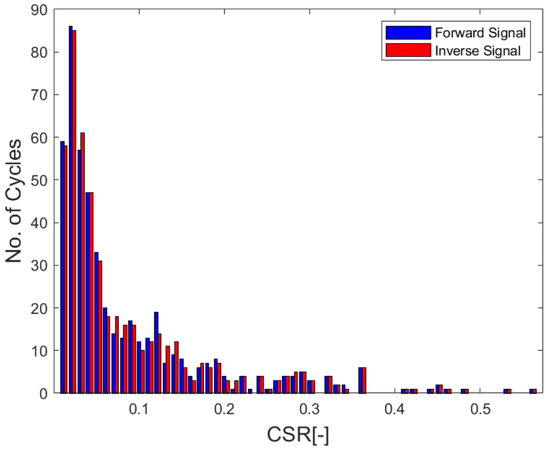

(b) CSR Histogram - TNW Position A - Mudline

Figure 6.13: CSR Time History and CSR Histogram at TNW Position A - Mudline

These bins are then used as loading parcels, which are subsequently utilized to calculate the accumulated EPPR through the application of the CDF as illustrated in Figure 6.14.

It can be observed in Figure 6.15a that the first small layer exhibits EPPRs close to 1. Then there is an intermediate condition with EPPR from 0.4 to 0.7, and for the final sandy layer, the EPPR is less than or equal to 0.1. Full result plate can be found in Appendix C.

To incorporate potential liquefaction into the design of the mono-pile, the degradation factor (De) was used to multiply the ultimate strength of the p-y curves following the formula $De = 1 - 0.9 \times Ru$, as shown in Figure 6.16 and outlined in Section 3.4. The degradation factors per depth can be found in Figure 6.15b.

For the calculation of the PPD, it is assumed that the total load on the MP corresponds to the ultimate limit state (ULS) load. The applied load at the mudline level comprises an 18 MN lateral force and a 1000 MNm moment based on extreme wave and wind conditions.

In this scenario, the static PPD is determined to be 28.3 meters when accounting for maximum displacement of 0.1 times the pile diameter at the top of the MP. When accounting for the liquefaction degradation factor, the penetration depth increases to 30.4 meters. According to the guidelines provided by DNV [17] and API [1], soil parameter degradation due to cyclic loading, which occurs throughout the lifecycle of an OWT, must be considered. Following these guidelines, and excluding the effects of liquefaction, the PPD is calculated to be 33 meters.

The impact on rotations and deflections is illustrated in Figures 6.20a and 6.20b.

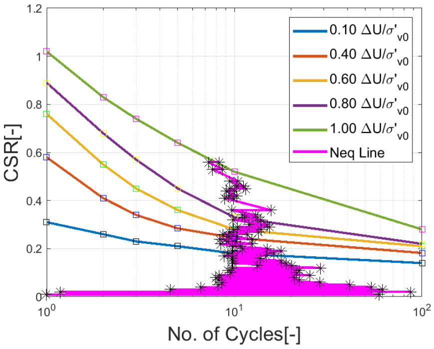

(a) Contour Graph for Batch 4

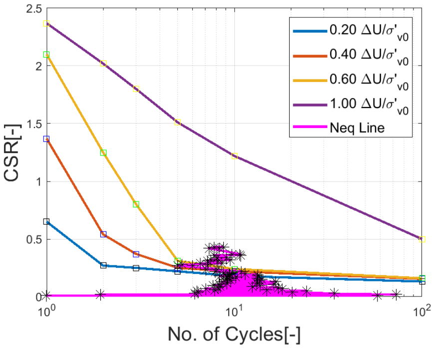

(b) Contour Graph for Batch 1

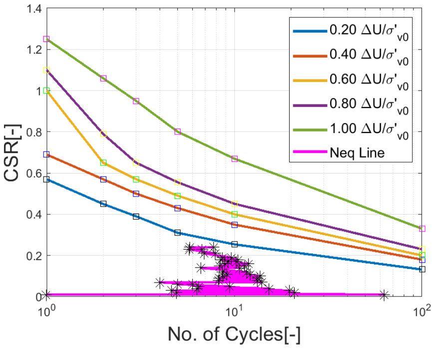

(c) Contour Graph for Batch 2

Figure 6.14: Contour Graphs for Different Sand Batches at TNW Position A

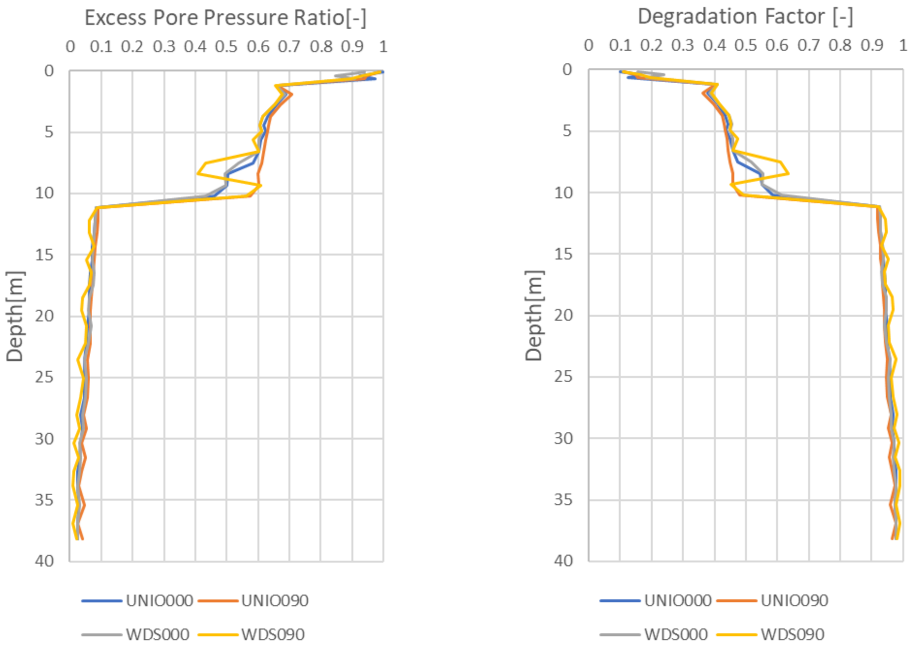

(a) Excess Pore Pressure Ratio - TNW Position A

(b) Degradation Factor by Depth - TNW Position A

Figure 6.15: Excess Pore Pressure Ratio and Degradation Factor by Depth at Position A

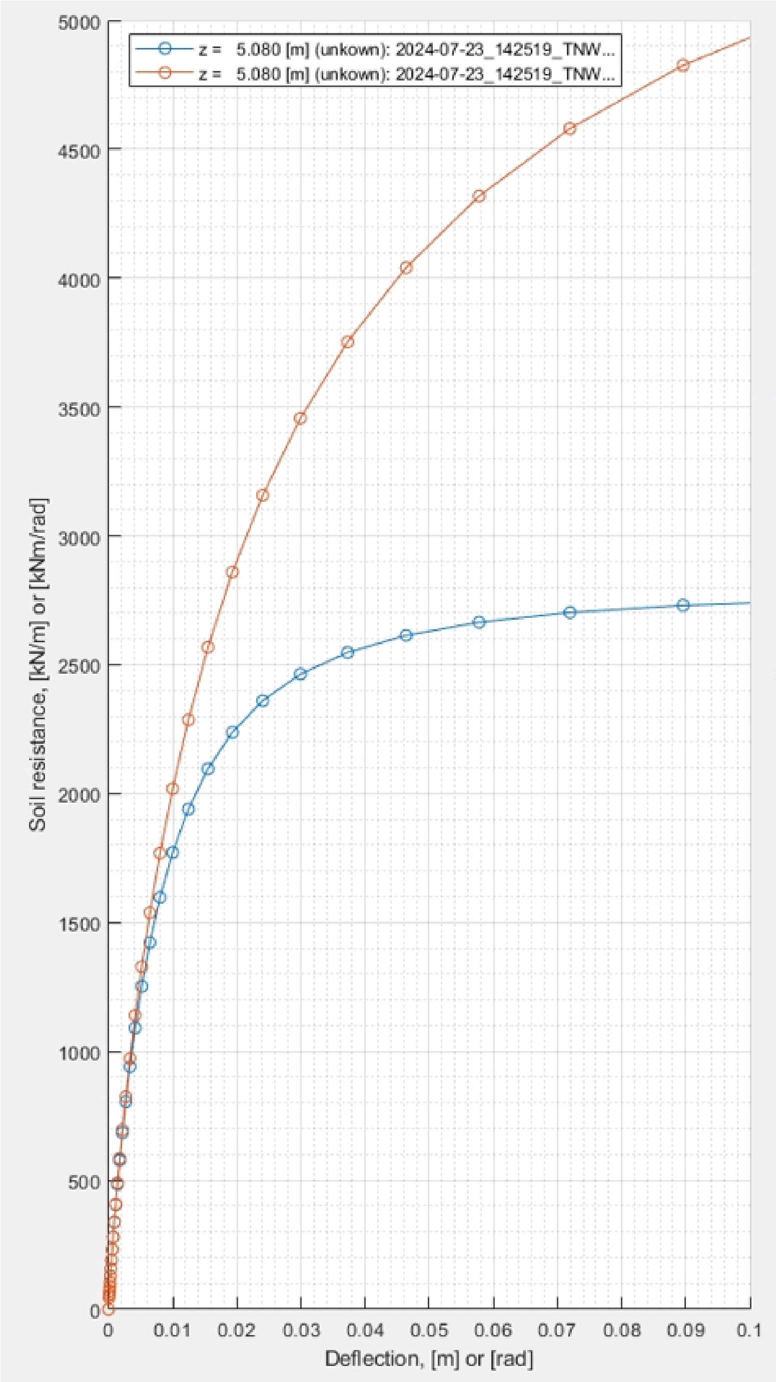

Figure 6.16: Original and Degraded p-y Curve - Depth of 5.080 m

6.2.2 TNW Position A Modified

This section investigates the effects of altering the second soil layer properties at Position A by modifying its contour diagram to represent a soil with lower cyclic resistance. The objective is to evaluate how these changes influence the liquefaction potential and EPPR in the sandy layers and as a consequence, the pile design. The updated soil stratification is shown in Figure 6.17.

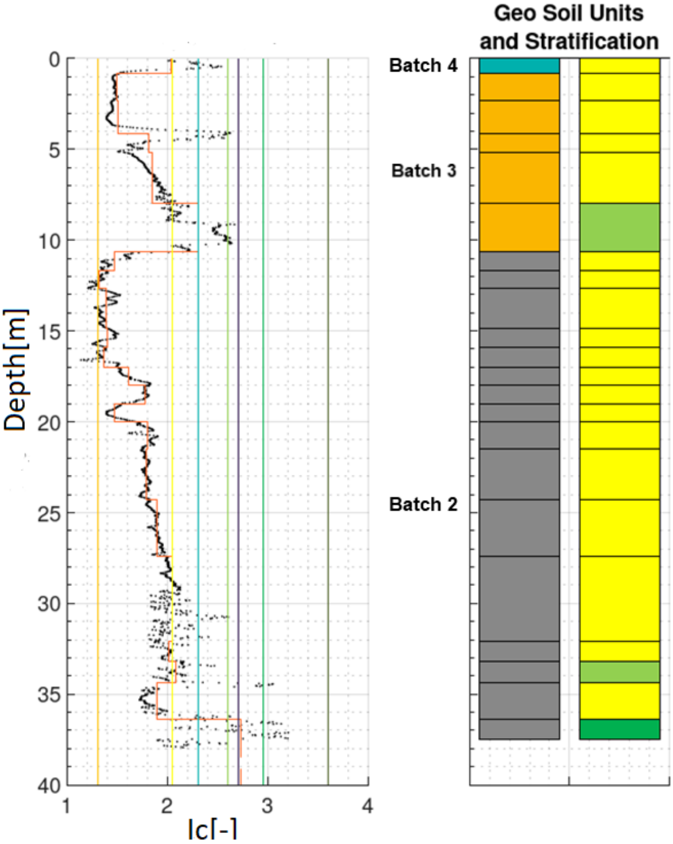

Figure 6.17: Soil Stratification - TNW Position A Modified

Soil properties are not changed for the SRA. If the updated soil properties are taken into account, the results would be even more conservative, as soils with low CRRs usually exhibit higher CSRs due to low shear wave velocity and shear strength.

As expected, the now weaker second layer exhibits higher EPPRs than before since it is now fully liquefied, as shown in Figure 6.18 and 6.19a. Consequently, the degradation factor is lower for the same layer, as indicated in Figure 6.19b. Full result plate can be found in Appendix C.

Similarly, the PPD is determined using SGRE's in-house tools. For the static case, the depth remains 28.3 meters, given unchanged soil properties except the EPPR contour diagram. When considering soil degradation due to liquefaction, the total penetration depth increases to 31.1 meters. According to DNV [17] and API [1] guidelines for cyclic degradation of soil properties, the total penetration depth is again 33 meters as soil properties are not altered. Considering both liquefaction effects and cyclic degradation of the soil properties, the PPD increases to 35.2 meters. The results for all scenarios are summarized in Table 6.17. This PPD is highly conservative, as it assumes the occurrence of a very strong earthquake precisely at the end of the OWT's lifecycle. Therefore, the final determination should involve a probabilistic combination that reflects the design life and the return periods of the examined events, possibly using a percentage of total soil degradation rather than the full factor.

Table 6.17: Pile Penetration Depths under Various Conditions

	Pile Penetration Depth [m]
Static	28.3
Cyclic Degradation	33.0
Liquefaction	30.4
Modified Liquefaction	31.3
Modified Liquefaction + Cyclic Degradation	35.2

Deflections and rotations can be found in Figures 6.20a and 6.20b.

It can be observed that the cases that take into account liquefaction lead to larger deflections and rotations which correspond to higher moments and shear forces.

These results showcase that potential liquefaction will lead to probable reconsideration of the thickness of the MP foundation as well as larger PPDs when designing for the earthquake event to happen near the end of the OWTs life cycle.

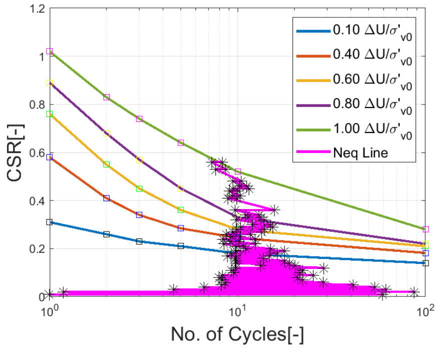

(a) Contour Graph for Batch 4

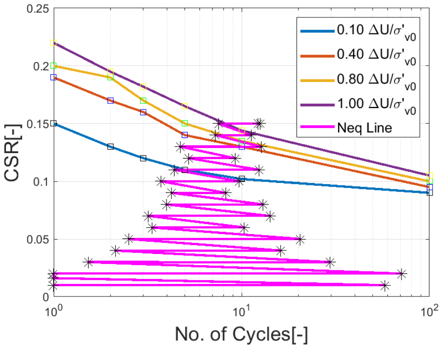

(b) Contour Graph for Batch 3

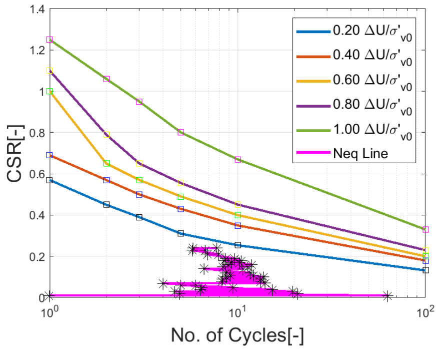

(c) Contour Graph for Batch 2

Figure 6.18: Contour Graphs for Different Sand Batches at TNW Position A (Modified)

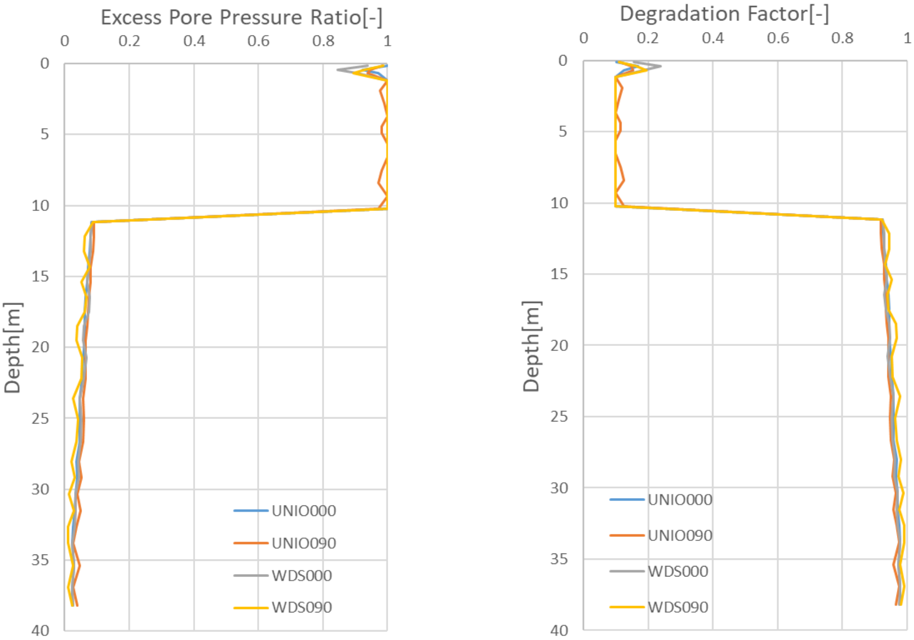

(a) Excess Pore Pressure Ratio - TNW Position A Modified

(b) Degradation Factor by Depth - TNW Position A Modified

Figure 6.19: Excess Pore Pressure Ratio and Degradation Factor by Depth at Position A Modified

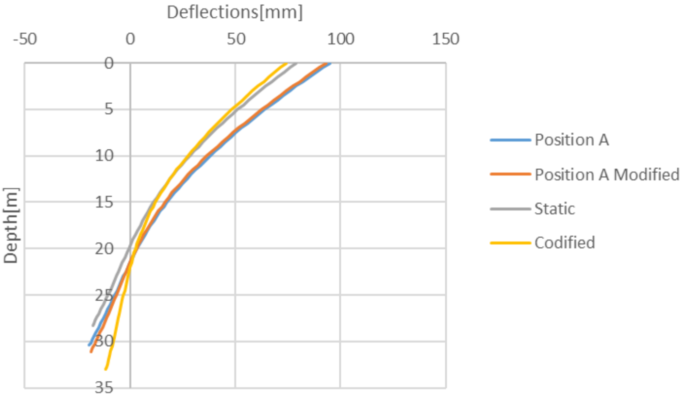

(a) Deflections for TNW Position A, All Cases

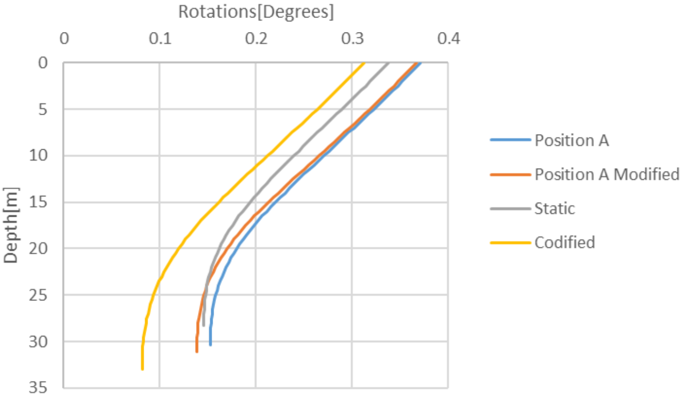

(b) Rotations for TNW Position A, All Cases

Figure 6.20: Deflections and Rotations for TNW Position A, All Cases

6.2.3 Summary of Findings - TNW Offshore Wind Farm

The liquefaction analysis for TNW Position A and its modified counterpart demonstrates the significant influence of soil's cyclic resistance on the design of OWTs foundations under seismic loading. In the original analysis for Position A, the dense sand layers exhibited moderate EPPRs, with only small sections of the soil column showing signs of potential liquefaction. The corresponding PPD was calculated to be 28.3 meters under static conditions, increasing to 30.4 meters when accounting for liquefaction effects. Both rotations and deflections were observed to increase as a result of the liquefaction, leading to higher moments and shear forces acting on the MP foundation.

In the modified case, where the cyclic resistance of the second sand layer was reduced, the liquefaction potential increased significantly, with the second layer reaching full liquefaction. This led to a lower degradation factor and a further increase in PPD to 31.3m when considering only liquefaction and to 35.2 meters when both liquefaction and cyclic degradation are considered. As in the original case, liquefaction caused increases in rotations and deflections, which again resulted in higher moments and shear forces acting on the MP.

Chapter 7

Conclusions, Recommendations and Guidelines

This chapter presents the key conclusions drawn from the research and analysis conducted throughout this thesis. The primary objective of this study was to assess the effectiveness of the CDF in predicting liquefaction potential and EPPRs in coarse-grained soils under seismic loading. Through the application of the CDF to both theoretical and real-world case studies, and its comparison with widely used liquefaction assessment methods, several important insights have emerged.

In addition to summarizing the performance of the CDF, this chapter outlines recommendations for future research areas, particularly those that could further refine the framework and improve its applicability in engineering practice. Finally, guidelines for the practical implementation of the CDF in engineering design are provided, emphasizing key considerations for its use in seismic-prone regions and the potential advantages it offers over traditional methods.

7.1 Conclusions

The objective of this thesis was to evaluate the accuracy and reliability of the CDF in predicting EPPRs and liquefaction potential in coarse-grained soils under seismic loading.

Regarding the accuracy of the method, both the validation and the Omaha Wharf case study indicate that the method is conservatively accurate. It reliably predicts the onset of liquefaction and low EPPRs, while for intermediate conditions (EPPR between 0.3 and 0.5), it provides valuable but slightly conservative information (Error of around 20%).

When compared to the widely used methods by Boulanger and Idriss (2014)[8] and Youd et al. (2001)[40], the CDF offers specific information in terms of EPPR, CSR, and equivalent cycles instead of solely a SF. However, the CDF relies on conducting detailed SRA and laboratory tests to create the contour plots. SRA demands significant expertise in ground motions, soil mechanics, soil dynamics, and numerical modeling, thus requiring more extensive knowledge than the methods currently used in engineering practice, such as Boulanger and Idriss (2014) and Youd et al. (2001), which primarily involve applying empirical formulas derived from CPT or SPT data.

Deriving the contour graphs and obtaining accurate soil data for the SRA also necessitates expensive laboratory equipment, if the data is not available publicly like in the case of TNW, and specialists to ensure proper test conduction. The contour plot, in particular, plays a crucial role, as demonstrated by the sensitivity test, in accurately assessing the EPP accumulation.

Lastly, based on the offshore wind farm preliminary design study, it is evident that considering liquefaction effects in MP foundation design can significantly alter PPD and potentially the structural design, especially when considering that cyclic degradation of the soil properties might occur before the earthquake event.

Overall, it is concluded that the CDF is a valuable tool for engineering practice when used appropriately. For complex structures like OWTs, it aids in optimizing the design, which justifies the resources used.

7.2 Recommendations

The research presented in this thesis highlights several areas that warrant further investigation to improve the CDF and its practical application in engineering projects. The following recommendations are proposed:

Every constitutive model has inherent limitations, and validating the method through laboratory experiments would provide crucial insights. This validation process can help determine whether the errors observed under intermediate conditions are due to the FEM model or the method itself. Since PM4Sand is specifically designed to accurately capture the onset of liquefaction, it's important to exclude potential shortcomings related to the constitutive model. To achieve this, one could conduct a shaking test on a sand column, recording the excess pore pressure, and then compare these results with those obtained from applying the CDF to the same soil column. This approach would clarify whether the discrepancies arise from the model or the method.

It would be valuable to further explore the differences between the CDF and the simplified method. In the Omaha Wharf 1 case study, the sand layers were calibrated based on the method from Boulanger and Idriss (2014) [8], aligning the FEM results with the simplified results, as both were calibrated to the same CRR. However, calibrating the model based on laboratory tests could yield different CRRs, which may not fully align with the simplified method. This underscores the importance of understanding the variations that may arise when comparing the results of the SF-based methods and the CDF.

Furthermore, potential methods for investigating the dissipation of excess pore pressure should be explored. In a soil column, the first few layers will drain water upwards, resulting in a decrease in the EPPR. Additionally, drainage occurring between two sand layers during excitation could also influence the final EPPRs. To implement this, a modification could be done in the CDF where based on the distance from the adjacent layers and the permeability coefficient k The model would then adjust the pore pressure accordingly, either decreasing or increasing it based on the specific drainage conditions.

Lastly, the degradation factor (De) should be further investigated. Denser sands tend to dilate and increase their shear strength after liquefaction. Adopting a single degradation factor to model the soil structure interaction, is not the most efficient way to address it. Investigating a degradation factor that depends on the current strain and the initial relative density of the material or a different formulation of the p-y curves would perhaps be more accurate and efficient.

By addressing these areas of research, the CDF could become a more versatile and reliable tool, further enhancing its role in seismic liquefaction assessment for OWTs and other critical infrastructure.

7.3 Guidelines

For engineers looking to implement the CDF in seismic liquefaction assessment, the following guidelines are proposed to ensure accurate and effective application.

Before employing the CDF, it is advisable to first apply SF-based methods. If the soil is found to be not prone to liquefaction, the use of the CDF may be unnecessary, thereby conserving time and resources. However, if the soil is susceptible to liquefaction or the soil column extends beyond depths greater than 25 meters, utilizing the

CDF becomes more relevant. Additionally, if an optical examination of the contour graphs reveals low CRR in some of the coarse-grained layers, it is a strong indication that the CDF should be applied.

When using the CDF, it is crucial to examine the generated contour plots from laboratory tests. With experience, it is possible to identify materials that are likely to develop high EPPRs through visual inspection of these graphs.

In the final design of a MP foundation, the impact of loading conditions, along with the combined effects of cyclic and seismic degradation due to liquefaction, is critical in determining the final PPD and potentially influencing the structural design of the MP. It is essential to carefully consider the design life and the return period of the relevant events to develop an appropriate probabilistic event model. Combining two extreme events without consideration of their combined probability can lead to overly conservative and economically unfeasible designs. A more balanced approach begins with assessing the cyclic degradation of soil properties through laboratory tests. By fitting a distribution to the degradation data and selecting a percentile that aligns with the design life, the cyclic degradation can be more accurately modeled over time. Next, a Poisson distribution can be applied to estimate the probability of a severe seismic event occurring near the design location at a given year. Finally, an economic analysis should be conducted to determine the optimal time frame for considering the combined effects of seismic and cyclic degradation. This approach helps to avoid over designing the MP foundations, leading to more efficient and cost-effective solutions.

By following these guidelines, engineers can ensure that the CDF is applied correctly and effectively, leading to more accurate liquefaction assessments and more effective designs for seismic-prone regions.

Appendix A

Soil Properties TNW Position A

Table A.1: General Layer Properties

Layer	Depth Range [m]	γ [kN/m^3]	γ' [kN/m^3]	K_0 [-]	ν [-]
1	0 to 0.82	14.87	4.87	0.47	0.49
2	0.82 to 2.3	19.62	9.62	0.33	0.49
3	2.3 to 4.16	20.29	10.29	0.34	0.49
4	4.16 to 5.16	18.99	8.99	0.41	0.49
5	5.16 to 7.98	19.12	9.12	0.42	0.49
6	7.98 to 10.66	18.91	8.91	0.55	0.49
7	10.66 to 11.66	20.73	10.73	0.35	0.49
8	11.66 to 12.66	21.29	11.29	0.32	0.49
9	12.66 to 14.88	21.87	11.87	0.32	0.49
10	14.88 to 15.88	21.33	11.33	0.34	0.49
11	15.88 to 17	21.83	11.83	0.32	0.49
12	17 to 18	22.08	12.08	0.34	0.49
13	18 to 19	21.43	11.43	0.37	0.49
14	19 to 20	22.30	12.30	0.32	0.49
15	20 to 21.5	21.16	11.16	0.38	0.49
16	21.5 to 24.28	21.79	11.79	0.36	0.49
17	24.28 to 27.44	21.21	11.21	0.38	0.49
18	27.44 to 32.1	20.28	10.28	0.43	0.49
19	32.1 to 33.2	21.01	11.01	0.41	0.49
20	33.2 to 34.36	19.94	9.94	0.43	0.49
21	34.36 to 36.36	21.41	11.41	0.38	0.49
22	36.36 to 37.48	19.71	9.71	1.00	0.49
23	37.48 to 60	19.71	9.71	1.00	0.49

Table A.2: Strength Properties

Layer	ϕ' [deg]	$\sigma'_{\text{v,top}}$ [kN/m^2]	$\sigma'_{\text{v,bot}}$ [kN/m^2]	Cvs_{top} [kN/m^2]	Cvs_{bot} [kN/m^2]	S_u Top [kN/m^2]	S_u Bot [kN/m^2]
1	32	0.0	4.0	10.0	10.0	10.0	12.5
2	42	4.0	33.0	62.0	62.0	65.6	91.7
3	41.5	33.0	70.8	89.5	89.5	118.7	152.1
4	36.5	70.8	89.8	54.9	54.9	107.3	121.4
5	35.5	89.8	143.7	61.2	61.2	125.2	163.7
6	27	143.7	194.4	56.5	56.5	129.7	155.5
7	40.5	194.4	215.1	127.1	127.1	293.1	310.8
8	42.5	215.1	236.4	163.2	163.2	360.3	379.8
9	43	236.4	284.9	208.8	208.8	429.2	474.5
10	41.5	284.9	306.3	171.1	171.1	423.2	442.0
11	42.5	306.3	330.7	211.9	211.9	492.5	514.9
12	41.5	330.7	352.8	234.7	234.7	527.2	546.8
13	39	352.8	374.2	181.3	181.3	467.0	484.3
14	43	374.2	396.5	263.7	263.7	612.7	633.5
15	38.5	396.5	428.3	169.5	169.5	484.9	510.2
16	39.5	428.3	488.8	221.3	221.3	574.3	624.3
17	38	488.8	555.9	184.4	184.4	566.3	618.7
18	35	555.9	650.4	140.5	140.5	529.7	595.9
19	36.5	650.4	673.5	186.8	186.8	668.0	685.1
20	34.5	673.5	696.6	133.4	133.4	596.3	612.2
21	38	696.6	739.4	220.5	220.5	764.8	798.2
22	–	739.4	761.5	–	–	404	404
23	–	761.5	1205.4	–	–	404	404

Table A.3: Stiffness Properties

Layer	G_0 Top [MN/m^2]	G_0 Bot [MN/m^2]	V_s Top [m/s^2]	V_s Bot [m/s^2]	OCR [-]	Plasticity Index [%]
1	9	9	77.1	77.1	1	0
2	79	79	198.7	198.7	1	0
3	114	114	234.8	234.8	1	0
4	70	70	190.2	190.2	1	0
5	78	78	200.0	200.0	1	0
6	72	72	193.3	193.3	1	0
7	162	162	276.9	276.9	1	0
8	208	208	309.6	309.6	1	0
9	266	266	345.4	345.4	1	0
10	218	218	316.6	316.6	1	0
11	270	270	348.3	348.3	1	0
12	299	299	364.5	364.5	1	0
13	231	231	325.2	325.2	1	0
14	336	336	384.5	384.5	1	0
15	216	216	316.4	316.4	1	0
16	282	282	356.3	356.3	1	0
17	235	235	329.7	329.7	1	0
18	179	179	294.3	294.3	1	0
19	238	238	333.4	333.4	1	0
20	170	170	289.2	289.2	1	0
21	281	281	358.8	358.8	1	0
22	168	168	289.2	289.2	2.3	12
23	168	168	289.2	289.2	2.3	12

Appendix B

Earthquakes

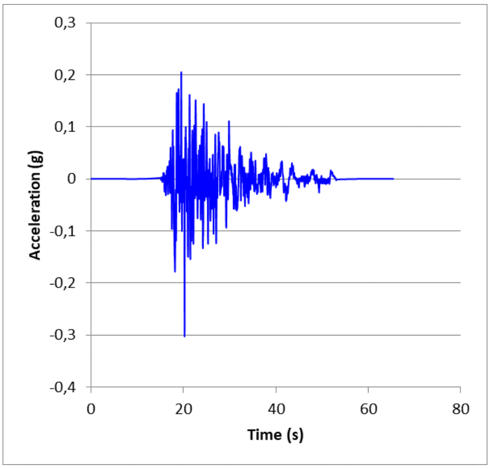

Figure B.1: Acceleration - Spectral Matched and Baseline Corrected WDS090

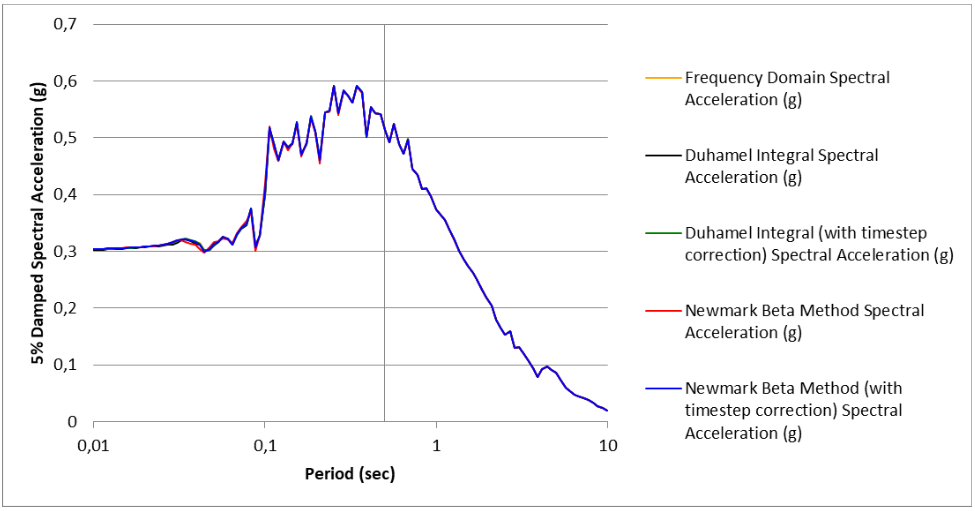

Figure B.2: 5% Damped Spectral Acceleration - Spectral Matched and Baseline Corrected WDS090

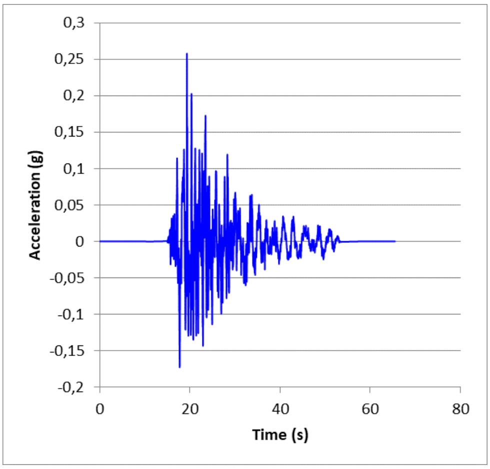

Figure B.3: Acceleration - Spectral Matched and Baseline Corrected WDS000

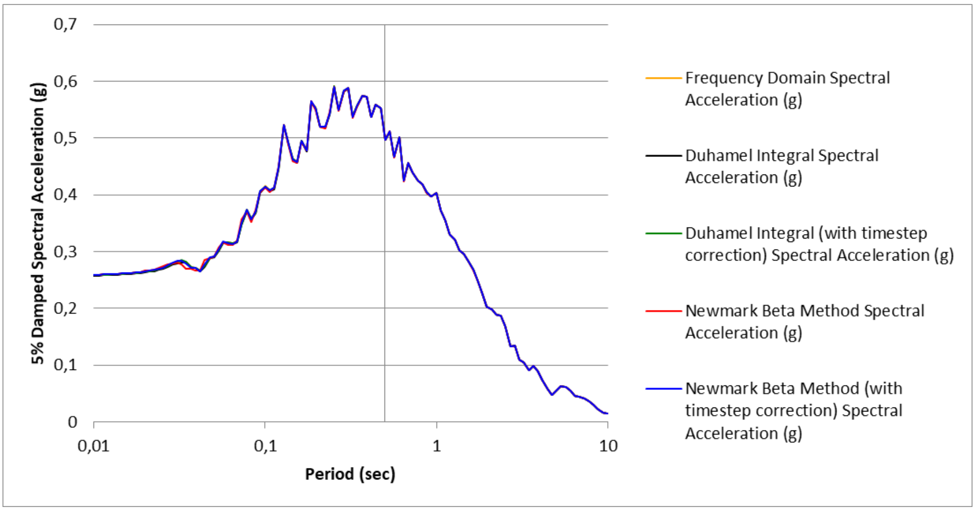

Figure B.4: 5% Damped Spectral Acceleration - Spectral Matched and Baseline Corrected WDS000

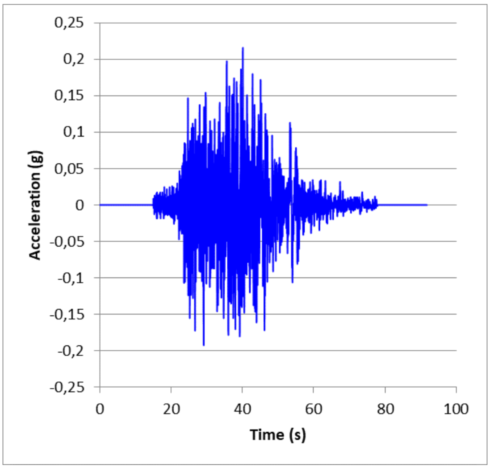

Figure B.5: Acceleration - Spectral Matched and Baseline Corrected UNIO090

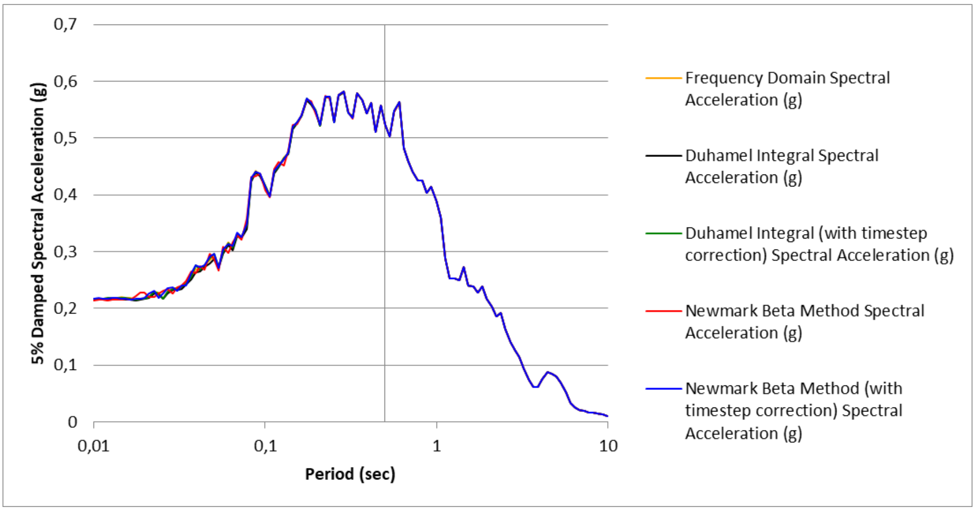

Figure B.6: 5% Damped Spectral Acceleration - Spectral Matched and Baseline Corrected UNIO090

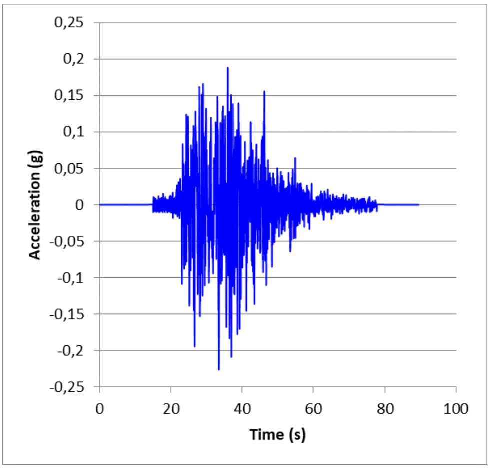

Figure B.7: Acceleration - Spectral Matched and Baseline Corrected UNIO000

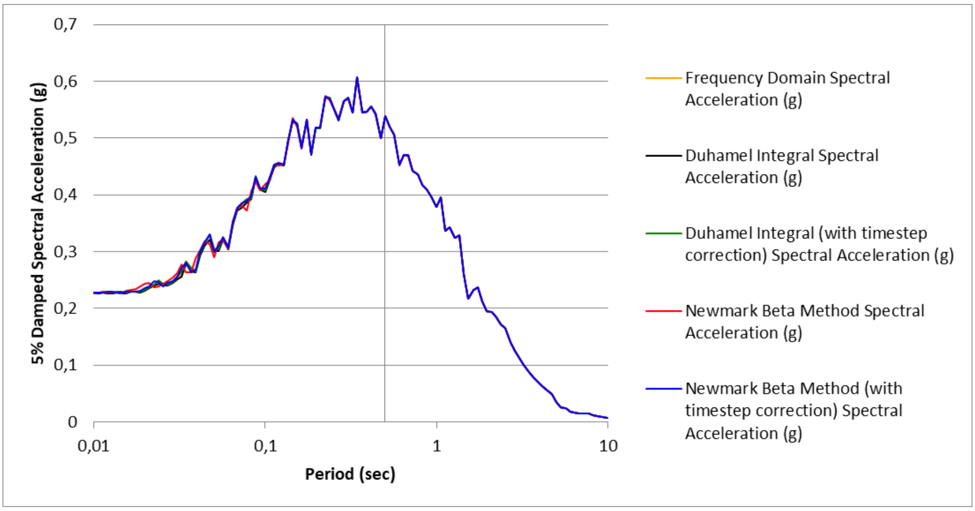

Figure B.8: 5% Damped Spectral Acceleration - Spectral Matched and Baseline Corrected UNIO000

Appendix C

TNW - CDF Result Plates

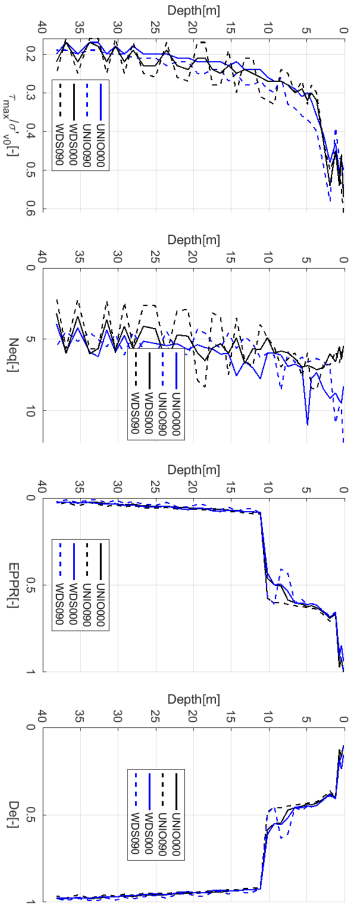

Figure C.1: Plate with τ_{max}/σ'_{v0}, N_{eq}, $EPPR$, and Degradation Factor D_e - TNW Position A

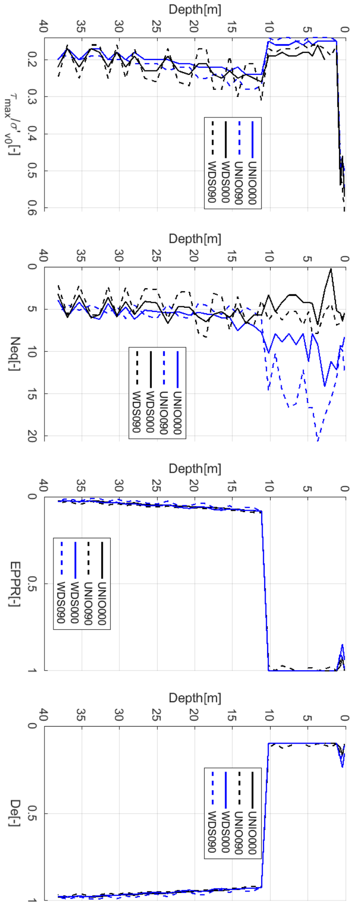

Figure C.2: Plate with τ_{max}/σ'_{v0}, N_{eq}, $EPPR$, and Degradation Factor D_e - TNW Position A Modified

Bibliography

[1] American Petroleum Institute. *API RP 2A-WSD: Recommended Practice for Planning, Designing and Constructing Fixed Offshore Platforms – Working Stress Design*. API Publishing Services, March 2000.

[2] K.H. Andersen. Cyclic Soil Parameters for Offshore Foundation Design: The 3rd McClelland Lecture. In *Proceedings of the 3rd International Symposium on Frontiers in Offshore Geotechnics (ISFOG)*, 2015.

[3] Laing Barden. The Winkler Model and Its Application to Soil. *The Structural Engineer*, 41, 1963.

[4] K. Been and M. G. Jefferies. A State Parameter for Sands. *Geotechnique*, 35(2):99–112, 1985.

[5] R. W. Boulanger. A Sand Plasticity Model for Earthquake Engineering Applications. Technical Report UCD/CGM-10/01, University of California, Davis, California, 2010.

[6] R. W. Boulanger and K. Ziotopoulou. PM4Sand (version 3): A Sand Plasticity Model for Earthquake Engineering Applications. Technical Report UCD/CGM-15/01, University of California, Davis, California, 2015.

[7] R. W. Boulanger and K. Ziotopoulou. PM4Sand (version 3.1): A Sand Plasticity Model for Earthquake Engineering Applications. Technical Report UCD/CGM-17/01, University of California, Davis, California, 2017.

[8] Ross W. Boulanger and I. M. Idriss. CPT And SPT Based Liquefaction Triggering Procedures. Technical Report UCD/CGM-14/01, Center for Geotechnical Modeling, Department of Civil and Environmental Engineering, University of California, Davis, California, April 2014.

[9] Ross W. Boulanger, Bruce L. Kutter, Scott J. Brandenberg, Priyanshu Singh, and Dongdong Chang. Pile Foundations in Liquefied and Laterally Spreading Ground During Earthquakes: Centrifuge Experiments & Analyses. Technical Report UCD/CGM-03/01, Center for Geotechnical Modeling, Department of Civil & Environmental Engineering, University of California, Davis, California, 2003.

[10] Dinu Bratosin and Tudor Sireteanu. Hysteretic Damping Modeling by Nonlinear Kelvin-Voigt Model. *Proceedings of the Romanian Academy, Series A*, 3:1–6, January 2002.

[11] R. Brinkgreve, E. Engin, and H. Engin. Validation of Empirical Formulas to Derive Model Parameters for Sands. Technical report, TU Delft, PLAXIS, 2010.

[12] Confidential. Confidential. Internal document, 2019. Confidential Project Report, SGRE.

[13] Y. F. Dafalias and M. T. Manzari. A Simple Constitutive Model for Sand under Monotonic and Cyclic Loading. *International Journal for Numerical and Analytical Methods in Geomechanics*, 28(9):1047–1064, 2004.

[14] Mehmet Baris Darendeli. *Development of a New Family of Normalized Modulus Reduction and Material Damping Curves*. Doctoral dissertation, The University of Texas at Austin, 2001.

[15] M. De Groot, M. Bolton, P. Foray, P. Meijers, A. Palmer, R. Sandven, A. Sawicki, and T. Teh. Physics of Liquefaction Phenomena around Marine Structures. *Journal of Waterway, Port, Coastal, and Ocean Engineering*, 2006.

[16] David A Dillard, Bikramjit Mukherjee, Preetika Karnal, Romesh C Batra, and Joelle Frechette. A Review of Winkler's Foundation and Its Profound Influence on Adhesion and Soft Matter Applications. *Soft Matter*, 14:3669–3683, 2018.

[17] DNV GL. *DNVGL-RP-C212: Offshore Soil Mechanics and Geotechnical Engineering*. Det Norske Veritas Germanischer Lloyd, 2019-09 - amended 2021-09 edition, September 2019. Available at: `https://www.document-center.com/standards/show/DNVGL-RP-C212`.

[18] Ricardo Dobry, Victor Taboada, and Lianyang Liu. Centrifuge Modeling of Liquefaction Effects During Earthquakes. In K. Ishihara, editor, *Proc. 1st Intl. Conf. On Earthquake Geotechnical Engineering*, volume 3, pages 1291–1324, Tokyo, Japan, 1995.

[19] J. M. Duncan and C. Y. Chang. Nonlinear Analysis of Stress and Strain in Soils. *Journal of the Soil Mechanics and Foundations Division, ASCE*, 96(5):1629–1653, 1970.

[20] European Committee for Standardization (CEN). *Eurocode 8: Design of Structures for Earthquake Resistance—Part 1: General Rules, Seismic Actions and Rules for Buildings*. EN 1998-1. European Committee for Standardization (CEN), Brussels, Belgium, 2004.

[21] L. Zampich G. Vilhar, R.B.J. Brinkgreve. *PM4Sand Model Manual 2018*. Plaxis bv, Delft, Netherlands, 2018. Available from www.plaxis.nl.

[22] David R. Groholski, Youssef M. A. Hashash, Michael I. Musgrove, Jonathan A. Harmon, Caleb A. Phillips, and Daniel Park. DEEPSOIL 6.1, User Manual: A Computer Program for One-Dimensional Ground Response Analysis. Technical report, University of Illinois at Urbana-Champaign, Champaign, IL, 2016. Available from http://deepsoil.cee.illinois.edu.

[23] Daniel Guerreiro and Stavroula Kontoe. Comparative study of stiffness reduction and damping curves for dynamic analysis of soils. In *7th International Conference on Computational Methods in Structural Dynamics and Earthquake Engineering (COMPDYN)*. ECCOMAS, 2019.

[24] J. Harmon. *Non-Linear Site Amplification Functions for Central and Eastern North America*. University of Illinois at Urbana-Champaign, Urbana, Illinois, 2017.

[25] Y.M.A. Hashash, M.I. Musgrove, J.A. Harmon, O. Ilhan, G. Xing, O. Numanoglu, D.R. Groholski, C.A. Phillips, and D. Park. *DEEPSOIL 7.0 User Manual*. Board of Trustees of University of Illinois at Urbana-Champaign, Urbana, IL, 2020.

[26] W. D. Iwan. On a Class of Models for the Yielding Behavior of Continuous and Composite Systems. *Journal of Applied Mechanics*, 34(3):612–617, 1967.

[27] Japanese Road Association. Design Specifications for Highway Bridges - Part V Seismic Design. Technical report, Japanese Road Association (JRA), March 2002.

[28] S. L. Kramer. *Geotechnical Earthquake Engineering*. Prentice Hall, 1996.

[29] D. Lombardi and S. Bhattacharya. Evaluation of Seismic Performance of Pile-Supported Models in Liquefiable Soils. *Earthquake Engineering & Structural Dynamics*, 45(7):1019–1038, 2016.

[30] Gheorghe Marmureanu, C. O. Cioflan, Alexandru Marmureanu, and Elena Manea. Bridging the Gap Between Nonlinear Seismology as Reality and Earthquake Engineering. In *Bridging the Gap Between Nonlinear Seismology as Reality and Earthquake Engineering*. Springer International Publishing, 2015.

[31] PLAXIS bv, Delft, Netherlands. *Material Models Manual*, 2017. Version 2017.

[32] P. K. Robertson and C. E. Wride. Evaluating Cyclic Liquefaction Potential Using the Cone Penetration Test. *Canadian Geotechnical Journal*, 35:442–459, 1998.

[33] RVO. General Information TNW. `https://offshorewind.rvo.nl/page/view/796048cf-12cb-4e90-8124-ae4eb73c1c49/general-information-tnw`. Accessed: August 18, 2024.

[34] A. N. Schofield and C. P. Wroth. *Critical State Soil Mechanics*. McGraw-Hill, 1968.

[35] SeismoSoft. SeismoMatch. `https://www.seismosoft.com/seismomatch/`, 2024. Version 3.0.

[36] Anastasios Stamou. Internship Report. *Siemens Gamesa Renewable Energy*, 2023.

[37] P.V. Toloza. Liquefaction Modelling Using the PM4Sand Constitutive Model in PLAXIS 2D. Master of science thesis, Delft University of Technology, Delft, The Netherlands, 2018.

[38] G. Vilhar, A. Laera, F. Foria, A. Gupta, and R. B. J. Brinkgreve. Implementation, Validation, and Application of PM4Sand Model in PLAXIS. In *Geotechnical Special Publication*, volume GSP 292, pages 200–211, 2018.

[39] Emil Winkler. *Die Lehre von der Elastizität und Festigkeit*. H. Dominicus, Prague, 1867.

[40] T.L. Youd and et al. Proceedings of the NCEER Workshop. In *Proceedings of the NCEER Workshop*, Buffalo, NY, 2001. National Center for Earthquake Engineering Research.

TU Delft
Delft
University of
Technology

SIEMENS Gamesa
RENEWABLE ENERGY